Università degli Studi di Napoli
"Federico II"

Scuola Politecnica e delle Scienze di Base
Area Didattica di Scienze Matematiche,
Fisiche e Naturali

corso di laurea magistrale in

FISICA

Curriculum: Sperimentale Applicativo
Fisica Subnucleare e Astroparticellare

Measurement of low p_T D^+ meson production cross section at CDF II

Relatori:
Prof. Fabio Ambrosino
Prof. Stefano Zucchelli
Dott. Manuel Mussini

Candidato:
Luigi Marchese
Matr. N94000097

Anno Accademico 2012 - 2013

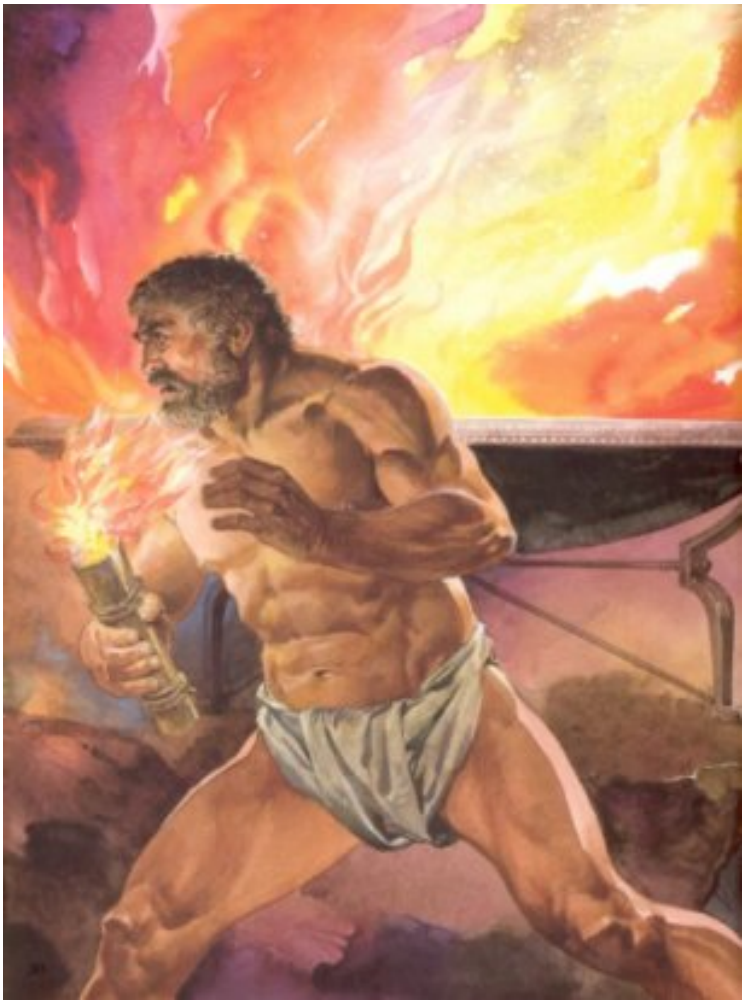

"Hèphaistos: La luce artefice di tutto, il fuoco, il fiore tuo, egli lo ha rubato e ne ha fatto partecipi i mortali."
Aischỳlos, Prometeo Incatenato

"Go forward, Faustus, in that famous art wherein all Nature's treasure is contained."
Marlowe, Doctor Faustus

Solo la fame di conoscenza
vivifica i ricordi.
a Luisa

Contents

List of Figures

List of Tables

Introduction

In this thesis we present the measurement of D^+ meson inclusive production cross section in the low transverse momentum region. The data were collected with the CDF II detector at the Tevatron Collider of the Fermi National Accelerator Laboratory. In particular, we use fully reconstructed candidates in the $D^+ \to K^-\pi^+\pi^+$ mode and its charge coniugate.

The actual QCD theory cannot predict the behavior of the strong interactions in the low transferred 4-momentum region (low Q^2) because in these kinematic conditions the strong coupling constant, α_s, is of the order of the unity. Thus, a perturbative expansion is no longer permitted and the colour confinement behaviour is not understood yet. At present, several phenomenological models have been proposed, but they are able to describe only few aspects of the observed physical quantities and not their whole complexity. Experimental results in this conditions are then crucial to predict new QCD models. The measurement of the differential cross section at low p_T plays an important role in this context allowing to refine the actual knowledge.

This work is part of a specific effort by the CDF Collaboration to measure the inclusive differential cross section of prompt charmed mesons at low p_T. A previous published analysis by the CDF Collaboration in 2003 performed this measurement down to a minimum p_T of the D^+ of 6.0 GeV/c, because they introduced a bias through a trigger selection. To extend the previous measurement down to a $p_T(D^+)$ as low as 1.5 GeV/c, we use the Minimum Bias (MB) and Zero Bias (ZB) data samples. Because of its relatively big mass, the quark c production cross section is several order of magnitude smaller than lighter quarks ones (u, d and s).
One of the main contributions of the present work is the optimization of the candidate selection in order to reduce the light mesons background, 10^4 times larger than the signal.

This thesis is divided into eight chapters.

Chapter 1 : we present the theoretical background of the D^+ meson and its place within the Standard Model (SM). We rimark the uniqueness of this measurement.

Chapter 2 : we briefly describe the Tevatron collider and the CDF II experiment with some emphasis on the subdetectors used for this analysis.

Chapter 3 : we describe the online and offline data selections giving a description of the optimization strategy used to extract the D^+ signal.

Chapter 4 : we present the simulation samples used through the analysis.

Chapter 5 : after a description of the fitting procedure used, the search of the signal is finalized.

Chapter 6 : we evaluate the trigger and the reconstruction efficiencies.

Chapter 7 : the measurement of the inclusive D^+ meson production cross section as a function of the transverse momentum is presented.

Chapter 8 : we conclude remarking the results of this work.

Results will begin soon the internal CDF review process and they will be submitted to an international journal for their prediction.

Sommario

In questo lavoro di tesi presentiamo una misura della sezione d'urto inclusiva di produzione del mesone D^+ nella regione a basso momento trasverso. I dati in analisi sono stati raccolti dall'esperimento CDF II presso il collisonatore di protoni e antiprotoni Tevatron, ubicato al Fermi National Accelerator Laboratory. Più specificamente, utilizziamo i candidati completamente ricostruiti nel canale di decadimento $D^+ \to K^-\pi^+\pi^+$ e il suo coniugato di carica.

L'attuale QCD non può predire il comporatmento delle interazioni forti nella regione a basso quadrimpulso trasferito (basso Q^2) perchè in queste condizioni cinematiche la costante di accoppiamento forte, α_s, è dell'ordine dell'unità. Dunque non è possibile uno sviluppo perturbativo e il confinamento del colore non è ancora compreso. Ad oggi, diversi modelli fenomenoligici sono stati proposti, ma nessuno di questi è in grado di descrivere tutti gli aspetti delle quantità fisiche osservate nella loro complessità. I risultati sperimentali in queste condizioni sono quindi cruciali per predire nuovi modelli di QCD. La misura della sezione d'urto differenziale a bassi p_T riveste un ruolo importante in questo contesto giacché consente di migliorare l'attuale conoscenza. Questo lavoro è parte di uno specifico sforzo della collaborazione CDF di misurare la sezione d'urto inclusiva dei mesoni charmati diretti, nella regione cinematica a basso p_T. Un lavoro precedentemente pubblicato dalla Collaborazione CDF nel 2003 studiava questa misura fino ad un minimo p_T del D^+ di 6.0 GeV/c, perchè introducevano un bias nella procedura di selezione operata dai trigger. Per estendere la precedente misura a $p_T(D^+)$ pari a 1.5 GeV/c, abbiamo utilizzato il campione raccolto solo dai trigger Minimum Bias (MB) e Zero Bias (ZB). A causa della sua grande massa, la sezione d'urto di produzione del quark c è parecchi ordini di grandezza più piccola di quella dei quarks più leggeri (u, d and s).

Uno dei principali contributi di questo lavoro è rappresentato dall'ottimizzazione della selezione dei candidati in modo da ridurre il fondo di mesoni leggeri, 10^4 volte più abbondante del segnale.

Questa tesi è strutturata in otto capitoli.

Chapter 1 : presentiamo le basi teoriche della misura introducendo il mesone D^+

e il suo ruolo nell'ambito del Modello Standard (SM). Inoltre, puntualizziamo l'unicità di questa misura

Chapter 2 : descriviamo brevemente il collisonatore Tevatron e l'esperimento CDF II con particolare minuzia ai subdetectors utilizzati in questa analisi.

Chapter 3 : presentiamo la selezione dei dati, online e offline, fornendo anche una descrizione della strategia d'ottimizzazione utilizzata per estrarre il segnale D^+.

Chapter 4 : mostriamo i campioni di simulazione utilizzati in questa analisi.

Chapter 5 : dopo una descrizione della procedura utilizzata per modelizzare segnale e fondo, viene presentata l'evidenza del segnale.

Chapter 6 : stimiamo l'efficienze di trigger e di ricostruzione.

Chapter 7 : presentiamo la misura inclusiva della sezione d'urto di produzione del mesone D^+ in funzione del momento trasverso.

Chapter 8 : concludiamo riassumendo i risultati di questo lavoro.

Questi risulati saranno presto revisionati dalla collaborazione CDF per essere sottomessi al più presto ad una rivista internazionale per il loro carattere predittivo.

Chapter 1

Theoretical background and motivation

In this chapter we describe the importance and uniqueness of the measurement presented in this thesis. We first illustrate a short description of the Standard Model and of the strong interaction; then we discuss previous similar measurements of the D^+ meson production. We discuss the motivations for this analysis.

1.1 The Standard Model

Several researches performed during centuries have resulted in a remarkable insight into the fundamental structure of matter: the ordinary matter in the universe is found to be made from a few basic building blocks called fundamental particles, governed by four fundamental forces. Our best understanding is described by the Standard Model (SM) of particle physics. The SM is a quantum field theory (QFT) describing all elementary particles and three of the fundamental interactions know today: the weak, the electromagnetic and strong interactions. The first two forces are unified into the electroweak interaction, confirmed in 1983 by the discovery of the W and Z particles at LEP (CERN). Gravitation is still not included in the model, but many efforts move in this direction. Over time and through many experiments, the SM has become established as a well-tested physics theory.

1.1.1 The gauge invariance

The SM Lagrangian is invariant under appropriate transformations, called local gauge transformations. In fact, the three forces observed in nature obey to the local gauge symmetries of the unitary group:

$$G_{SM} = SU(3)_C \otimes SU(2)_L \otimes U(1)_Y \tag{1.1}$$

The $SU(3)_C$ symmetry represents the strong (or color) force. The $SU(2)_L \otimes U(1)_Y$ symmetry represents the weak isospin and hypercharge symmetry, respectively, and it describes the unification between the electromagnetic and the weak forces. The two forces together are referred to as the electroweak force. Because of the gauge-invariance, Noether's theorem states that in the theory there are some conserved charges: the strong charge (or color) C, the weak isospin T (or rather its third component T_3), the hypercharge Y and the electric charge Q. These charges satisfy the Gell-Mann Nishijima relation:

$$Q = \frac{Y}{2} + T_3 \tag{1.2}$$

In this model the elementary particles appear as irreducible representation of the G_{SM} symmetry group. They are divided into two families: fermions (spin 1/2), which satisfy the Fermi-Dirac statistics and bosons (with spin 1), which satisfy the Bose-Einstein statistics. The fermions are classified into two types according to how they interact: *leptons* and *quarks*.

Leptons interact only through the electronweak force. They are described as doublets and singlets of the $SU(2)_L$ group. The doublets are eigenstates of chirality with eigenvalue -1 (*left-handed* eigenstates). The "down" type of each iso-doublets has $T_3 = -1/2$ and electric charge -1, while the "up" type has $T_3 = +1/2$ and neutral electric charge. The neutral leptons are called neutrinos. The charged leptons are called electron e, muon μ and tau τ. Neutrinos interact only via the weak force (they do not carry electric charge) and, as Goldhaber's experiment proved, they can be only eigenstates of chirality with negative eigenvalues, so the *right-handed* fermions in the SM ought to be singlets for $SU(2)_L$ [1]. The three leptonic iso-doublets of the SM are also called leptonic generations:

$$\begin{pmatrix}\nu_e\\ e^-\end{pmatrix}_L \quad \begin{pmatrix}\nu_\mu\\ \mu^-\end{pmatrix}_L \quad \begin{pmatrix}\nu_\tau\\ \tau^-\end{pmatrix}_L \qquad\qquad (e^-)_R \quad (\mu^-)_R \quad (\tau^-)_R \tag{1.3}$$

Quarks interact via electroweak force and they carry the color charge too. In fact, the quarks are triplets of $SU(3)_C$, that is they can exist in three different colors: C = R, G, B. The six quarks are named "flavors" and are: up (u), down (d), charm (c), strange (s), top or thruth (t) and bottom or beauty (b). If one chooses a base where u, c and t quarks are simultaneously eigenstates of both the strong and the weak interactions, the remaining eigenstates are usually written as d, s and b for the strong interaction and d', s' and b' for the weak interaction: d', s' and b' are obtained through a rotation of d, s and b. The rotation matrix is known as the Cabibbo-Kobayashi-Maskawa quark mixing matrix, V_{CKM}:

[1] Antiparticles behave in the opposite way: they are grouped as right-handed doublets and lef-handed singlets of $SU(2)_L$.

$$\begin{pmatrix} d' \\ s' \\ b' \end{pmatrix} = V_{CKM} \begin{pmatrix} d \\ s \\ b \end{pmatrix} = \begin{pmatrix} V_{ud} & V_{us} & V_{ub} \\ V_{cd} & V_{cs} & V_{cb} \\ V_{td} & V_{ts} & V_{tb} \end{pmatrix} \begin{pmatrix} d \\ s \\ b \end{pmatrix} \tag{1.4}$$

The quarks are divided into *left-handed* doublets and *right-handed* singlets of $SU(2)_L$:

$$\begin{pmatrix} u \\ d' \end{pmatrix}_L \quad \begin{pmatrix} c \\ s' \end{pmatrix}_L \quad \begin{pmatrix} t \\ b' \end{pmatrix}_L \qquad (u)_R \quad (d')_R \quad (c)_R \quad (s')_R \quad (t)_R \quad (b')_R \tag{1.5}$$

Again, the "up" type of each iso-doublets has $T_3 = -1/2$ and electric charge -1/3, while the "down" type has $T_3 = +1/2$ and electric charge +2/3. The three quarks iso-doublets are also known as SM generations of quarks.

The generators of the symmetry group G_{SM} are the mediators of the fundamental interactions described in the SM. They are spin 1 elementary particles called *gauge bosons*. The photon, γ, and the vector bosons, $W^{\pm}$ and Z, are the generators of the $SU(2)_L \otimes U(1)_Y$ group (best-known as electroweak generators), while the gluons, g, are the generators of the $SU(3)_C$ group.

1.1.2 The Higgs mechanism

The gauge invariance of $SU(2)_L \otimes U(1)_Y$ implies massless weak bosons and fermions since massive fields would make the theory non-renormalizable. This is in total contradiction with reality where weak bosons (W and Z) and almost all fermions are experimentally observed to be massive. The most accepted solution to this problem is the Higgs mechanism [1] [2]. This mechanism predicts the existence of a scalar field, Φ, whose corresponding lagrangian density has the following form

$$\mathcal{L}_\Phi = (D_\mu \Phi)^\dagger D^\mu \Phi - V(\Phi) \tag{1.6}$$

where:

$$V(\Phi) = \mu^2 \Phi^\dagger \Phi + \lambda (\Phi^\dagger \Phi)^2. \tag{1.7}$$

If $\lambda > 0$ and $\mu^2 < 0$ the potential has a minimum for $\Phi^\dagger \Phi = -\mu^2/2\lambda \equiv v^2/2$. Under this assumption, the field Φ has a non-zero vacuum expectation value (VEV). The electroweak symmetry is spontaneously broken choosing one of a set of degenerate states of minimum energy. According to the Goldstone theorem, fields that acquire a VEV will have an associated massless boson which will disappear, transformed into the longitudinal component of a massive gauge boson. Since the photon is known to be massless, the symmetry is chosen to be broken so that only two fields acquire a vacuum expectation value. Expanding the field Φ around the true minimum of the theory, one obtains:

$$\Phi(x) = \frac{1}{2} e^{i\theta(x)/v} \begin{pmatrix} 0 \\ v + H(x) \end{pmatrix} \tag{1.8}$$

where $H(x)$ is the Higgs field and $\theta(x)$ are non-physical Goldstone bosons. Introducing this representation of Φ the Goldstones bosons vanish and the gauge bosons acquire terms which can be identified as mass terms. From the "broken" lagrangian one finds the following prediction for the mass of the Higgs boson:

$$m_H = \sqrt{-2\mu^2} \tag{1.9}$$

After fourty years of Higgs-hunting, on July 4^{th}, 2012 two of the LHC experiments, ATLAS and CMS, announced that a previously unknown particle with a mass of about 126 GeV/c^2 had been detected [3] [4]; physicists guessed that it was the Higgs boson. On March 2013, their guess has been confirmed [5]. Peter Higgs and Francois Englert were awarded the Nobel Prize in Physics for their confirmed prediction.
In Table 1.1 all the elementary particles in the SM are summerized.

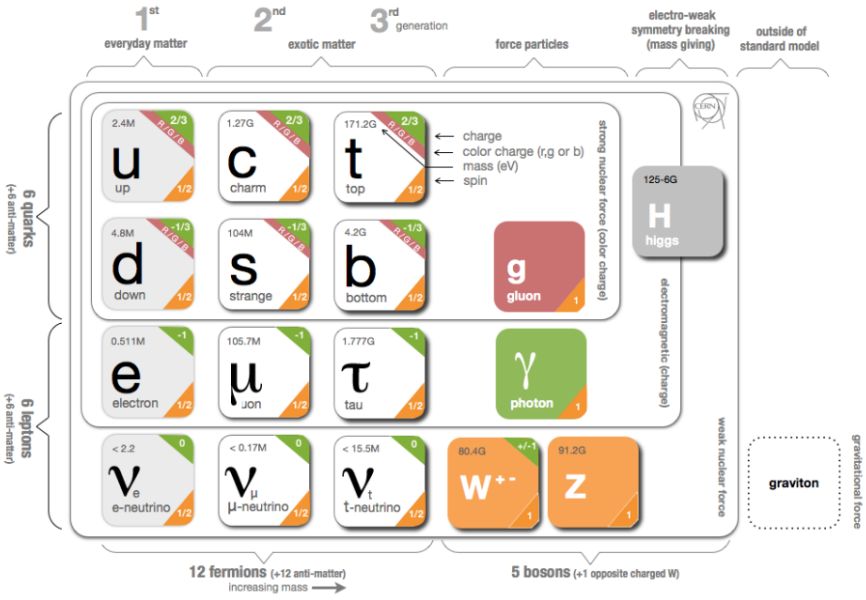

Figure 1.1: *Elementary particles in the SM.*

1.2 Quantum Chromodynamics

Quantum chromodynamics (QCD) is the name of the QFT describing the strong interactions of the colored quarks and gluons. It is based on the non-abelian $SU(3)_C$ gauge group. Quarks possess a color charge (there are three types of color charges, arbitrarily labeled *red*, *blue* and *green*) while gluons carry a color and an anti-color

(for a total of eight possible combinations). A hadron is a color-singlet combination of quarks, anti-quarks and gluons. QCD predictions are well tested at high energies where perturbative approaches are possible because of the small value of the strong coupling constant, α_s (see Figure 1.3). On the other hand, in the low-energy region, QCD becomes a strongly-coupled theory and a perturbative approach can not be applied. QCD is a relativistic QFT of quarks and gluons interacting according to the laws of non-abelian forces between color charges. The QCD Lagrangian is defined as follows:

$$\mathcal{L}_{QCD} = -\frac{1}{4} G^{\mu\nu}_a G^a_{\mu\nu} + \sum_f \bar{q}_f [i\gamma^\mu D_\mu - m_f] q_f \tag{1.10}$$

where q represents the quark field and f for the quark flavors relevant in the interaction, while $G^{\mu\nu}_a$ is the gluon field strength tensor:

$$G^{\mu\nu}_a = \partial^\mu A^\nu_a - \partial^\nu A^\mu_a + g f^{bc}_a A^\mu_b A^\nu_c \tag{1.11}$$

A^ν_a is the gluon field, f^{bc}_a the antisymmetric structure constants and g a constant related to the strong coupling constant, α_S, via the formula $\alpha_S = g^2/4\pi$. D^μ is the gauge covariant derivative, namely

$$D^\mu = \partial^\mu - i\frac{g}{2} A^\mu_a \lambda^a \tag{1.12}$$

The world of hadronic and nuclear physics is originated by this QCD Lagrangian. Quarks and gluons represent the fundamental QCD degrees of freedom. How this elegant and simple-pattern theory can originate the hadrons complexity, is only qualitatively understood by now. The QCD field equations are non-linear since the gluons that mediate the interaction carry color charge and hence they can interact among themselves. This means that even the simplest strongly-interacting system is a multi-body problem: many quark-antiquarks pairs and gluons are always involved.

An intrinsic QCD scale, Λ_{QCD}, is set through the process of the renormalization in quantum field theory: below the QCD scale the standard perturbation theory is no longer valid because the coupling constant becomes larger.

Two of the prominent features of QCD are:

1. **color-confinement**, which means that any strongly interacting system at temperatures below a critical value, T_c (about 0.2 GeV/c), and at low baryon density must be a color singlet at a scale of distance larger than $1/\Lambda_{QCD}$. As a consequence, isolated free quarks cannot exist in nature (quark confinement). The force between quarks diverges with distance; this bounds them into hadrons, such as the proton, the neutron and so on. Although analytically unproven, the color confinement of QCD is a theoretical conjecture consistent with experimental facts. To prove it in QCD is still a challenge that has not been met.

2. **asymptotic freedom**, which states that the interaction strength between quarks, α_S, becomes smaller as the distance between them gets shorter.

No phase-transition line separating these two properties is theorized and observed: confinement is dominant in low-energy scales while asymptotic freedom becomes dominant as energy increases.

It has been said that QCD is the most elegant theory among the renormalisable QFTs based on the $SU(3)$ gauge group. The QCD Lagrangian has several other important "accidental" symmetries: the discrete symmetries parity, charge conjugation and flavour conservation are the main examples. The number of quarks minus that of antiquarks for each flavour is conserved, corresponding to an automatic invariance of the Lagrangian under phase rotations of the quark fields of each flavour separately.

Still today, after about fourty years from the first QCD theoretical formulation, strong interactions are not completely understood: features of low transferred momentum QCD phenomena are far to be theoretically predicted. That is why experiments which test QCD in the non-perturbative regime are crucial to improve our understanding of the strong interactions.

1.2.1 QCD coupling constant

The qualitative understanding of QCD is based on the classical calculation of the renormalization scale dependence of the QCD coupling constant α_s. The best way to show this dependency is to define the so-called β-function at an energy scale μ:

$$\beta(\alpha_s) \equiv \frac{\mu}{2}\frac{\partial \alpha_s}{\partial \mu} = -\frac{\beta_0}{4\pi}\alpha_s^2 - \frac{\beta_1}{8\pi^2}\alpha_s^3 - \dots \tag{1.13}$$

where

$$\beta_0 = 11 - \frac{2}{3}n_f \tag{1.14}$$

$$\beta_1 = 51 - \frac{19}{3}n_f \tag{1.15}$$

and n_f is the number of *effective quarks* (i.e. quarks with mass less than μ). One introduces the arbitrary scale Λ for solving this differential equation for α_s and to provide the μ dependence of α_s. A first order approximate solution is the following:

$$\alpha_s(\mu^2) = \frac{\alpha_s(\Lambda^2)}{1 + \frac{\alpha_s(\Lambda^2)}{12\pi}\beta_0 ln\frac{\mu^2}{\Lambda^2}} \tag{1.16}$$

The solution demonstrates the two famous QCD properties: asymptotic freedom

$$\alpha_s \xrightarrow{\mu \to +\infty} 0 \tag{1.17}$$

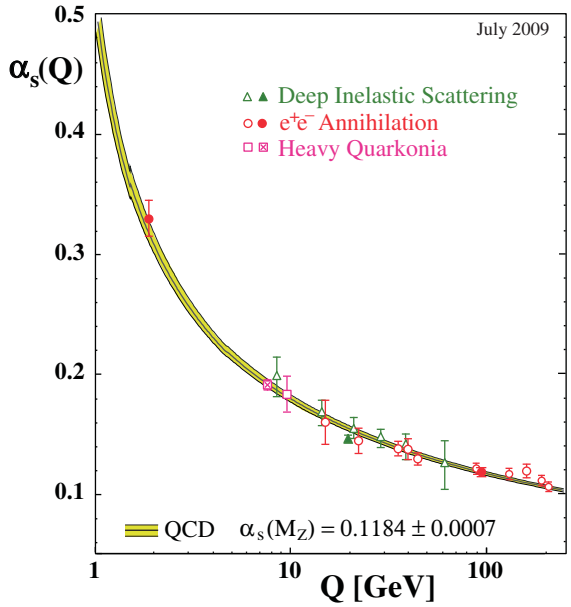

Figure 1.2: *The running of the strong coupling constant as a function of the transferred momentum Q [6].*

and the strong coupling at scales below $\mu \sim \Lambda$. As shown in Figure 1.2, it is possible to roughly divide the strong interaction physics into two regions as a function of the energy of the process: the area of perturbative QCD (pQCD) for high transferred momentum (small α_S) and that of non-perturbative QCD for low transferred momentum (big α_S). The pQCD has been well-tested in quantitatively describing phenomena where Feynman standard rules apply. In the perturbative regime, the magnitude of the coupling constant is the fundamental parameter for theoretical predictions. Its value as a function of the energy determines a host of phenomena, such as scaling violations in deep inelastic scattering, the τ lifetime, high-energy hadron collisions, heavy-quarkonium (in particular bottomonium) decay, e^+e^- collisions and jet rates in ep collisions. One of the most important example is the e^+e^- annihilation in the area of the Z^0 boson: the multi-particle hadronic final-state system reveals the pQCD physics in the form of the quark and gluon jets. The different values of the coupling constant derived from these processes are listed in Figure 1.3; they are consistent with each other leading to an average value of [6] :

$$\alpha_s(m_Z^2) = 0.1184 \pm 0.0007. \tag{1.18}$$

The non-perturbative area is quantitatively much less understood: important questions still wait to be answered.

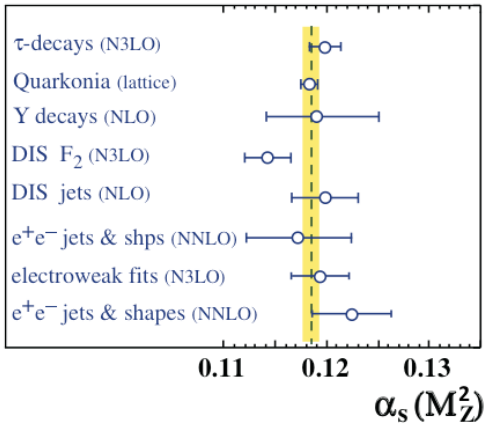

Figure 1.3: *Summary of $\alpha_s(m_Z^2)$ measurements and world average value [6].*

1.2.2 Non-perturbative QCD

The theoretical approaches to the non-perturbative QCD region are essentially two: the Lattice QCD (LQCD) and the Effective Field Theory (EFT).

LQCD is a numerical approach. This approach uses a discrete set of space-time points, the so-called lattice, to reduce the analytically intractable path integrals of the continuum theory to a very difficult numerical computation which is then carried out on supercomputers, constructed for precisely this purpose. The discretization is removed by letting the lattice spacing tend to zero, thus restoring the continuum. Even if LQCD theoretical principles were originally proposed in 1974, this approach has made enormous progress over the last decades, mainly due to the empowerment of the computer technology.

An EFT is a theoretical prescription for constructing theory spanning multiple energy scales, under a series of approximations. For instance, if we assume negligible mass of the u, d and s quarks with respect to Λ_{QCD}, it is possible to formulate an EFT equivalent to QCD in a certain scale range. The most successful approach is the heavy-quark effective theory (HQET) for hadrons contaning a quark c, b or t because their mass is $m_Q \gg \Lambda_{QCD}$. In the limit $m_Q \to +\infty$ the heavy quark becomes on-shell and the dynamics becomes independent of its mass. The hadronic matrix elements can be expanded as a power series in $1/m_Q$ resulting in symmetry relations between various matrix elements [7].

In recent years a great variety of EFTs with quark and gluon degrees of freedom have been developed. The best solution is obtained combining LQCD with EFT because there is a remarkable simplification in the theoretical calculations.

1.3 Quark c and the D mesons

After the discovery of several hadrons made up by u, d and s quarks, the existence of a fourth quark had been speculated by a number of authors around 1964: its prediction is usually credited to Sheldon Glashow, John Iliopoulos and Luciano Maiani in 1970 within the so-called GIM mechanism.

A firmly established experimental fact is that flavor changing weak processes obey certain selection rules. One of them, known as the $\Delta S = 1$ rule, states that the flavor number, in this case strangeness S, changes by at most one unit. A second rule is that flavor changing neutral current (FCNC) processes, must occur only at second order in the weak interactions[2]. In order to explain the non observation of FCNC processes at tree level, it was postulated the existence of a second up-type quark, which group with the s quark into a doublet of $SU(2)_L$. Thus, Cabibbo universality principle [8] for the charged weak current was generalised as follows:

$$J_\mu(x) = \bar{U}(x)\gamma_\mu(1+\gamma_5)CD(x) \tag{1.19}$$

with

$$U = \begin{pmatrix} u \\ c \end{pmatrix}; D = \begin{pmatrix} d \\ s \end{pmatrix}; C = \begin{pmatrix} cos\theta_C & sin\theta_C \\ -sin\theta_C & cos\theta_C \end{pmatrix} \tag{1.20}$$

where θ_C is the Cabibbo angle. As a result, the neutral current will be diagonal, ensuring that FCNC processes will not be generated at the tree level.

In 1974, independently, two research groups, one at the Stanford Linear Accelerator Center, headed by Burton Richter, and one at the Brookhaven National Laboratory, headed by Samuel Ting, announced the discovery of the first meson consisting of a charm quark and a charm antiquark, namely J/Ψ (charmonium).

c quark occupies a unique place among up-type quarks, because it is the only up-type quark whose hadronization (and the consequent decay) can be studied. This is due to the fact that, on the heavy side of the spectrum, the t quark decays before it can hadronize, while on the lighter side, the u quark can be considered stable. In fact, u quark forms only two kinds of neutral hadron which decay weakly, neutrons and pions: the decay of the former is due to the weak decay of quark d and, in the latter, quark and antiquark of the first family annihilate each other.

In order to keep the theory consistent and manage consequent possible anomalies, the main features of charm quarks were predicted to be the followings:

- c quarks have the same coupling as u quarks, but their mass is much heavier, namely about 2 GeV/c^2;

[2]The best experimental evidence is the measurement of the branching ratio $\frac{Br(K^+\to\pi^+\nu\bar{\nu})}{Br(K^+\to\pi^0\mu^+\nu_\mu)} \sim 10^{-8}$, where $K^+ \to \pi^+\nu\bar{\nu}$ is a neutral current process with $\Delta S = 1$ and $K^+ \to \pi^0\mu^+\nu_\mu$ is a charged current process with $\Delta S = 1$.

- They form charged and neutral hadrons, of which (in the $C = 1$ sector) three mesons and four baryons that decay only weakly with lifetimes of about $10^{-13}s$. The D family is composed by the D^0, D^+, D^{*+}, D_s meson and their antiparticles.

- Charm decay produces direct leptons and preferentially strange hadrons.

Still today, after about 50 years of research in the charm sector, these assumptions are reliable. Since the charm is an $up-type$ quark, loops diagrams cannot involve the heavy top quark, so the SM predictions for charm hadronization and decay are smaller by many orders of magnitude than the down-type corresponding processes. Intermediate meson-states are expected to contribute at the 10^{-4} level overshadowing the short-distance contributions. SM loop-mediated processes are very unlikely to be observed, while, new physics may enhance them and it could be easier to detect them in the charm system than in the bottom system. Experimentally, charm has some distinct advantages compared to the B-system: fully reconstructed modes are characterized by branching fractions at the level of the 10%, much more higher than branching ratios to fully reconstruct a B-decay (10^{-5}). Moreover, very specific tags are present in the charm decays, allowing distinguishable signatures. For instance about one third of the D^0 comes from a $D^{*+} \to D^0\pi^+$ decay: the charge of the slow pion tags the D^0 flavor at production with an efficiency of almost 100 %.

The mixing of neutral mesons is studied in the case of D^0 - $\bar{D}^0$ oscillations. Two parameters are used to describe the mixing phenomenon: $x_D \equiv \frac{\Delta M_D}{\Gamma_D}$ and $y_D \equiv \frac{\Delta\Gamma_D}{\Gamma_D}$, where ΔM_D is the mass difference between D^0 and $\bar{D}^0$ and $\Delta\Gamma_D$ is the difference between their decay rates. The box-diagram theoretical predictions for x_D and y_D are at the 10^{-5} level [9]. New physics has a little effect on $\Delta\Gamma_D$, but may have significant contributions to ΔM_D up to values of x at the 1 % level. Contributions from non-perturbative QCD tend to increase $\Delta\Gamma_D$ but the effect on ΔM_D is small. An observation of the x at the percent level together with a strong limit on y at the 10^{-3} level would be a strong indication for new physics. In 2007 Belle [10] and BABAR [11] obtained the first evidence for D^0 - $\bar{D}^0$ mixing, which had been searched for more than two decades. These results were later confirmed by CDF [12]. There are now numerous measurements of mixing in the charm sector, with different levels of sensitivity. Many channels have been studied: $D^0 \to K^+l^-\nu$, $D^0 \to K^+K^-$, $D^0 \to \pi^+\pi^-$, $D^0 \to K^+\pi^-$, $D^0 \to K^+\pi^-\pi 0$, $D^0 \to K^0_S\pi^+\pi^-$ and $D^0 \to K^0_S K^+K^-$.

The LHCb and CDF experiments have obtained the evidence for direct CP violation in D^0 decays [13] [14]. They studied the channels: $D^0 \to K^+K^-$ and $D^0 \to \pi^+\pi^-$, measuring the difference: $A_{CP}(K^+K^-) - A_{CP}(\pi^+\pi^-)$ where:

$$A_{CP}(K^+K^-) = \frac{\Gamma(D^0 \to K^+K^-) - \Gamma(\bar{D}^0 \to K^+K^-)}{\Gamma(D^0 \to K^+K^-) + \Gamma(\bar{D}^0 \to K^+K^-)} \tag{1.21}$$

and

$$A_{CP}(\pi^+\pi^-) = \frac{\Gamma(D^0 \to \pi^+\pi^-) - \Gamma(\bar{D}^0 \to \pi^+\pi^-)}{\Gamma(D^0 \to \pi^+\pi^-) + \Gamma(\bar{D}^0 \to \pi^+\pi^-)} \tag{1.22}$$

The result excludes the no-mixing hypothesis with a probability corresponding to 95% C.L. and represents the first evidence of oscillations from a single measurement in the charm sector. CDF measured a value of $A_{CP}(K^+K^-) - A_{CP}(\pi^+\pi^-) = (-0.62 \pm 0.21(stat.) \pm 0.10(syst.))\%$, while LHCb a value of $A_{CP}(K^+K^-) - A_{CP}(\pi^+\pi^-) = (-0.82 \pm 0.21(stat.) \pm 0.11(syst.))\%$.

1.4 Charmed hadrons production and D^+ cross section measurements

Many experimental and theoretical studies have been made about the production of charmed hadrons (X_c) at hadron colliders. Charm physics has been deeply studied by fixed target experiments (SELEX, E791 and E687/FOCUS). CLEO results were the first to be competititve with the best fixed-target experiments. The last phase of the experiment, the 3-year special run CLEO-C, was planned to measure at various thresholds the absolute branching ratios of the D meson decays, very hard to be measured otherwise. Important results on the charm physics come from the PHENIX and the STAR experiments at the BNL Relativistic Heavy Ion Collider (RHIC). Both collaborations reported the measurement of non-photonic electron production through charm and bottom decays in pp, dAu and AuAu collisions at $\sqrt{s} = 200\ GeV$ [15] [16]. The STAR Collaboration also presented mid-rapidity open charm spectra from direct reconstruction of decays in dAu collisions and indirect e^+e^- measurements via charm semileptonic decays in pp and dAu collisions at the center of mass energy, $\sqrt{s}$, of 200 GeV [17]. These results at the RHIC only covered a very limited low-p_T range. So far, many of the world best charm measurements come from BaBar and Belle because of their high statistics. Actually Alice and LHCb are the most powerful c-factory all over the world. The latest result concerning the charm physics is the measurement of the inclusive open charm production in p-p and Pb-Pb collision performed by the ALICE collaboration [18]. A preliminary measurement of the D^0, D^+ and D^{*+} differential cross sections at $\sqrt{s} = 7\ TeV$ was released. The total charm production cross section dependence on $\sqrt{s}$ was estimated using the extrapolation of the D meson cross section measurements to the full kinematic phase space. In Figure 1.4 it is shown the $pp \to c\bar{c}$ cross section as a function of the centre of mass energy for various experiments.

One of the important contributions in the charm sector comes from CDF. Before CDF, charm physics had not been done at $p\bar{p}$ collider. The CDF Silicon Vertex Tracker (SVT) was designed to collect large samples of B hadrons in fully hadronic final states, but thanks to this particular tracker, CDF was also able to collect huge samples containing D mesons decays, becoming competitive in terms of sensitivity

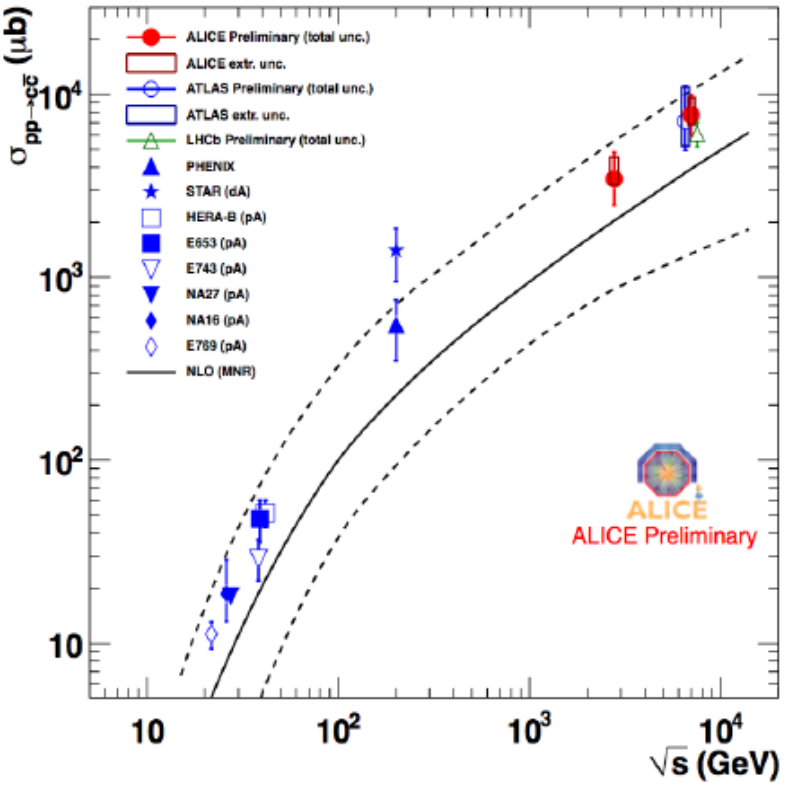

Figure 1.4: *Total charm production cross section as a function of centre of mass energy for various experiments [18].*

to previous charm factories [19].
On the other side some limits for charm physics at CDF are due to physics and detector constraints:

- **Limited particle identification.** The Time-Of-Flight detector had π/K separation $\geq 2\sigma$ for $p_T \leq 1.6$ GeV/c, while dE/dx could also help a bit in these conditions. However, CDF had no powerful PID over the full momentum spectrum of interest.

- **Secondary charm.** B hadrons preferentially decay into charm hadrons. Due to the long B lifetime, charm hadrons could be produced at a significant distance from the primary vertex (PV), resulting in a bias to the proper time measurement if the B decay vertex was not reconstructed. The impact parameter distribution of the charm candidate can be very helpful to disentangle direct from secondary charm. In Figure 1.5 is shown a *prompt* D^+ (directly produced in the $p\bar{p}$ interaction) and a *secondary* D^+ (produced from a B^- decay).

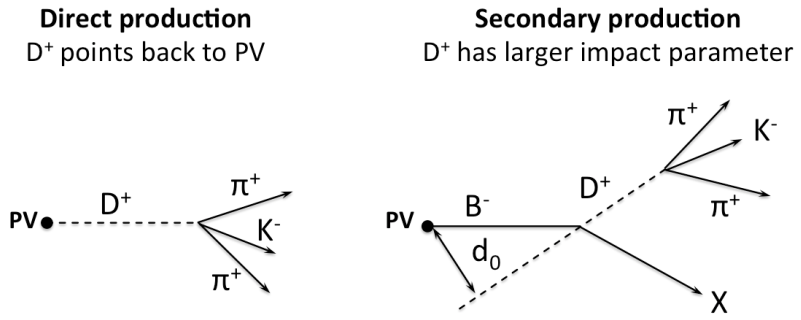

Figure 1.5: *The impact parameter for prompt and secondary D^+ mesons in the r-ϕ plane.*

In 2003, the CDF Collaboration published the measurements of the differential cross sections for the production of charmed mesons as a function of the transverse momentum for $p_T \geq 5.5\ GeV/c$ at $\sqrt{s} = 1.96\ TeV$ [20]. Figure 1.6 shows CDF differential cross section measurements for the mesons of the D family.

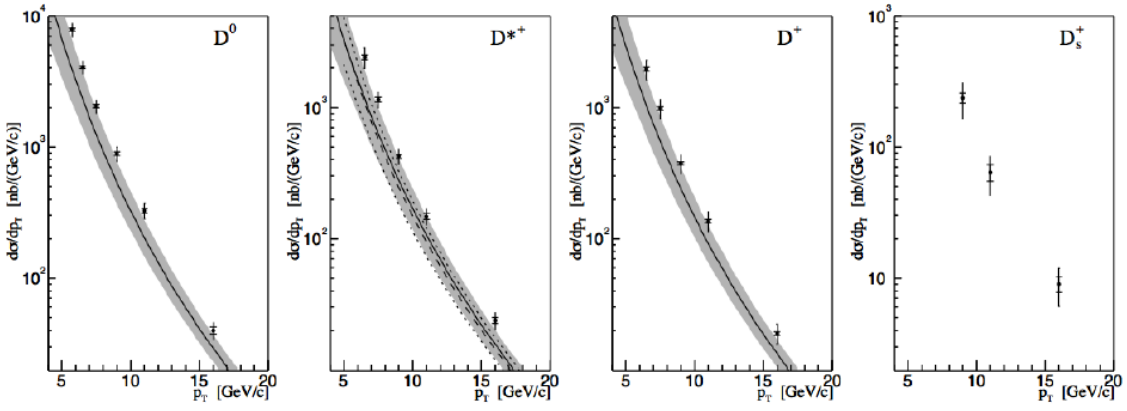

Figure 1.6: *The differential cross section measurements for the mesons of the D family at $\sqrt{s} = 1.96\ TeV$ at CDF II. The inner bars represent the statistical uncertainties, while the outer bars are the quadratic sum of the statistical and systematic uncertainties. The solid and dashed curves represent the theoretical predictions and the shaded bands indicate uncertainties. For the D_s^+ production there is no theoretical prediction [20].*

Theoretically, the cross section for the inclusive production of X_c mesons can be modeled by the convolution of universal parton distribution functions (PDFs) and universal fragmentation functions (FFs) with calculable hard-scattering cross sections via perturbative approach. The universality of the PDFs and FFs guarantees

unique predictions for the cross section of the production of heavy-flavored hadrons. The theoretical prediction using this method in case of X_c production at the energy available at the Tevatron [21] [22] were compared to CDF results and a not so good agreement between theory and experimental results was found. As evident in Figure 1.6, theory is in agreement with the experimental data if we consider the overlapping of the errors, but the central prediction tends to underestimate the data points in most of the considered p_T range; this is particular evident in the lower end of the spectrum where the prediction undershoots by a factor of about 1.5 the observed data.

Tevatron shut down on September 30^{th}, 2011 after collecting about 10/fb of data at $\sqrt{s}$ = 1.96 TeV. Before the final shut down, additional scans at lower center of mass energies were performed: $\sqrt{s}$ = 300 GeV and $\sqrt{s}$ = 900 GeV. Still today, the Tevatron sample acquired at $\sqrt{s}$ = 900 GeV is the largest sample at this center of mass energy ever collected at an hadronic collider. The measurement of the D^0 meson differential production cross section, extended to the low p_T range ($1.5\ GeV/c \leq p_T \leq 14.5\ GeV/c$) at $\sqrt{s}$ = 1.96 TeV and $\sqrt{s}$ = 900 GeV, is now under the internal collaboration review and it will be submitted soon to international journals for publication [23]. In Figure 1.7 we show a preliminary result of this measurement.

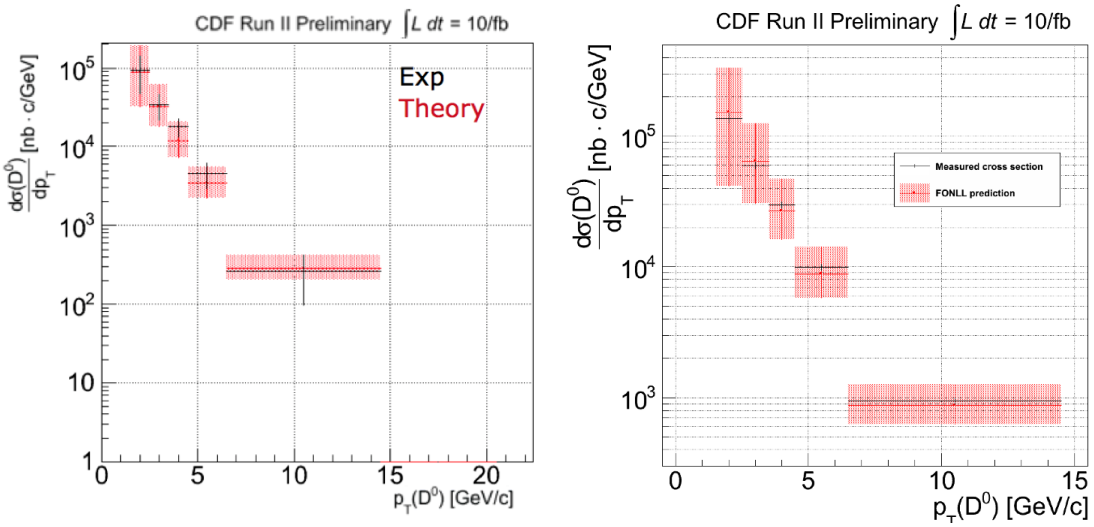

(a) $\sqrt{s}$ = 900 GeV. (b) $\sqrt{s}$ = 1.97 TeV.

Figure 1.7: *Low p_T D^0 meson differential production cross section at different center of mass energies at CDF II. The shaded areas indicate the theoretical prediction [23].*

New measurements in the region where α_S becomes too big for perturbative calculation and the color confinement behavior is not well understood are crucial. The extension of the previous CDF published measurement for the $D^+ \to K^-\pi^+\pi^+$ cross section at low p_T can give an additional important lever arm to refine the

current knowledge and theory.

Recently, other measurements of charm production cross-section at low-p_T became available from the ALICE and LHCb experiments at the CERN LHC proton-proton collider. However, the present measurement maintains its uniqueness. In fact the different experimental conditions won't reproduce Tevatron ones both in terms of initial state ($p\bar{p}$) and center of mass energy ($\sqrt{s} = 1.96\,TeV$). Thanks to the sample collected at $\sqrt{s} = 900\,GeV$, this measurement could also be extended to this different center of mass energy.

In this work we perform the inclusive measurement of the D^+ meson differential production cross section as a function of the transverse momentum at CDF II:

$$\frac{d\sigma_{D^+\to K^-\pi^+\pi^+}}{dp_T}(p_T; |y| \le 1) = \left.\frac{\frac{N_{D^+}+N_{D^-}}{2}(p_T)}{\Delta p_T \cdot L \cdot \varepsilon_{trig} \cdot \varepsilon_{rec}(p_T) \cdot Br(D^+ \to K^-\pi^+\pi^+)}\right|_{|y|\le 1} \quad (1.23)$$

where:

- N_{D^+} and N_{D^-} are the yields of the D^+ and D^- signals in each bin of p_T. We report the cross section only for D^+ mesons while we measure the yields for both, D^+ and D^- mesons. We include a factor $1/2$ because what is actually measured is the average cross section for D^+ and D^- mesons. We postulate charge invariance in the production process through the strong interaction.
- Δp_T is the bin width.
- L is the integrated luminosity of the data sample.
- ε_{trig} is the trigger efficiency.
- ε_{rec} is the global reconstruction efficiency of our candidates. This parameter takes into account geometrical and kinematical acceptances as well as the detector reconstruction efficiency of the signal.
- $Br(D^+ \to K^-\pi^+\pi^+)$ is the decay branching ratio of the channel used in this analysis.
- $|y| \le 1$ is the rapidity range considered: the central region of the detector.

Chapter 2

Accelerator and detector

The measurement described in this thesis is based on a data sample collected by the CDF II detector during Run II operations at the Fermilab's Tevatron Collider. In this chapter we briefly describe the Tevatron collider accelerator and the CDF II detector, mainly focusing on the subsystems used for this analysis such as the trigger and the tracking systems.

2.1 The Tevatron collider

The Tevatron located at the Fermi National Accelerator Laboratory (FNAL or Fermilab) in Batavia (Illinois, USA) was a proton-antiproton ($p\bar{p}$) collider. It produced collisions at center of mass energy of $\sqrt{s}$ = 1.96 TeV. It was a circular superconducting magnets synchrotron, with a 1 km radius. It started operating in 1975, producing its first $p\bar{p}$ collision in 1985 and since then it had undergone extensive upgrades and improvements till it was shut down on September 30^{th}, 2011. The machine collided 36×36 bunches every $396\,ns$. In order to reach $p\bar{p}$ interactions at this energy, several preparation and acceleration steps were needed; Figure 2.1 shows the arrangement in the laboratory area of all the machines involved.

2.1.1 Luminosity and center of mass energy

The performance of a collider is evaluated in terms of two key parameters: the available center of mass energy, $\sqrt{s}$, and the instantaneous luminosity, $\mathcal{L}$. In the measurement of the cross section of a given process, the luminosity is fundamental because it represents the proportionality between the rate of the process, R, and its cross section σ:

$$\mathrm{R[events\ s^{-1}]} = \mathcal{L}\ [\mathrm{cm^{-2}s^{-1}}] \times \sigma\ [\mathrm{cm^{2}}] \tag{2.1}$$

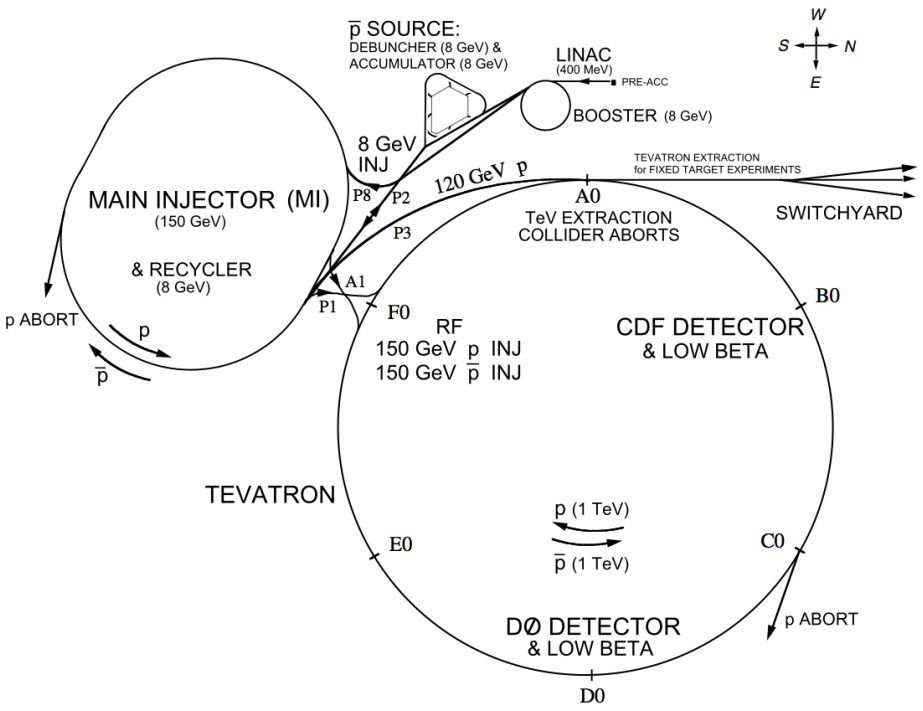

Figure 2.1: *The Tevatron Collider chain at Fermilab.*

R is the product of σ, which is set by the physics of the process, and $\mathcal{L}$, that is purely due to the machine. The cross section is constant in time, so the time integral of the luminosity (*integrated luminosity*) is therefore a measurement of the expected number of events, N, produced in a finite time ΔT:

$$N(\Delta T) = \sigma \int_{\Delta T} \mathcal{L}(t)\, dt \tag{2.2}$$

Assuming an ideal head-on $p\bar{p}$ collision with no crossing angle between the beams, the instantaneous luminosity can be written as follows:

$$\mathcal{L} = 10^{-5} \frac{N_p N_{\bar{p}} B f \beta\gamma}{2\pi\beta^* \sqrt{(\epsilon_p + \epsilon_{\bar{p}})_x (\epsilon_p + \epsilon_{\bar{p}})_y}} \mathcal{H}(\sigma_z/\beta^*) \ [10^{30}\mathrm{cm}^{-2}\mathrm{s}^{-1}] \tag{2.3}$$

$\mathcal{L}$ depends on the following Tevatron parameters: the number of circulating bunches in the ring (B = 36), the revolution frequency (f = 47.713 kHz), the Lorentz relativistic factor ($\beta\gamma$ = 1045.8 at 980 GeV), the average numbers of protons ($N_p \approx 2.78 \times 10^{12}$) and antiprotons ($N_{\bar{p}} \approx 8.33 \times 10^{11}$) in a bunch, an empiric "hourglass" factor ($\mathcal{H}$ = 0.6-0.7), which is a function of the ratio between the longitudinal r.m.s. width of the bunch ($\sigma_z \approx 60$ cm) and the "beta function[1]" calculated at the interaction

[1]The beta function (or betatron function) is the function that parametrize all the linear properties of the beam.

point ($\beta^* \approx 31$ cm) and the 95% normalized emittances of the beams ($\epsilon_p \approx 18\ \pi$ mm mrad and $\epsilon_{\bar{p}} \approx 13\ \pi$ mm mrad after injection).

The most limiting factor of the Tevatron luminosity was the number of $\bar{p}$ per bunch because of their low production efficiency [2].

$\sqrt{s}$, instead, defines the accessible phase space for the production of resonances in the final states; this Tevatron parameter was increased after the upgrade from Run I to Run II moving from 1.8 to 1.96 TeV thanks to an improvement of the performances of the superconducting-magnet cooling system. The $\sqrt{s}$ value is extremely important because it fixes the upper limit for the masses of the particles produced in the $p\bar{p}$ interaction.

The period of a continuous procedure of collider operations using the same collection of protons and antiprotons was called a *store*. Further details about the Tevatron Collider can be found in [24].

2.1.2 Protons beam

The acceleration cycle started with the production of protons from ionized hydrogen atoms, H^-, which were accelerated to 750 keV by a *Cockroft- Walton* electrostatic accelerator. Pre-accelerated H^- ions were then injected into the *LINAC* (LINear ACcelerator), where they were accelerated up to 400 MeV by passing through a 150 m long chain of radio-frequency (RF) accelerator cavities. To obtain protons, the H^- ions were passed through a carbon foil which stripped their electrons off. The resulting protons were then injected to the *Booster* (see Figure 2.1), a rapid cycling synchrotron (with a radius of 75.5 m) that accelerated the protons up to 8 GeV and compacted them into bunches. Each turn around the Booster, the protons accrued about 500 keV of kinetic energy. The protons were then transfered to a synchrotron, called the *Main Injector*, which brought their energy to 150 GeV: this was the beginning of the final injection process into the Tevatron, called "shot". Inside the Main Injector several bunches were coalesced into one for Tevatron injection.

The last stage of the process was the transfer to the Tevatron.

2.1.3 Antiprotons beam

The production of the antiproton beam was significantly more complicated. The cycle started with extracting a 120 GeV proton beam from the Main Injector onto a stainless steel target. This process produced a variety of different particles, among which there were antiprotons. The particles came off the target at many different angles and they were focused into a beam line with a lithium lens. In order to select

[2] The difficulty for collimating $\bar{p}$ into bunches and their transfer through the subsequent accelerator stages were the main factors that caused low $\bar{p}$ production efficiency.

only the antiprotons, the beam was sent through a pulsed magnet which acted as a charge-mass spectrometer. The emerging antiprotons had a bunch structure similar to that of the incident protons and were stored in a *Debuncher*. It was a storage ring where the momentum spread of the $\bar{p}$ was reduced while maintaining a constant energy of 8 GeV, via stochastic cooling stations. Many cycles of Debuncher caused the destruction of the bunch structure which resulted in a continuous beam of antiprotons. At the end of the process the monochromatic antiprotons were stored in the *Accumulator* (see Figure 2.1), which was a triangle-shaped storage ring where they were further cooled and stored until the cycles of the Debuncher were completed. After the accumulator had collected a sufficient amount of antiprotons ($6{\cdot}10^{11}$), they were transferred to the *Recycler*, which was an 8 GeV storage ring made of permanent magnets and further cooled using stochastic cooling and accumulated. When a current sufficient to create 36 bunches with the required density was available, the $\bar{p}$ were injected into the Main Injector. Here their energy was raised to 150 GeV and they were transferred to the Tevatron.

2.1.4 Tevatron

The Tevatron was a synchrotron, 1 Km in radius, which employed superconducting Nb-Ti alloy filaments embedded in copper as magnet coils. It kept both protons and antiprotons in the same beampipe, revolving in opposite directions. When 36 bunches of both protons and antiprotons were circulating in the Tevatron, the energy of the machine was increased in about 10 seconds from 150 to 980 GeV and the collisions began at the two interaction points: DØ (where the homonym detector was located) and BØ (home for CDF II). Special quadrupole magnets (*low-β squeezers*) located at both extremities of the detectors along the beam pipe "squeezed" the beam to maximize the luminosity inside the detectors. A roughly Gaussian distribution of the interaction region along the beam axis was achieved ($\sigma_z \approx 28$ cm) and its center was shifted on the nominal interaction point by the fine tuning of the squeezers.
Only when the beam profile was narrow enough and the conditions were safely stable, the detectors were turned on and the data acquisition started. This was the end of the shot.

The inter-bunch crossing was 396 ns and this defined an overall time constant which influenced the whole detector design: on this parameter depended the choice of the active parts, the design of the readout electronics, the structure of the trigger, etc. The pile up, i.e. the number of overlapping interactions for each bunch crossing, was a function of the instantaneous luminosity and followed a Poisson distribution (see Figure 2.2). The average pile up was approximately 10 when the luminosity was at Tevatron's peak of $\mathcal{L} \approx 4 \times 10^{32}[\mathrm{cm}^{-2}\mathrm{s}^{-1}]$. Each time that at least one of the CDF II triggers fired, an *event* was labeled with an increasing number. Events were

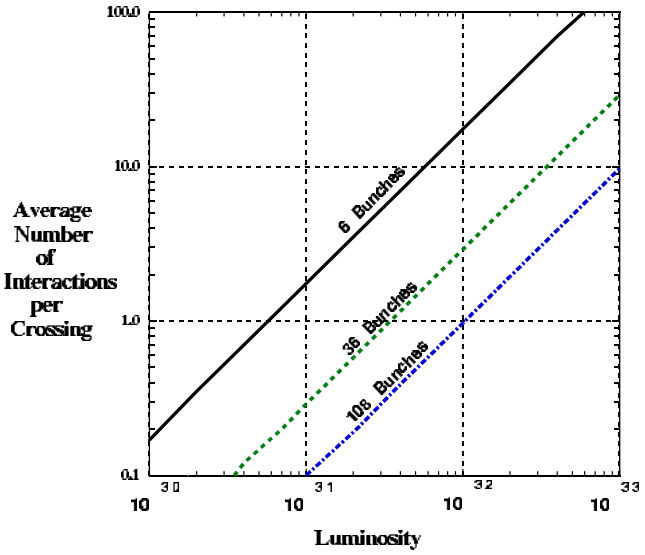

Figure 2.2: *Average number of interactions per crossing as a function of the luminosity (cm^{-2} s^{-1}) and the number of bunches circulating in the Tevatron.*

grouped into *runs*; a run was a period of continuous operation of the CDF II Data Acquisition (DAQ). Many different situations could require the Data Acquisition (DAQ) to be stopped and restarted (beginning in this way a new run) including the need to enable or disable a subdetector, a change in the Trigger Table, a problem in the trigger/DAQ chain, etc... Several parameters of the CDF II operations (e.g. the position of the beam) were stored in a database on a run-averaged format. While collisions took place the luminosity decreased exponentially[3] because of the beam-gas and beam-halo interactions. In the meantime, antiproton production and storage continued. When the antiproton stack was sufficiently large ($\simeq 4 \times 10^{12}$ antiprotons) and the circulating beams were degraded the detector high-voltages were switched off and the store was dumped. The beam was extracted via a switch-yard and sent to an absorption zone. Beam abortion could occur also accidentally when the temperature of a superconducting magnet shifted above the critical value and a magnet quenched destroying the orbit of the beams. The time between the end of a store and the beginning of collisions of the next one was typically $\sim$ 2 hr; during this time CDF II crew usually performed calibrations of the sub-detectors and test runs with cosmics.

As stated in the proposal of Tevatron Run II, the goal was the accumulation of 2/fb at $\sqrt{s}$ = 2 TeV with instantaneous luminosity peaks up to $2 \times 10^{32}[\mathrm{cm}^{-2}\mathrm{s}^{-1}]$. The performance was always well beyond these expectations. The center of mass energy was 1.96 TeV, the peak luminosity, as shown in Figure 2.3, was almost regularly >

[3]The decrease is about a factor of 3 (5) for a store of $\sim$ 10 (20) hrs.

$2 \times 10^{32}[\mathrm{cm}^{-2}\mathrm{s}^{-1}]$ after 2006 (with usual peaks at $4 \times 10^{32}[\mathrm{cm}^{-2}\mathrm{s}^{-1}]$ in the last years of operations) and the crossing time was equal to 396 ns.

The total luminosity delivered by the Tevatron during its activity was about $12/fb$, but only $\sim 10.3/fb$ of data were "acquired" on tape: these are the data used for this analysis. Figure 2.4 shows the trend of Tevatron's integrated and initial luminosity as function of time and store number.

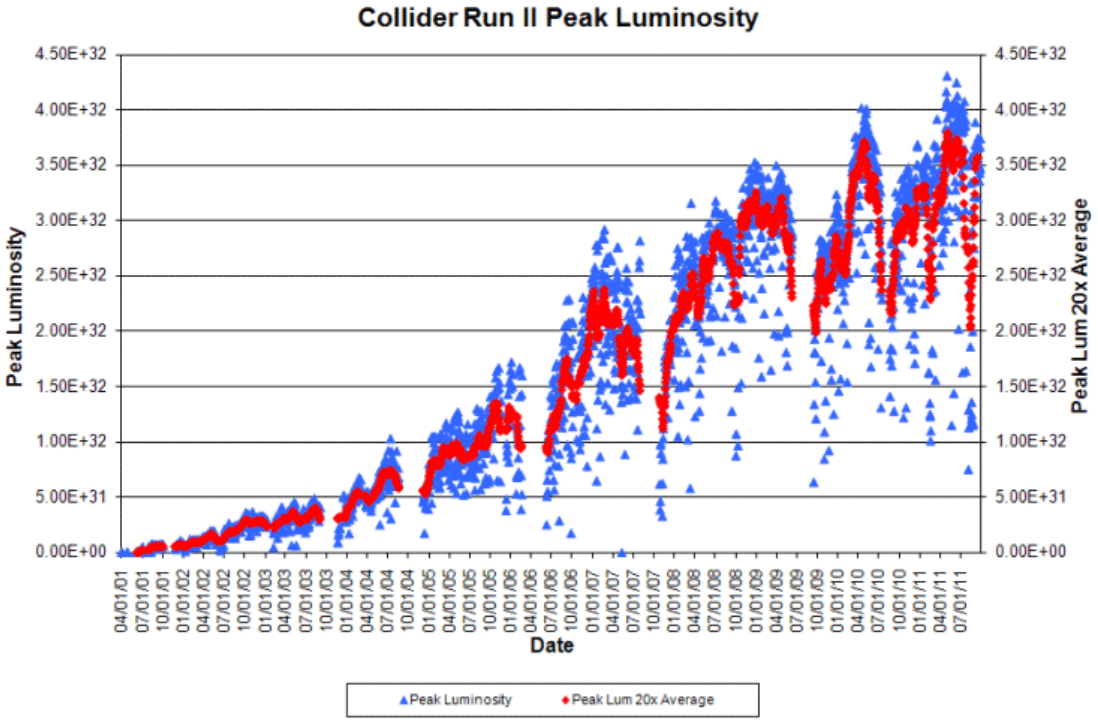

Figure 2.3: *Initial luminosity as a function of the time (or store number).*

2.2 The CDF II experiment

The CDF II detector was a large multi purpose solenoidal magnetic spectrometer surrounded by 4π, fast, projective calorimeters and fine-grained muon detectors. It was installed at the BØ interaction point of the Tevatron (see Figure 2.1) and it was designed to study 1.96 TeV $p\bar{p}$ collisions. The original facility, commissioned in 1985, was subjected to several upgrades during the time; the most extensive one started in 1995 and led to the detector configuration whose operation, begun in 2001, was generally referred to as CDF II (see Figures 2.5 2.6).

CDF II detector, shown in a schematic view in Figure 2.6, was composed of several specialized subsystems arranged in concentric layers, each one aimed at per-

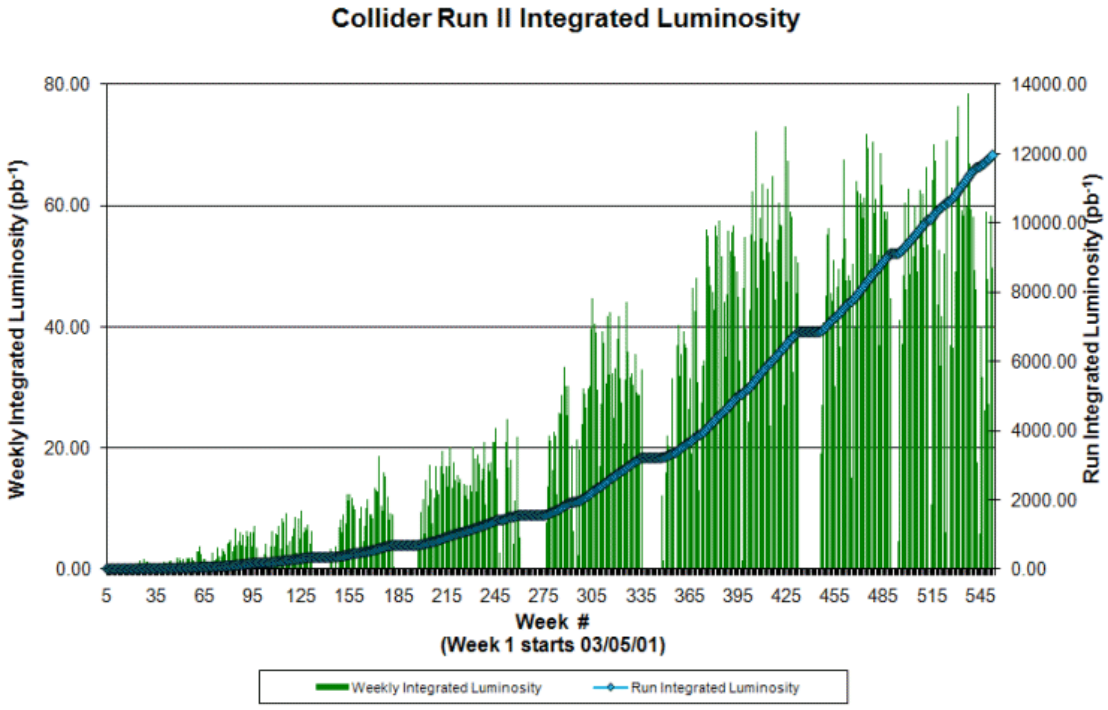

Figure 2.4: *Integrated luminosity as a function of the time (or store number). The blue line is for the acquired luminosity, while the black one for the delivered luminosity.*

forming a specific task. CDF II was a 5000-ton approximately cylindric assembly of sub-detectors, ~ 15 m in length, ~ 15 m in diameter. An accurate description of the final states particle in energetic hadronic collisions is quantitatively well obtained by the use of (pseudo)rapidity, transverse component of the momentum and azimuthal angle around the longitudinal axis (see Sec. sec. 2.2.1): this was the reason for the CDF II cylindrical symmetry both in the azimuthal plane and in the *forward* ($z > 0$) – *backward* ($z < 0$) directions with spatial segmentation of its subcomponents roughly uniform in pseudorapidity and azimuth.
Starting from the interaction point, particles generated from the $p\bar{p}$ collisions encountered in sequence:

- the thin beryllium wall of the beam vacuum pipe;
- a high-precision tracking system, that provided charged-particle trajectory reconstruction; it was composed by a inner set of silicon microstrip detectors and an outer drift chamber;
- a time of flight detector, for the particle identification. It was a cylindrical

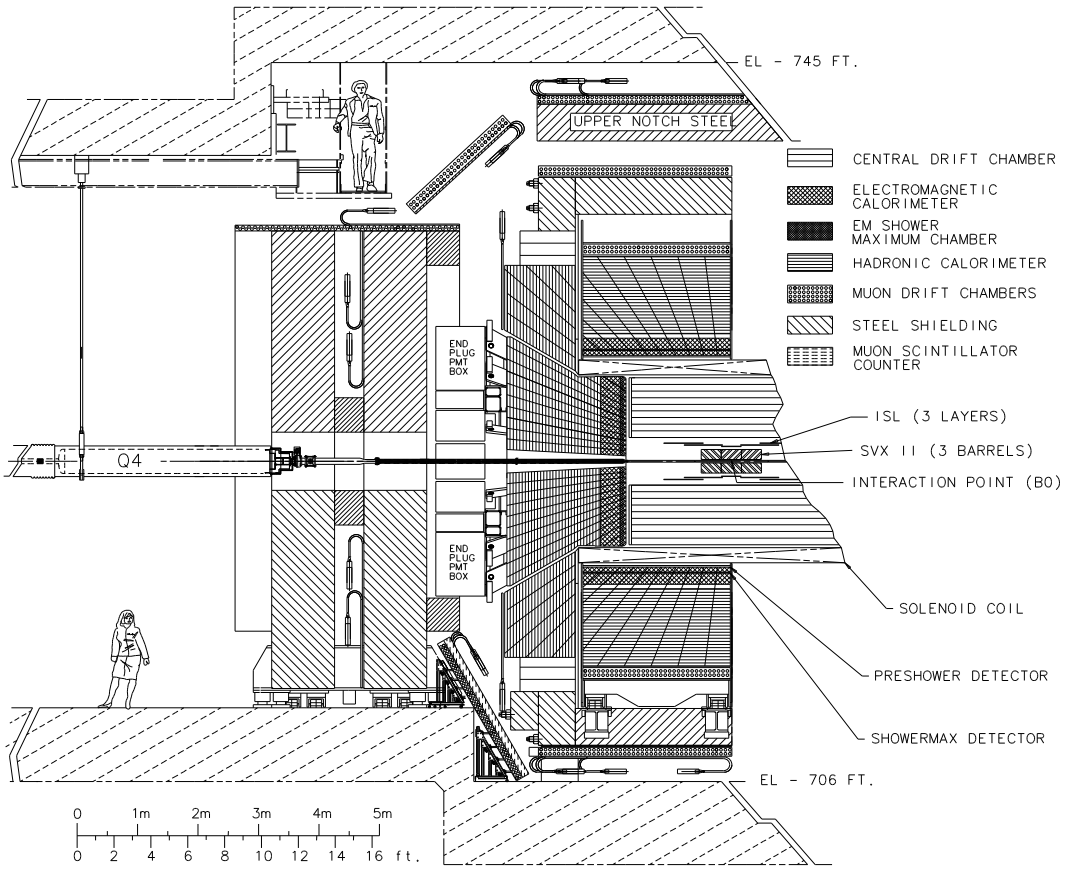

Figure 2.5: *View of one half of the CDF II detector in the longitudinal section.*

array made of scintillating bars that allowed particle identification via the time of flight method. The TOF was also contained into the solenoid;

- a solenoidal magnet and its return steel joke to avoid having the fields interfere with the proper operations of the following calorimeter's PMTs;

- a set of electromagnetic and hadronic calorimeters segmented with a projective tower geometry. They measured respectively the energy of photons and electrons and the energy of hadronic particles using the shower *sampling technique*. The basic structure consisted of alternating layers of passive absorber and plastic scintillator.

- a set of drift chambers and scintillators counters, used to detect muons.

The set of all these components guaranteed the possibility of CDF II to perform a wide range of measurements, including high resolution tracking of charged particle, electron and muon identification, low momentum π/K separation, precise secondary vertices proper time measurements, finely segmented sampling of energy

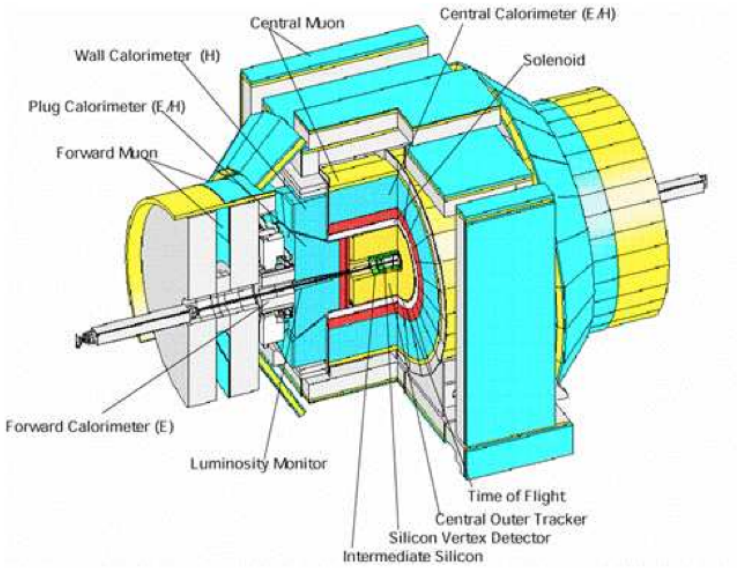

Figure 2.6: *Isometric view of the CDF Run II detector..*

flow coming from final state hadrons, electrons or photons, identification of neutrinos via transverse energy imbalance. Another fundamental feature of CDF II was the capability to monitor the instantaneous luminosity. This was achieved by the use of Cherenkov Luminosity Counters (CLC) (see Sec. 2.2.4).

A 1.4 T solenoidal magnetic field was maintained in the region with $r \leq 150$ cm and $|z| \leq 250$ cm by circulating a 4650 A current through 1164 turns of a Nb-Ti/Cu superconducting coil. The field was oriented along the positive $\hat{z}$ direction and was uniform at the 0.1% level in the $|z| \leq 150$ cm volume, where tracking measurements were made (the tiny non-uniformities, mapped out during the detector construction, were treated as a small perturbation within the track fitting software). The field was continuously monitored via NMR probes during data taking and any deviation from the mapped values was applied as a correction to measured track momenta. The threshold to escape radially the magnetic field for a particle was $p_T > 280$ MeV/c while the trajectory of a $p_T = 30$ GeV/c particle deviates only 1.6 cm from a straight path of 150 cm. The solenoid was 4.8 m in length, 1.5 m in radius, 0.85 X_0 (*radiation length* for normally incident particles) in radial thickness and was cooled by forced flow of two-phase helium.
The detector was divided conventionally into two main polar regions. In the following, if not otherwise stated, we refer to the detector volume contained in the $|\eta_{\rm det}| < 1$ as the *central region*, while the *forward region* indicates the detector volume comprised in $1 < |\eta_{\rm det}| < 3.6$.

2.2.1 Coordinates system

The Figure 2.7, shows the right-handed Cartesian coordinates system employed in CDF II. The origin of the frame was assumed to coincide with the BØ nominal inter-

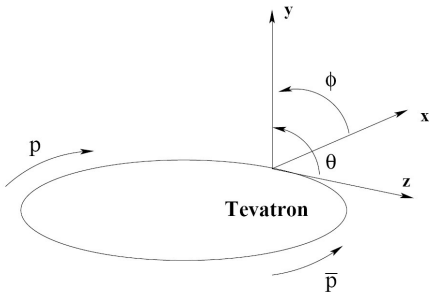

Figure 2.7: *CDF II Cartesian coordinates system.*

action point and with the center of the drift chamber. The proton direction (east) defined the positive z-axis which lay along the nominal beam line. The (x, y) plane was therefore perpendicular to both protons and antiprotons beams. The positive *y-axis* pointed vertically upward and the positive x-axis pointed radially outward with respect to the center of the ring, in the horizontal plane of the Tevatron. Neither the protons beam nor the antiprotons beam was polarized. As a consequence, the resulting physical observations are invariant under rotations around the z-axis. This invariance makes a description of the detector geometry in cylindrical (r, ϕ, z) coordinates system very convenient. Throughout this thesis, we use the word *longitudinal* to indicate the positive direction of the the z-axis and the word *transverse* to indicate the plane perpendicular to the proton direction, i.e. $(x, y) \equiv (r, \phi)$ plane.

In the hadron collisions environment, it is customary to use a variable invariant under $\hat{z}$ boosts as an unit of relativistic phase-space, instead of the polar angle θ. This variable is the *rapidity* defined as

$$y = \frac{1}{2} \ln\left[\frac{E + p \cdot \cos(\theta)}{E - p \cdot \cos(\theta)}\right] \tag{2.4}$$

where $(E, \vec{p})$ is the energy-momentum four-vector of the particle. Under a $\hat{z}$ boost to an inertial frame with velocity β, the rapidity of a particle transforms linearly, according to $y \to y' \equiv y + \tanh^{-1}(\beta)$, therefore y is invariant since $dy \equiv dy'$. However, a measurement of rapidity still requires a detector with accurate identification capabilities because of the mass term entering E. Thus, for practical reasons, it is often preferred to substitute y with its approximate expression η in the ultra-relativistic limit $(p \gg m)$, usually valid for products of high-energy collisions:

$$y \xrightarrow{p \gg m} \eta + \mathcal{O}(m^2/p^2) \tag{2.5}$$

where the *pseudo-rapidity* is only function of θ:

$$\eta = -\ln \tan\left(\frac{\theta}{2}\right) \tag{2.6}$$

As the event-by-event longitudinal position of the actual interaction is distributed around the nominal interaction point with ~ 30 cm r.m.s width, it is useful to distinguish the *detector pseudo-rapidity*, η_{det}, measured with respect to the (0,0,0) nominal interaction point, from the *particle pseudo-rapidity*, η, measured with respect to the z_0 position of the real vertex where the particle originated. For instance, for a particle produced at $z = 60$ cm from the nominal interaction point, it is $\eta_{\text{det}} \approx \eta \pm 0.2$.

An other commonly used variable is the transverse component of the momentum with respect to the beam axis (p_T), defined as:

$$\vec{p}_T \equiv (p_x, p_y) \rightarrow p_T \equiv p \cdot \sin(\theta). \tag{2.7}$$

2.2.2 Tracking system

An integrated cylindrical system consisting of three silicon inner subdetector (LØØ, SVX II and ISL) and an outer drift chamber (COT), immersed in a B = 1.4 T solenoidal magnetic field parallel to the beam axis, provided an excellent three-dimensional charged particle tracking. A diagram of the CDF tracking volume in the (r, z) plane is shown in Figure 2.8. Here we describe in more details each tracking subsystem, starting from the one closer to the interaction point.

2.2.2.1 LayerØØ

LayerØØ (LØØ) was the innermost layer of the microvertex silicon detector (see Figure 2.9). It was a single sided silicon microstrip detector directly mounted on the 80 cm long beryllium beam pipe, at an alternating radius of 1.35 cm or 1.62 cm. The state-of-the-art 7.85 cm long silicon sensors of LØØ could be biased to very high voltages ($\mathcal{O}$(500 V)) allowing to maintain a good signal-to-noise ratio even after high integrated radiation dose ($\mathcal{O}$(5 MRad)). The radiation hardness of such sensors allowed their installation at radii of 1.35 and 1.62 cm supported by a mechanical structure in direct contact with the beam pipe. The LØØ strips were located parallel to the beam axis and provided the first sampling of tracks in the $r - \phi$ plane; the inter-strip pitch was 25 μm but the read-out strip were alternated with floating ones resulting in 50 μm of readout pitch and a resolution of the $r - \phi$ charged particle's impact point of about 10 μm.
The operation temperature of this device was around 0° C maintained by a forced flux of under-pressurized gas through tiny aluminum pipes installed in between the sensor and the beam-pipe.

The total mass of the LØØ was about $0.01 \cdot X_0$ in the region with the cooling pipes, while it reduced to $0.006 \cdot X_0$ in the regions where only sensors were placed.

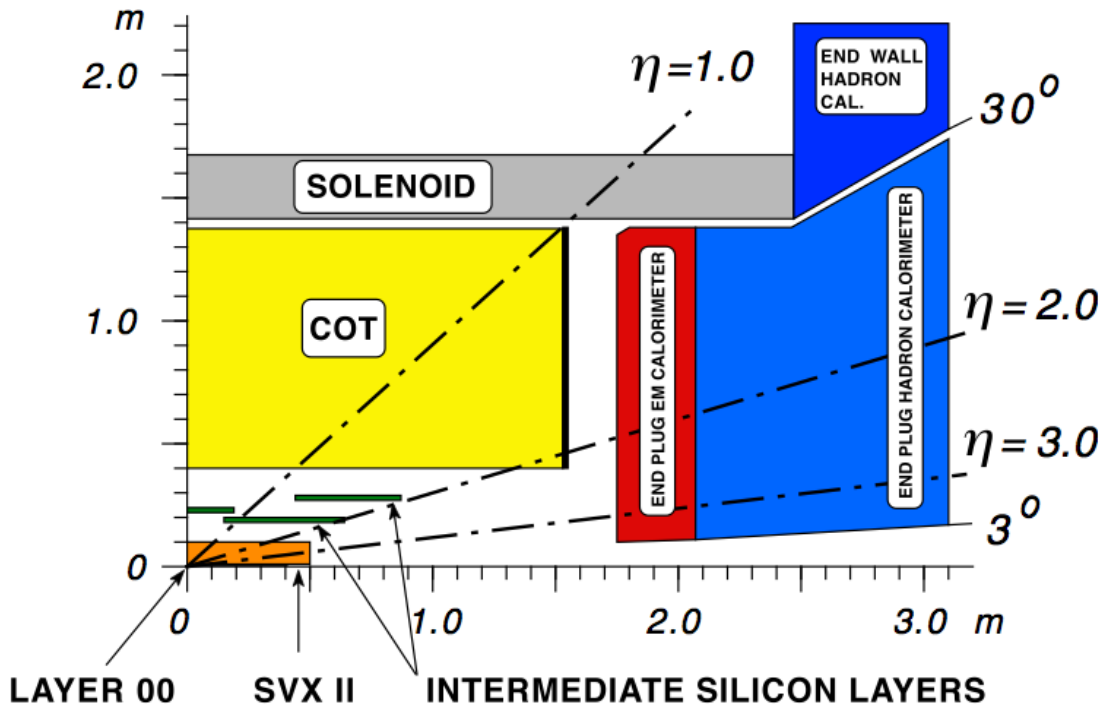

Figure 2.8: *Elevation view of one quadrant of the inner portion of the CDF detector; the tracking volume inside the solenoid and the forward calorimeters are shown.*

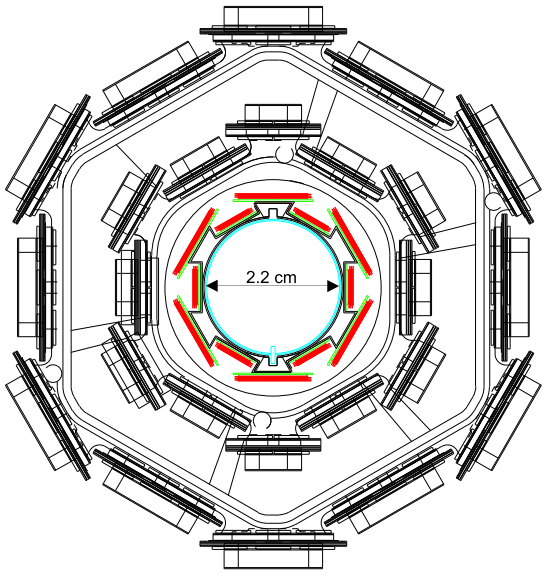

Figure 2.9: *Schematic illustration of LØØ and the first two layers of SVXII.*

2.2.2.2 Silicon VerteX detector II

Located outside LØØ, the Silicon VerteX detector II (SVX II) consisted of a fine resolution silicon microstrip vertex detector which provided five 3D samplings of a track in the transversal region between 2.4 and 10.7 cm from the beam (see Figure 2.8). The detector cylindrical geometry coaxial with the beam was segmented along z into three 32 cm long *mechanical barrels* for a total length of 96 cm which assured a complete geometrical coverage within $|\eta_{\text{det}}| < 2$ (see Figure 2.10(a)). Each barrel comprised 12 azimuthal wedges each of which subtended approximately 30°. In order to allow the wedge-to-wedge alignment, the edges of two adjacent wedges slightly overlapped [4]. Each wedge consisted of 5 concentric and equally spaced silicon layers sensors installed at radii 2.45 (3.0), 4.1 (4.6), 6.5 (7.0), 8.2 (8.7) and 10.1 (10.6) cm from the beam[5] as shown in Figure 2.10(b).

Independent readout units, called *ladders*, hosted sensors in a layer. Each ladder was composed by two double sided rectangular 7.5 cm long sensors and by the read out electronics unit. SVX II active surface consists of double-sided, AC-coupled silicon sensors. In each sensors side, the different possible orientations of strips were three:

1. *Axial*, strips oriented parallel to the beam axis, called $r - \phi$;

2. *Small Angle Stereo* (SAS), strips rotated by 1.2° with respect to the beam axis;

3. *90° Stereo*, strips oriented in the transverse plane.

All the five layers had axial strips on one side, three had 90° stereo on the other side and two had SAS strips.

A radiation-hard front-end chip, called SVX3D, collected the charge pulse from the strips. Only signals above a threshold were processed: SVX3D operated readout in "sparse-mode". When a channel was over the threshold, the signal of the neighbor channels was also processed in order to cluster the hits. The measured average signal-to-noise ratio was S/N $\geq$ 10 with a single hit efficiency greater than 99%.
Impact parameter resolution for central high momentum tracks were $\sigma_\phi < 35$ μm and $\sigma_z < 60$ μm. To prevent thermal expansion, relative detector motion, increased leakage current and chip failure due to thermal heating the SVX II was held at roughly constant temperature of 10-15° C through the operation of a water-glycol cooling system whose pipes ran all below the detector. The average material of SVX II corresponded to $0.05 \cdot X_0$.

[4] Half of the wedges were closer to the beam than the other half because their edges had to overlap.

[5] The numbers in brackets indicate the distance from the beam of the further wedges layers.

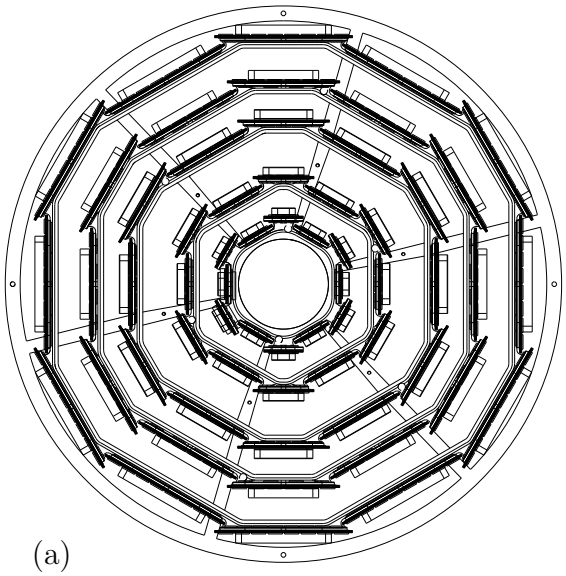

(a)

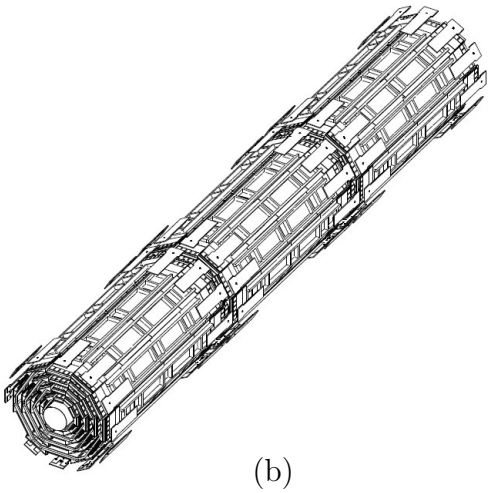

(b)

Figure 2.10: *(a) SVX II section view in the* (r, ϕ) *plane; (b) view of the three instrumental mechanical barrels of SVX II.*

2.2.2.3 Intermediate Silicon Layer

On the outside of SVX II, another silicon tracker was placed: the Intermediate Silicon Layer detector, ISL, shown in Figure 2.11. It was a silicon tracker placed at intermediate radial distance between the SVX II and the drift chamber (see Figure 2.8). The polar coverage extended to $|\eta_{\text{det}}| < 2$. ISL could be roughly divided in three regions: a central region and two forward regions. The central region consisted of a single layer of silicon installed over a cylindrical barrel at radius of 22 cm, while the forward regions consisted of two layers of silicon installed on concentric barrels at radii of 20 and 28 cm. In order to match SVX II wedges, each silicon layer of ISL

was azimuthally divided into 30°.The basic readout unit was the ISL *ladder* which was similar to the SVX II ladder but consisted of three, instead of two, sensors wirebonded in series resulting in a total active length of 25 cm.

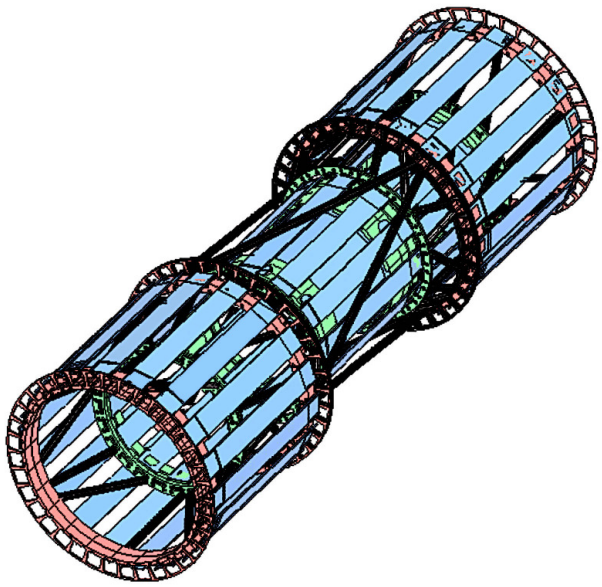

Figure 2.11: *Schematic illustration of the three mechanical barrels of ISL.*

ISL sensors were double sided AC-coupled, with axial strips on one side and SAS strips on the other. The sensors dimensions were 5.7×7.5 cm^2 wide and 300 μm thick. As in SVX II, the charge pulse from each strip was read by SVX3D chips. ISL average mass was $0.02 \cdot X_0$ for normally incident particles.

In Figure 2.12 the complete silicon detector system and its coverage in the $r-z$ plane is shown.

2.2.2.4 Central Outer Tracker

The outermost tracking volume of CDF II was a large open cell drift chamber called the Central Outer Tracker (COT), see Figure 2.14.
The COT was a cylindrical detector, coaxial with the beam and it extended radially, within the central region, between the radius of 40 cm and 138 cm from z-axis. The chamber contained 96 radial layers of wires arranged into 8 *superlayers* (SL), see Figure 2.14(a). Each SL sampled the path of a charged particle at 12 radii (spaced 0.762 cm apart) where sense wires were strung. The wires of the 8 SL were not oriented all in the same way: in order to reconstruct the path of a charged particle in the $r-z$ volume, the wires of four SL were oriented parallely to the beam axis (*axial* SL) and the wires of the remaining four SL were oriented either +3° or -3°

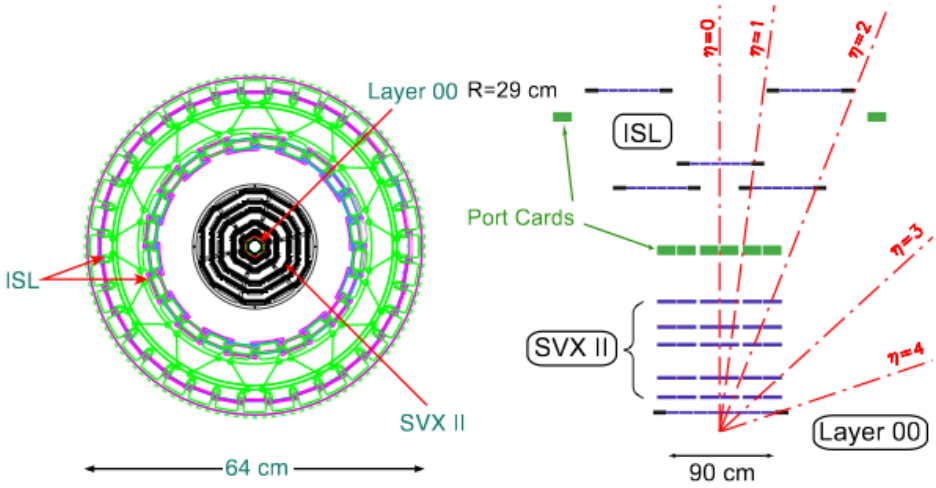

Figure 2.12: *A radial view of the three silicon detector subsystems (left) and their coverage in the $r-z$ plane (right).*

with respect to the beamline (*stereo* SL). The axial SL were radially interleaved with the stereo SL. Combined readout of stereo and axial SLs allowed the measurement of the $r-z$ hit coordinates.
Each superlayer was azimuthally segmented into open drift cells. A drift cell, as shown in Figure 2.14(b), contained a row of 12 sense wires alternating with thirteen 0.40 μm diameter gold-plated tungsten potential wires which controlled the gain on the sense wires, optimizing the electric field intensity. The cathode of the detection circuit was the *field panel* which closed the cell along the azimuthal direction. It was made of gold on a 0.25 mm thick Mylar sheet and defined the fiducial volume of a cell. The electric field strength was 2.5 kV/cm. Innermost and outermost radial extremities of a cell were both closed mechanically and electrostatically by the *shaper panels*, which were Mylar strips carrying field-shaping wires attached. The architecture of the cell allowed the containment of a possible broken wire inside only one cell.

In the chamber, the crossed electrical and magnetic field as well as the characteristics of the gas mixture caused an angular shift of the particle drift path. In order to balance this shift, the wire planes were 35° azimuthal tilted with respect the radial direction. The tilted-cell geometry showed other benefits: the calibration of the drift-velocity was easier and the left-right ambiguity[6] for tracks coming from the origin was removed. An overview of the COT main characteristics is presented

[6]Each pulse on a given wire had a two fold ambiguity corresponding to the two incoming azimuthal drift trajectories. The signals from a group of nearby radially wires satisfied the configuration for two tracks, one from the actual particle trajectory and another "ghost track" originated by the two fold ambiguity.

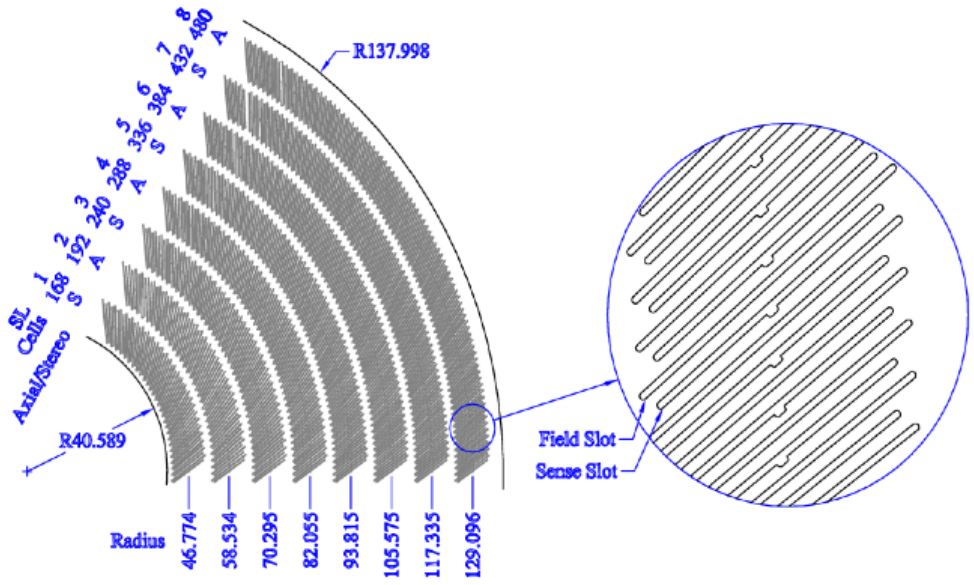

(a)

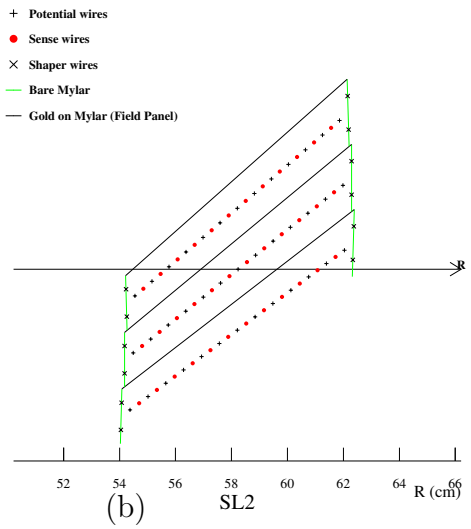

(b)

Figure 2.13: *A 1/6 section of the COT end-plate. (a) For each super-layer is given the total number of cells, the wire orientation (axial or stereo) and the average radius [cm]. The enlargement shows in details the slot were wire planes (sense) and field sheet (field) were installed. (b) A sketch of an axial section of three cells in super-layer 2. The arrow shows the radial direction.*

in Table 2.14.

A preamplifier shaped and amplified the analog pulses from the COT sense wires. To perform the dE/dx measurements, the discriminated differential output was used

Gas Mixture	Ar(50%)/Ethane(35%)/CF_4(15%)
Electron drift speed	about 100 μm/ns
Maximum drift time	about 100 ns
Track efficiency	99%
Single hit resolution	$\sigma_{\text{hit}} \simeq 140$ μm
p_t resolution	$\sigma_{p_T}/p_T^2 \simeq 0.0015$ c/GeV
Mass	$0.016 \cdot X_0$ for normally incident particle

Figure 2.14: *COT characteristics.*

because it encoded charge information in its width. A TDC was used to record the leading and trailing edges of the signals in 1 ns bins.
The COT had a 99% efficiency on tracks with measured single hit resolution $\sigma_{\text{hit}} \simeq 175$ μm and p_t resolution was $\sigma_{p_T}/p_T^2 \simeq 0.13\%$ c/GeV. The material of the COT was about $0.016 \cdot X_0$ for tracks at normal incidence.

2.2.2.5 Tracking performance.

The only physical objects used in this analysis are the *tracks*. An integrated cylindrical system consisting of three silicon inner subdetector and an outer drift chamber, immersed in a B = 1.4 T solenoidal magnetic field parallel to the beam axis, provided three-dimensional charged particle tracking. Within the magnetic field, particle trajectories were described by an helix, whose arc could be parameterized by using three transverse and two longitudinal parameters:

C – signed helix (half-)curvature, defined as $C \equiv \frac{q}{2R}$, where R was the radius of the helix. This was directly related to the transverse momentum: $p_T = \frac{cB}{2|C|}$ (where B was the intensity of the magnetic field).

φ_0 – ϕ direction of the particle at the point of closest approach to the beam.

d_0 – signed impact parameter, i.e. the distance of closest approach to the z-axis, defined as $d_0 \equiv q \cdot (\sqrt{x_c^2 + y_c^2} - R)$, where (x_c, y_c) were the coordinates of the beam in the transverse plane. This is schematically drawn in Figure 2.15.

λ – the helix pitch, i.e. $\cot(\theta)$, where θ was the polar direction of the particle at the point of its closest approach to the beam. This was directly related to the longitudinal component of the momentum: $p_z = p_T \cdot \cot(\theta)$.

z_0 – the z coordinate of the point of closest approach to the beam.

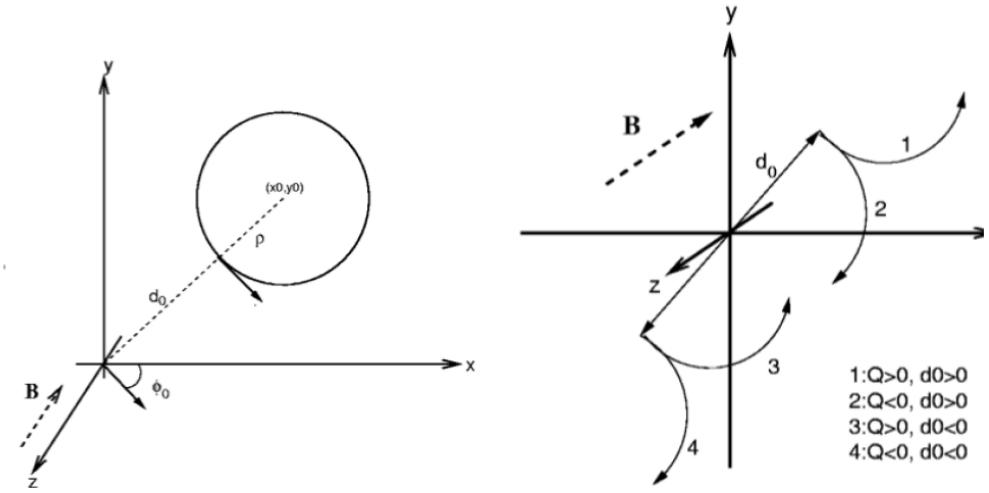

Figure 2.15: *Schematic drawing of the impact parameter d_0 and of the convention about the signs.*

The trajectory of a charged particle satisfied the following equations:

$$x = r \cdot \sin(\varphi) - (r + d_0) \cdot \sin(\varphi_0) \tag{2.8}$$

$$y = -r \cdot \cos(\varphi) + (r + d_0) \cdot \cos(\varphi_0) \tag{2.9}$$

$$z = z_0 + s \cdot \lambda \tag{2.10}$$

where s was the projected length along the track, $r = 1/2C$ and $\varphi = 2Cs + \varphi_0$. When a charged particle passed through the tracking system, the detector reconstructed, along the physical trajectory of the particle, a set of spatial measurements (hits) by clustering and pattern-recognition algorithms. In order to reconstruct the trajectory, the hits were fitted with a helical fit, which determined the five above parameters and finally defined a track object. The helical fit took into account non-uniformities of the magnetic field and scattering in the detector material.

For this analysis only tracks reconstructed with both silicon and COT hits have been used (*SVX+COT* tracks) because of three main reasons:

- silicon stand-alone tracking (*SVX-Only* tracks) becomes important in the region $1 \leq |\eta| \leq 2$ where the COT coverage was incomplete (this region of acceptance is excluded in our analysis, since the reconstruction efficiency and the momentum resolution out of this region are too low);

- in the central region only track with a $p_T < 0.28$ GeV/c have SVX-Only informations and this value is well below our minimum request;

- COT stand-alone tracking (*COT-Only* tracks) has an insufficient impact parameter resolution for our needs;

All SVX+COT tracks were first fit as COT only and then extrapolated inward to the silicon and refitted with the additional points. In the COT the track density was lower than in the silicon, because of its greater radial dimension, consequently the probability of hits accidental combination in the track reconstruction was smaller. This way of performing the fit was fast and efficient; the resulting tracks had high purities.

COT performance. The COT efficiency for tracks was typically 99% and all the COT channels worked properly until the last Tevatron run. Cosmic rays were exploited to mantain the internal alignments of the COT cells within 10 μm. The wires mechanical curvatures effects due to gravitational and electrostatic forces were kept under control within 0.5% by equalizing the difference of E/p between electrons and positrons as a function of $cot(\theta)$. The single-hit resolution was about 140 μm, including a 75 μm contribution from the uncertainty on the measurement of the proton-anitproton interaction time. The typical resolutions on track parameters for tracks fit with no silicon information or beam constraint were: $\sigma_{p_T}/p_T^2 \approx 0.0015$ c/GeV, $\sigma_{\varphi_0} \approx 0.035°$, $\sigma_{d_0} \approx 250$ μm, $\sigma_\theta \approx 0.17°$ and $\sigma_{z_0} \approx 0.3$ cm.

Performance with the silicon detectors. The reconstruction of the hits in the silicon detector was fundamental to improve the impact parameter resolution of tracks. In fact, with the additional informations provided by the silicon, the resolution could reach $\sigma_{d_0} \approx 20$ μm (not including the transverse beam size). This value, combined with the $\sigma_{\mathrm{T}} \approx 30$ μm transverse beam size, is sufficiently small with respect to the typical transverse decay-lengths of heavy flavors hadrons (a few hundred microns) to allow separation of their decay vertices from production vertices. The silicon tracker improved also the stereo resolutions up to $\sigma_\theta \approx 0.06°$, and $\sigma_{z_0} \approx 70$ μm. While, the transverse momentum and the azimuthal resolutions remained approximately the same of COT-Only tracks.

2.2.3 Other CDF II subdetectors

For accurate details on the CDF II subdetectors not used in this analysis (TOF system, calorimeters and muon system) see [25].

2.2.4 Cherenkov Luminosity Counters and measurement of the luminosity

Absolute luminosity measurements by the machine based on measurements of beam had uncertainties of the order of 15-20%.

For this reason in CDF, the beam luminosity was determined using gas Cherenkov counters (CLC) located into the pseudorapidity region $3.7 < |\eta| < 4.7$, which measured the average number of inelastic interaction per bunch crossing. Each module

consisted of 48 thin, gas-filled, Cherenkov counters. The counters were arranged around the beam pipe in three concentric layers, with 16 counters each, and pointing to the center of the interaction region. The cones in the two outer layers were about 180 cm long and the inner layer counters, closer to the beam pipe, had a length of 110 cm (see Figure 2.16). The Cherenkov light was detected with photomultiplier tubes and the momentum threshold for light emission was 9.3 MeV/c for electrons and 2.6 GeV/c for pions. The number of $p\bar{p}$ interactions in a bunch crossing followed a Poisson distribution with mean μ, where the probability of empty crossing was given by:

$$P_0(\mu) = e^{-\mu} \tag{2.11}$$

This formula is correct if the acceptance of the detector and its efficiency were 100%. In practice, there were some selection criteria, α, to define an interaction. An interaction was defined as a $p\bar{p}$ crossing with hits above a fixed threshold on both sides of the CLC detector. Therefore, an empty crossing was a $p\bar{p}$ crossing with no interactions. Given these selection criteria, the experimental quantity P_0, called $P_0^{exp}(\alpha)$, is related to μ as:

$$P_0^{exp}(\mu;\alpha) = \left(e^{\epsilon_\omega \cdot \mu} + e^{-\epsilon_e \cdot \mu} - 1\right) \cdot e^{-(1-\epsilon_0)\cdot\mu} \tag{2.12}$$

where the acceptances ϵ_0 and $\epsilon_{\omega/e}$ were, respectively, the probability to have no hits in the combined east and west CLC modules and the probability to have at least one hit exclusively in west/east CLC module. The evaluation of these parameters was based on Monte Carlo simulations, and typical values were: $\epsilon_0 = 0.07$ and $\epsilon_{\omega/e} = 0.12$. From the measurement of μ we can extract the luminosity. Since the CLC was not sensitive at all to the elastic component of the $p\bar{p}$ scattering, the rate of inelastic $p\bar{p}$ interactions is given by:

$$\mu \cdot f_{\text{b.c.}} = \sigma_{\text{p}\bar{\text{p}}\text{-in.}} \cdot \mathcal{L} \tag{2.13}$$

where the bunch-crossing frequency ($f_{\text{b.c.}}$) is known from the Tevatron RF, $\sigma_{\text{p}\bar{\text{p}}\text{-in.}} = 59.3 \pm 2.3$ mb is the inelastic $p\bar{p}$ cross-section resulting from the averaged CDF and E811 luminosity-independent measurements at $\sqrt{s} = 1.8$ TeV [26] [27] and extrapolated to $\sqrt{s} = 1.96$ TeV .

2.2.5 Trigger and Data AcQuisition (DAQ) system

The average interaction rate at the Tevatron was 1.7 MHz for $36 \cdot 36$ bunches. In fact, the interaction rate was higher because the bunches circulated in three trains of 12 bunches in each group spaced 396 ns, which led to a crossing rate of 2.53 MHz. The interaction rate was orders of magnitude higher than the maximum rate that the mass storage system could handle (f ~ 100 Hz). This led to the implementation of a trigger system that preselected events online and decided if the corresponding event information was written to tape or discarded. The CDF trigger system consisted of

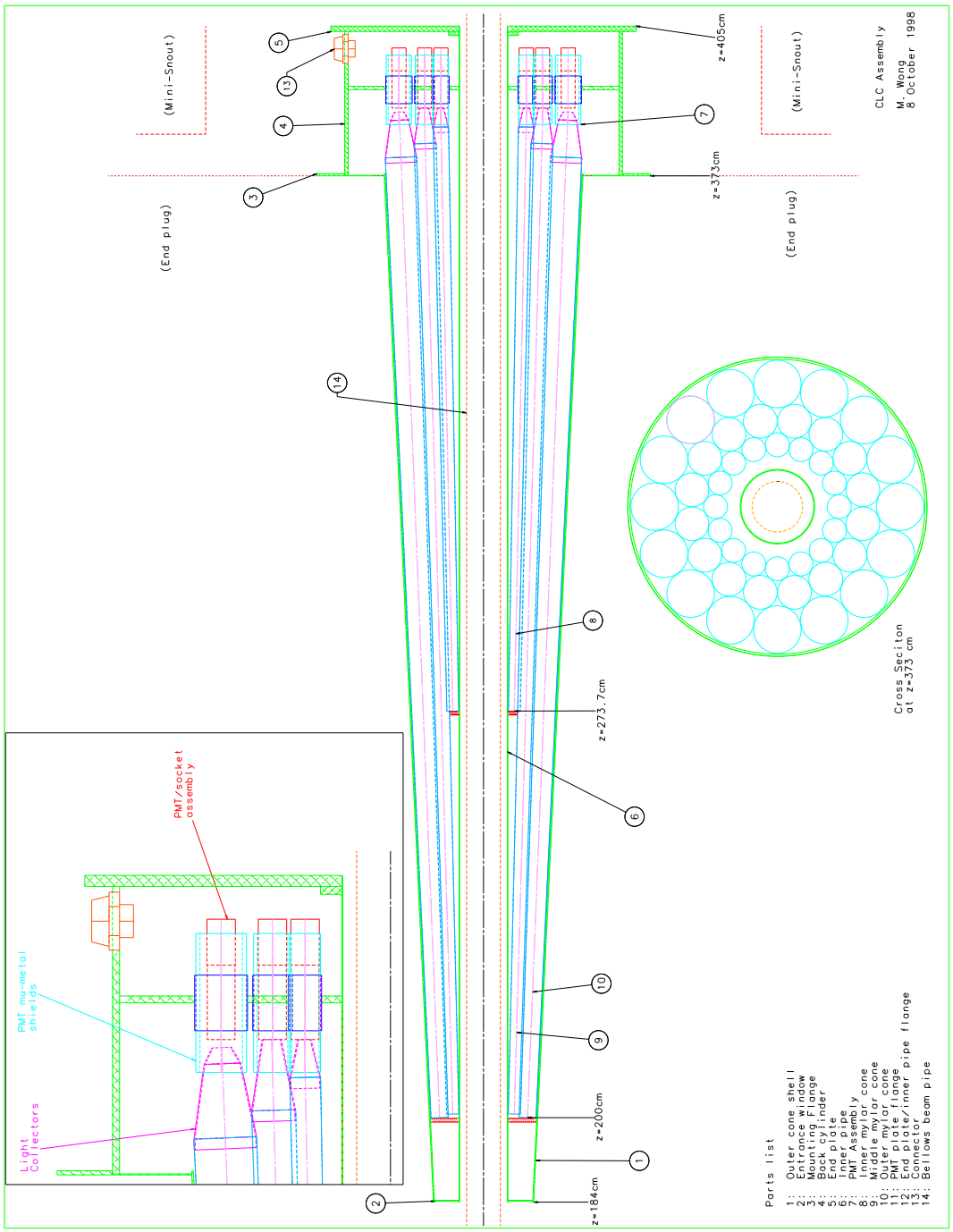

Figure 2.16: *Longitudinal section of the CLC system.*

three trigger levels, see Figure 2.17. The first two levels were hardware based and the third one was processed by a farm of computers. The decisions taken by the system are based on increasingly more complex event information. Each level received the

data event accepted by the previous one and, provided with more accurate detector information and more time for processing, chose to discard it or to send it to the following level. Level-1 and Level-2 received data directly from the detector front end electronics; events passing the Level-3 were stored to permanent memory.

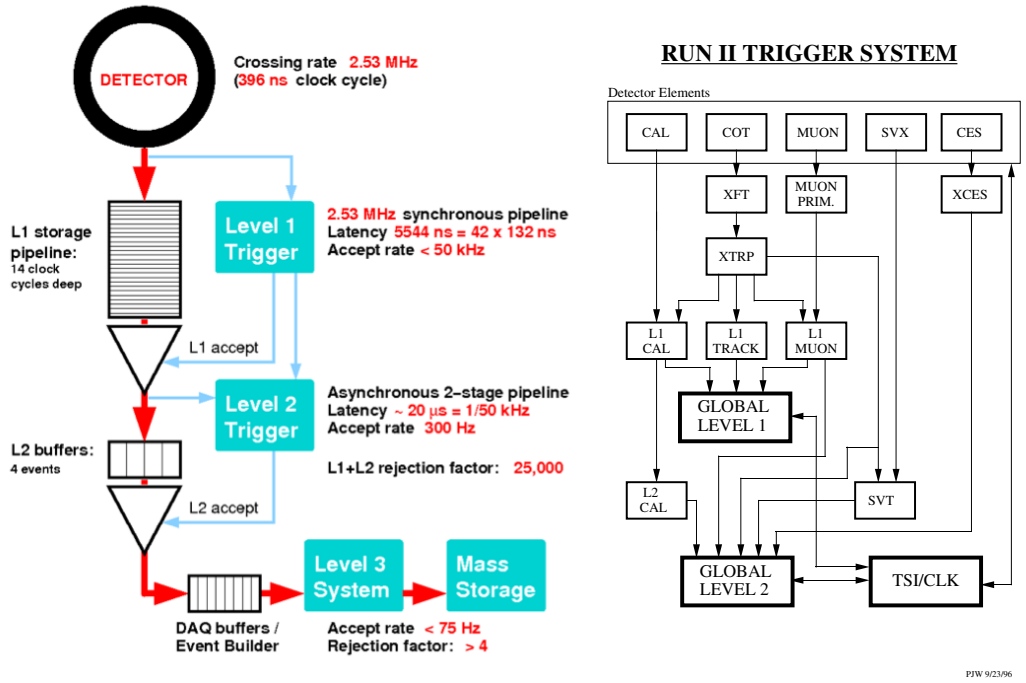

Figure 2.17: *Functional block diagram of the CDF II trigger and data acquisition system.*

Since the read-out of the entire detector needed about 2 ms on average, without a triggering system, after the acquisition of one event, other ~ 5,000 interactions could occur and they remained unrecorded. The percentage of events rejected solely because the trigger was busy processing previous events was referred to as trigger *deadtime* and at the final luminosity its tipical value was around the 5%.

2.2.5.1 Level 1

The Level 1 (L1) trigger was a synchronous system with an event read and a decision made every beam crossing. The depth of the L1 decision pipeline was approximately 4 μs (L1 latency). The L1 buffer had to be at least as deep as the total processing pipeline or the data associated with a particular L1 decision could have been lost before the decision was made. The L1 buffer was 14 crossings deep (5544 ns for a 396 ns bunch spacing) to provide a margin for unanticipated increases in L1 latency. The Level 1 reduced the event rates from 2.53 MHz to about 18 KHz.

At L1, a synchronous system of custom-designed hardware processes a simplified subset of data in three parallel streams to reconstruct coarse informations from the calorimeters (total energy and presence of single towers over threshold), the COT (two-dimensional tracks in the transverse plane) and the muon system (muon stubs in the CMU, CMX, and CMP chambers). A decision stage combined the information from these low-resolution physical objects, called "primitives", into more sophisticated objects (e.g., track primitives are matched with muon stubs or tower primitives) to form muon, electron or jet, which were subjected to basic selections. The COT channels were processed by the eXtremely Fast Tracker (XFT). The XFT was a custom processor that identified two-dimensional tracks in the (r, ϕ) view of the COT (transverse plane) in time with the L1 decision. It used a pattern matching algorithm to first identify short segments of tracks and then to link them into full-length tracks. If a coincidence between segments crossing four super-layers was found, two-dimensional XFT-tracks were reconstructed by linking the segments. Segments were compared to a set of about 2,400 predetermined patterns corresponding to all tracks with $p_T \gtrsim 1.5$ GeV/c originating from the beam line. The track-finding efficiency and the fake-rate with respect to the off-line tracks depended on the instantaneous luminosity and were measured to be $\varepsilon \approx 96\%$ and 3%, respectively, for tracks with $p_T \gtrsim 1.5$ GeV/c at $\mathcal{L} \approx 10^{32}$ [$\mathrm{cm}^{-2}\mathrm{s}^{-1}$]. The observed momentum resolution was $\sigma_{p_T}/p_T^2 \approx 0.017$ c/GeV and the azimuthal resolution was $\sigma_{\varphi_6} \approx 0.3^\circ$ (where φ_6 was the azimuthal angle of the track measured at the sixth COT super-layer, located at 106 cm of radius from the beam line).

2.2.5.2 Level 2 and Level 3

The Level-2 (L2) trigger fulfilled two subsequent tasks, the *Event building* and the *Decision*. L2 detector information was more complex than L1 detector information; thus, the Event builder (EVB) reconstructed the event with L2 information. The EVB processed in parallel the calorimetric and the tracking informations. It combined the outputs from L1 and L2 in order to decide whether or not an event was sent to Level-3. The maximum decision time of L2 was 20 μs for each event and the output rate was about 300 Hz.

Level-3 (L3) was exclusively software-based. About 400 commercial processors running in parallel reconstructed the event provided by L2 at full detector resolution. L3 codes were very similar to the offline reconstruction codes. About 191 *trigger paths* (a trigger path defined a particular sequence of L1, L2 and L3 selections) were implemented at L3; moreover L3 distributed the information to on-line monitoring consumers and data logger programs. The L3 decision to write on tape happened after the full reconstruction of the event was completed and the integrity of its data was checked in less than 10 ms. The typical size for an event was 150 kbytes and the maximum storage rate was about 20 Mbyte/s. The event output rate was finally ~

75 Hz: the relative fractions of high level objects was about 40% for the tracking, 30% for jet and photon and 30% for lepton.

2.2.6 Online operations and data quality

During each run, the operation of the detector and the quality of the *on-line* data taking was continuously controlled. The main causes of data taking inefficiencies were two. At the beginning of a run, the detector was not completely operative until the beam conditions were proved to be stable. In addition to that, problems related to trigger dead time, detector inactivity or DAQ malfunctioning could occur. The average data-taking efficiency was about 85%. The running condition had to undergo some physics-quality standards; for these reasons, the fractions of data valid for physics analysis were certified for each run by the crew in the CDF control room. The data-taking was immediately stopped if a malfunction of the detector was registered. Then, corrupted data were more likely contained in very short runs that were usually excluded on-line from physics analysis. The CLC were operative during the whole data-taking, thus an accurate integrated luminosity measurement had been guaranteed; a set of accelerator and detector parameters were constantly controlled to be within the expected ranges during the data taking. On-line, shift operators ensured that L1, L2 and L3 triggers worked correctly. Each time that at least one of the trigger paths fired, an "event" was labeled with a progressive number. Events were grouped into runs, i.e. periods of continuous data-taking in constant configurations of trigger table and set of active subdetectors. Several parameters of the operations (e.g. beam-line position and slope, set of calibrations, ...) were stored in the database on a run-averaged format.

2.2.7 Offline event reconstruction and analysis framework

All data manipulations occurring some time after the data were written to permanent memories and were referred to as *off-line* processes, as opposed to the on-line operations which took place in real time, during the data-taking. The events collected by the DAQ and the simulated samples were stored on tapes and analyzed with the *Production* reconstruction program. The production process was the main off-line operation: high-level software objects (e.g. tracks, vertices, muons, electrons, jets, etc.) were reconstructed by a centralized analysis computers farm from low-level information (e.g hits in the tracking subdetectors, muon stubs, fired calorimeter towers, etc.). Precise information about the detector such as calibrations, beam-line positions, alignment constants, masks of malfunctioning detector-channels, etc... and sophisticated algorithms were available during the production. After the production, the size of an event typically increased by the 20% because of the added information. Data produced this way are today directly accessible by all CDF analysis groups; usually each group creates a set of collection of these data (ntupes)

in order to have a secondary (reduced in size) set of data that physicists may use. These ntuples are created within the ROOT framework [28] (written in C++ and commonly used by several HEP experiments) and this same environment is also used for all the analyses preformed at CDF.

The ntuples used in this work are called Standard Ntuples (Stntuples) and they are commonly used by the QCD group. Stntuples contain the events collected by the triggers suitable for this analysis.

Chapter 3

Data selection

*In this chapter we describe how we extract the **signal**, $D^+ \to K^-\pi^+\pi^+$ (and its charge conjugated decay, $D^- \to K^+\pi^-\pi^-$), from all the other events, referred to as **background**. We show the decay kinematics highlighting the best variables to describe it. We illustrate the online trigger selection and the offline strategy to minimize the statistical uncertainties on the final result. We also present the studies developed on the selection requirements.*

3.1 $D^+ \to K^-\pi^+\pi^+$ at CDF II

D^+ decaying into three charged particles[1] represents one of the simplest decay channel detectable at CDF II for this meson, because of its sizeable branching fraction (~ 9.4 %) and mainly because all the decay products are charged particles. In addition there is no ambiguity in the assignment of the masses to the tracks: we know that the two tracks with the same charge are pions. These properties give us a good chance to unfold the heavy D^+ meson from the background of light particles (mainly pions and kaons) several orders of magnitude larger.

The large average lifetime of the D^+, $\tau = (1040 \pm 7) \cdot 10^{-15}$ s, corresponds to an average travelled path, away from the $p\overline{p}$ collision that originates it, of $c\tau = 311.8$ μm, that can be measured thanks to the resolution of the silicon tracker SVX II (see Sec. 2.2.2.5). In Figure 3.1 is sketched out the topology of the D^+ decaying to $K^-\pi^+\pi^+$ stressing out the relevant variables used in this analysis (for details about the quantities we use, see Sec. 2.2.2.5):

- the **transverse plane** is the plane perpendicular to the proton beam direction ($0xy$);

[1] From now, we write in term of D^+, but all the considerations are also true for the D^-.

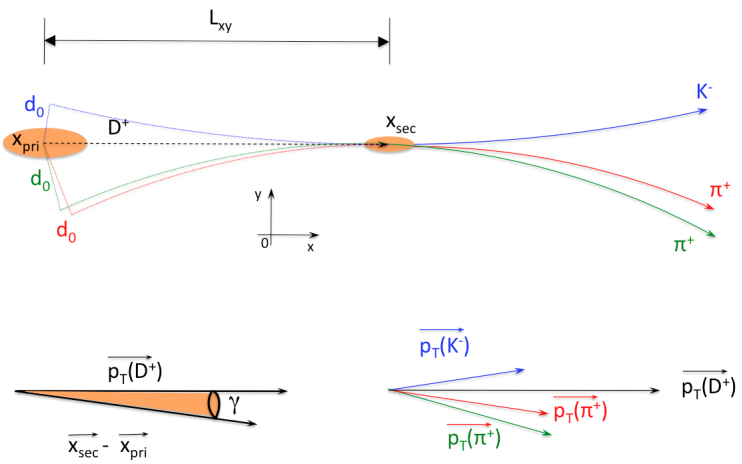

Figure 3.1: *Graphical representation in the plane of the decay channel* $D^+ \to K^-\pi^+\pi^+$.

- $\vec{x}_{pri}$ - the **primary vertex** - is the point where the $p\bar{p}$ collision takes place. It is located within the beam pipe and it represents the point where the meson is produced: D^+ **origin vertex**;

- $\vec{x}_{sec}$ - the **secondary vertex** - is the decaying point of the D^+;

- $\vec{p}_T$ - the **transverse momentum of the particle** - is the projection of the momentum vector to the transverse plane (writing p_T we refer to its magnitude);

- L_{xy} - the **transverse decay lenght** - is the signed distance between the primary and the secondary vertices projected to the $\vec{p}_T$ direction. It is defined as follows:

$$L_{xy} = \frac{(\vec{x}_{sec} - \vec{x}_{pri}) \cdot \vec{p}_T}{p_T}; \tag{3.1}$$

- d_0 - the **impact parameter** - is the signed distance between the origin vertex and the helix of a track at their closest approach;

- Δz_0 - the **longitudinal distance** - is the difference between the z coordinate (not shown in Figure 3.1) of the tracks at their maximum approach to the beam;

- $\Delta\varphi_0$ - the **transverse opening angle** - is the difference between the φ_0 angle (not shown in Figure 3.1) of the decay tracks at their maximum approach to the beam;

- γ - the **pointing angle** - is the angle in the transverse plane between the D^+ momentum and its travel direction:

$$\gamma = arccos\left[\frac{(\vec{x}_{sec} - \vec{x}_{pri})}{|\vec{x}_{sec} - \vec{x}_{pri}|} \cdot \frac{\vec{p}_T}{p_T}\right]; \tag{3.2}$$

3.2 Online

The published CDF measurement of the D^+ production cross section [20] extends to the minimum $p_T(D^+)$ of 6.0 GeV/c because the data set is selected by a trigger selection with hard requests in terms of transverse momentum of the meson decay products. In our case, in order to reach $p_T(D^+)$ values down to 1.5 GeV/c, we remove any possible bias from the trigger selection. We use the samples collected by the `ZEROBIAS` and the `MINBIAS` trigger paths because they completely satisfy our request. The samples have been collected during the whole Run II of the experiment (about 10 years of data taking, from February 2002 to September 2011) and they correspond to a total Tevatron delivered luminosity $L_{\text{dev}} = 10/\text{fb}$.

3.2.1 The Zero Bias trigger

The first trigger used in this analysis is the `ZEROBIAS (ZB)`. It doesn't use subdetectors: it depends only on the Tevatron bunch crossing frequency independently of whether the crossing produced a $p\bar{p}$ scattering or not. In order not to overcome the maximum output rate to the disk, the event rate must be reduced by a prescale factor; this happens only at L1. The ZB requirements to trigger an event are the followings:

Level 1: any bunch crossing fires L1. Prescale factor = 1,000,003.

Level 2: no restrictions, any event is automatically accepted by L2.

Level 3: no requests.

About 177 millions of events are collected by this trigger.

3.2.2 The Minimum Bias trigger

The second trigger used for this analysis is the `MINBIAS (MB)`. The aim of this trigger is to identify and select only crossings resulting in, at least, an inelastic $p\bar{p}$ collision. The main restrictions apply at L1 exploiting the CLC subdetectors. L1 fires when at least one East CLC signal is in coincidence with a signal in at least one West CLC. Considering the tipical Tevatron initial luminosity, almost all the bunch crossings result in a hard collision. As a consequence, the MB output rate would be higher than the maximum output rate to disk. A prescale factor is applied: one

event is triggered by L1 every 100,003 times this coincidence occurs. For the same reason further rate limitations occur at L2 and L3 reducing the trigger rate to one event per second. The MB requirements to trigger an event are the followings:

Level 1: CLC signals coincidence. Prescale factor = 100,003.

Level 2: any event is automatically accepted by L2. Rate limit = 3 Hz.

Level 3: any event is automatically accepted by L3. Rate limit = 1 Hz.

About 123 millions of events are collected by this path.

3.2.3 Samples overlap

During the data acquisition, the ZB and MB trigger selections operate at the same time. Events might be collected by both triggers and appear twice in the sample. All the times a collision happens and the crossing is triggered by the CLCs coincidence, also the ZB trigger is fired. On the contrary, bunch crossings with no interaction won't be triggered by the CLC coincidence. Thus the `MINBIAS` sample is a subset of the `ZEROBIAS` sample. Because of the prescale factor and the rate limits imposed to the `MINBIAS` trigger path, a reduction factor of $\sim 10^6$ is imposed on the overlapping events. Only 194 events are present in both samples. We use them only once, getting a negligible impact on the estimated integrated luminosity with respect to its uncertainty.

3.3 Offline

The offline selection can be summarized by a 4-steps strategy. Event by event:

1. we apply a "quality" selection on the online tracks using only the informations coming from the hits inside the tracking system. This first selection is necessary to reduce the fake track reconstruction;

2. we combine each tracks pair of same charge with all possible tracks of opposite charge and, fitting, we constrain them to a common vertex. If the fit returns a possible common origin we have a D^+ **candidate**. We then apply geometrical constraints to reject candidates reconstructed from unrelated tracks;

3. to reduce combinatorial background, we select only candidates with a decay vertex displaced from the primary vertex of interaction;

4. for each candidate found in the sample we estimate its invariant mass. Studying the $K\pi\pi$ invariant mass distribution we look for a signal at the expected D^+ mass. We apply an optimization strategy to extract the yield of the candidate.

We will discuss in more details each one of these four points in the next sections.

3.3.1 Good Run List

The CDF collaboration has defined a list of standard data-quality requirements (see Sec. 2.2.6) a run has to satisfy to be considered "good"; those runs are collected in the so-called `Good Run List` (GRL). All CDF analysis must conform to it. Furthermore, many specific good runs lists, dedicated to analyses based on different subdetectors status, have been developed by different groups. Which list is the most suitable for a certain analysis depends on the subdetectors it uses. That is why low p_T analyses that are not related to the muon systems can include runs where the muon systems is not working properly, but not runs were the COT is excluded or not working. In our case, a good list is made up only by runs where SVX II and the COT are working properly without further requirements on the other subdetectors. After applying the GRL selection, the ZB sample is reduced to about 141 millions of events, while the MB sample to about 85 millions of events.

3.3.2 Luminosity

Thanks to the measured rate of the inelastic $p\bar{p}$ events, $R_{p\bar{p}}$, (see Sec. 2.2.4), it is possible to estimate CDF II instantaneous luminosity by the following equation:

$$\mathcal{L} = \frac{R_{p\bar{p}}}{\sigma_{in} \cdot \epsilon_{CLC}} \tag{3.3}$$

where σ_{in} is the inelastic $p\bar{p}$ cross section at $\sqrt{s}$ = 1.96 TeV and ϵ_{CLC} is the CLCs acceptance. The only direct measurement of σ_{in} at the Tevatron has been performed at the beginning of Run I. At that time the center of mass energy was 1.8 TeV [26] [29]. Unfortunately, the inelastic cross section has not been measured anymore, even when the Tevatron achieved the higher and last center of mass energy of $\sqrt{s}$ = 1.96 TeV. The instantaneous luminosity used in the online and offline calculations is obtained by extrapolating the CDF and E811 combined measurements at $\sqrt{s}$ = 1.8 TeV to the project expected value $\sqrt{s}$ = 2 TeV. Even if the value of 2 TeV was never reached, for historical reasons the expected value has been used, overestimating the total $p\bar{p}$ cross section by about the 1.9%. In Table 3.1 are summarized the values of the integrated effective luminosities used in this analysis, L_{eff}. In the second column is shown the value of L_{eff}, after the 1.9% correction ($L = L_{\text{eff}} \cdot 1.019$):

	L_{eff} [1/nb]	$L_{\text{eff}} \cdot 1.019$ [1/nb]	syst
ZB	8.9	9.1	0.5
MB	6.8	6.9	0.4
Tot	15.7	16.0	0.9

Table 3.1: *Integrated effective luminosities correction for ZB, MB and total samples.*

In [30] the systematic uncertainty on the measured luminosity is assessed to be ~ 6%. Main contributions are due to uncertainties on the detector stability and calibration ($\leq 2.5\%$), ϵ_{CLC} (4.4%) and σ_{in} (4.0%).

3.3.3 Candidate selection

In each event, the D^+ candidates are reconstructed offline by combining all the possible triplets of tracks into a kinematic fit. We select tracks only in the η and p_T ranges where the reconstruction efficiency of the tracking system is high performing.

The base quality requests for the single track are the followings:

- SVX II small angle stereo hits $\geq +1$;
- SVX II stereo hits ≥ 2;
- SVX II axial hits ≥ 3;
- COT stereo hits ≥ 25;
- COT axial hits ≥ 25;
- $|\eta| \leq 1.2$;
- $p_T \geq 0.4$ GeV/c;
- $0 \leq |d_0| \leq 1$ mm.

The hits requests are needed in heavy flavour analysis for a good track reconstruction.

We consider all the possible triplets of tracks which pass the above selection. A triplet of good tracks is expected to satisfy the following criteria:

- $\sum_{i=1}^{3} |q_i| = 1$;
- $d_{0,max} \cdot d_{0,min} < 0$;
- $\Delta\varphi_{0,min} = |\varphi_{0,i} - \varphi_{0,j}| \geq 2°$;
- $\Delta z_{0,max} = |z_{0,max} - z_{0,min}| \leq 3$ cm;

where the index `i` and `j` refer to the tracks of the triplet; q_i is the charge of the track `i`; $d_{0,max}$, $d_{0,min}$, $z_{0,max}$, $z_{0,min}$ represent the track with the maximum or the minimum value of the impact parameter d_0 or of the z_0 coordinate; $\Delta z_{0,max}$ and $\Delta\varphi_{0,min}$ represent the maximum and minimum variation of the z_0 coordinate and φ_0 among the tracks of the triplet. We ask for $\Delta\varphi_{0,min} \geq 2°$ to avoid ghost tracks:

during the event reconstruction, for redundancy reasons, different pattern recognition alghoritms work indipendently, so the same track could be reconstructed by two of them with slightly different parameters and counted twice.

We fit the three tracks looking for a possible common origin point displaced by the primary vertex. We define the z coordinate of the *origin* vertex[2] as the weighted average of the tracks z_0. At this z coordinate we evaluate the beam position in the transverse plane and we set the x and y coordinates of the origin of the candidate. The fit converges only if the helices are within a certain threshold in the longitudinal direction. In case of slight incompatibility, the fitter modifies the track momentum to find an agreement; otherwise, if the tracks are totally incompatible, the reconstruction fails. A successful fit returns the candidate's decay vertex, the resulting global χ^2 of the fit and the new "rearranged" tracks. We have a candidate if the result of the fit satisfies the following base requests:

- $L_{\rm xy} \geq 0$ μm;
- $|y(D^+)| \leq 1$;
- $\chi^2_{red} \leq 10$;

where $y(D^+)$ is the candidate's rapidity and χ^2_{red} is the χ^2 of the fit divided by the number of degrees of freedom (n.d.f.).

In Figure 3.2 we show the invariant $K^-\pi^+\pi^+$ mass distribution of the candidates, selected as described above. No signal is observed with the base selection alone.

3.3.4 Evidence of the D^+ signal

On the basis of similar low-p_T analyses, we apply a strong cut, $L_{xy} \geq 750$ μm, to enhance the D^+ signal with respect to the background.

In Figure 3.3 is shown the invariant $K^-\pi^+\pi^+$ mass distribution for ZB, MB events and the summed samples, integrated over $p_T(D^+) \geq 1.5$ GeV/c. Because of the different trigger efficiency, the two samples should not be summed unless we assume that the two triggers have the same efficiency. We will justify this assumption in Section 6.1.1.2. In both the plots, it is possible to distinguish a clear peak at the expected D^+ mass ($m_{D^+} = 1.870\, GeV/c^2$).

3.3.5 Selection optimization

The requirements described in the previous subsections were set in order to unfold the D^+ signal from the background, considering the $p_T(D^+)$ integrated selection (i.e., $p_T(D^+) \geq 1.5\, GeV/c$). If the D^+ production is studied as a function of the D^+ transverse momentum, this selection is not guaranteed to be the best one as a

[2] position of the $p\bar{p}$ collision that generates the candidate.

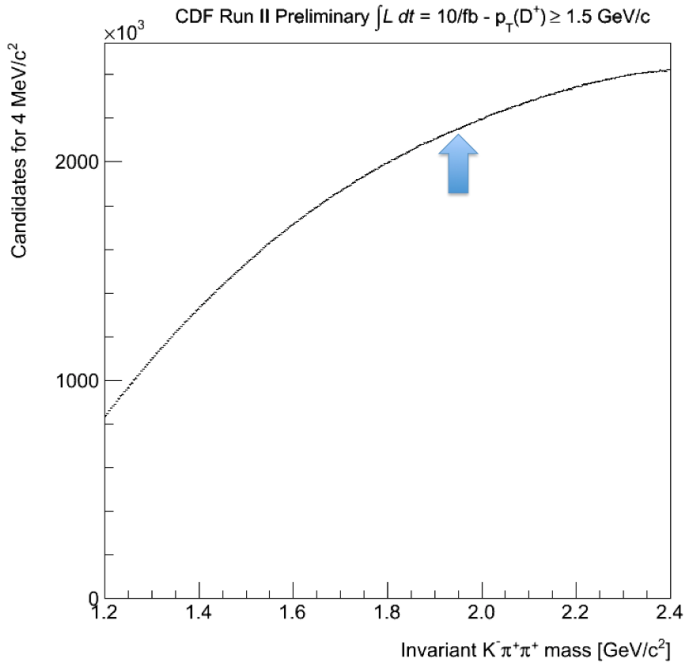

Figure 3.2: *Invariant $K^-\pi^+\pi^+$ mass distribution of the candidates obtained using the selection described in Sec. 3.3.3. The arrow indicates where the D^+ peak is expected.*

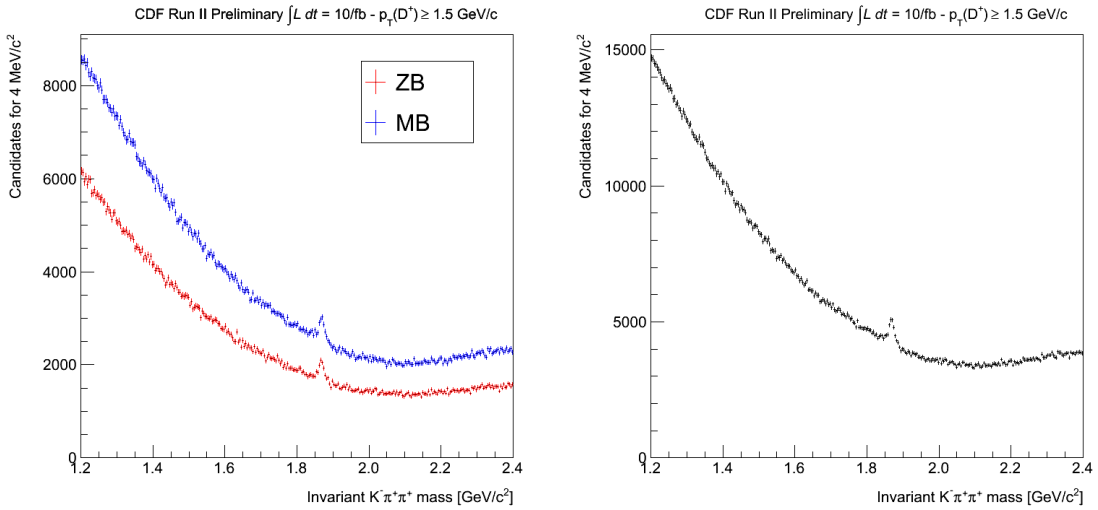

(a) (b)

Figure 3.3: *Invariant $K^-\pi^+\pi^+$ mass distribution for (a) the ZB (red) and MB (blue) samples and (b) for the summed samples obtained using the cut $L_{xy} \geq 750$ μm.*

function of $p_T(D^+)$. It is impossible to find the most performing selections using the Monte Carlo sample because it simulates only the signal and mainly because it needs as input the production cross section we want to measure. For this reason we use a pure data-driven optimization in order to obtain an unbiased technique. The statistics available is enough to probe the $p_T(D^+)$ range [1.5; 9.5] GeV/c in bins of 1 GeV/c each. We perform an optimization strategy of the selection *independently* in each $p_T(D^+)$ bin.

Let $\mathcal{M}$ be the data sample on which we want to optimize the selection.

1. A criterion is decided to identify the signal and background events which pass the selection, $\mathcal{S}$ and $\mathcal{B}$ respectively. We also choose the figure of merit, $f(\mathcal{S}, \mathcal{B})$, used to discriminate the different configurations for the selection requirements (e.g., all combinations of cuts).

2. Using a random criterion, we split $\mathcal{M}$ into two mutually exclusive subsamples, $\mathcal{A}$ and $\mathcal{B}$.

3. Considering the subsample $\mathcal{A}$, we scan the space of selection cuts and find the parameters that maximize our figure of merit, $f(\mathcal{S}^A, \mathcal{B}^A)$. The selection corresponding to the maximum of f optimizes $f(\mathcal{S}^A, \mathcal{B}^A)$.

4. The last two steps are repeated in sample $\mathcal{B}$ to obtain the set of cuts which optimize the sample $\mathcal{B}$: they are in general different from the ones obtained in sample $\mathcal{A}$.

5. We obtain the final sample applying to the subsample $\mathcal{B}$ the requirements optimized in subsample $\mathcal{A}$ and viceversa.

Splitting the sample $\mathcal{M}$ as described, we avoid statistical biases in the selection and, at the same time, we use all the statistics we have. This procedure fails in case of low statistics, because, in each splitted subsample the signal may be so small that the optimization is driven by statistical fluctuations. In the limit situations, it would be necessary to ensure that a fake signal cannot be built up from background clustering in that region of phase space. We are far from this pathologic cases, as evident in Figure 3.4, where are shown the signals for the sample $\mathcal{M}$ and for the two subsamples, $\mathcal{A}$ and $\mathcal{B}$, after applying the optimization method on the integrated selection.

For our tasks, the five points of the optimization method are performed as follows:

1. Considering the *i-th* configuration, signal ($\mathcal{S}_i$) and background ($\mathcal{B}_i$) are obtained through a binned likelihood fit on the invariant $K^-\pi^+\pi^+$ mass plot,

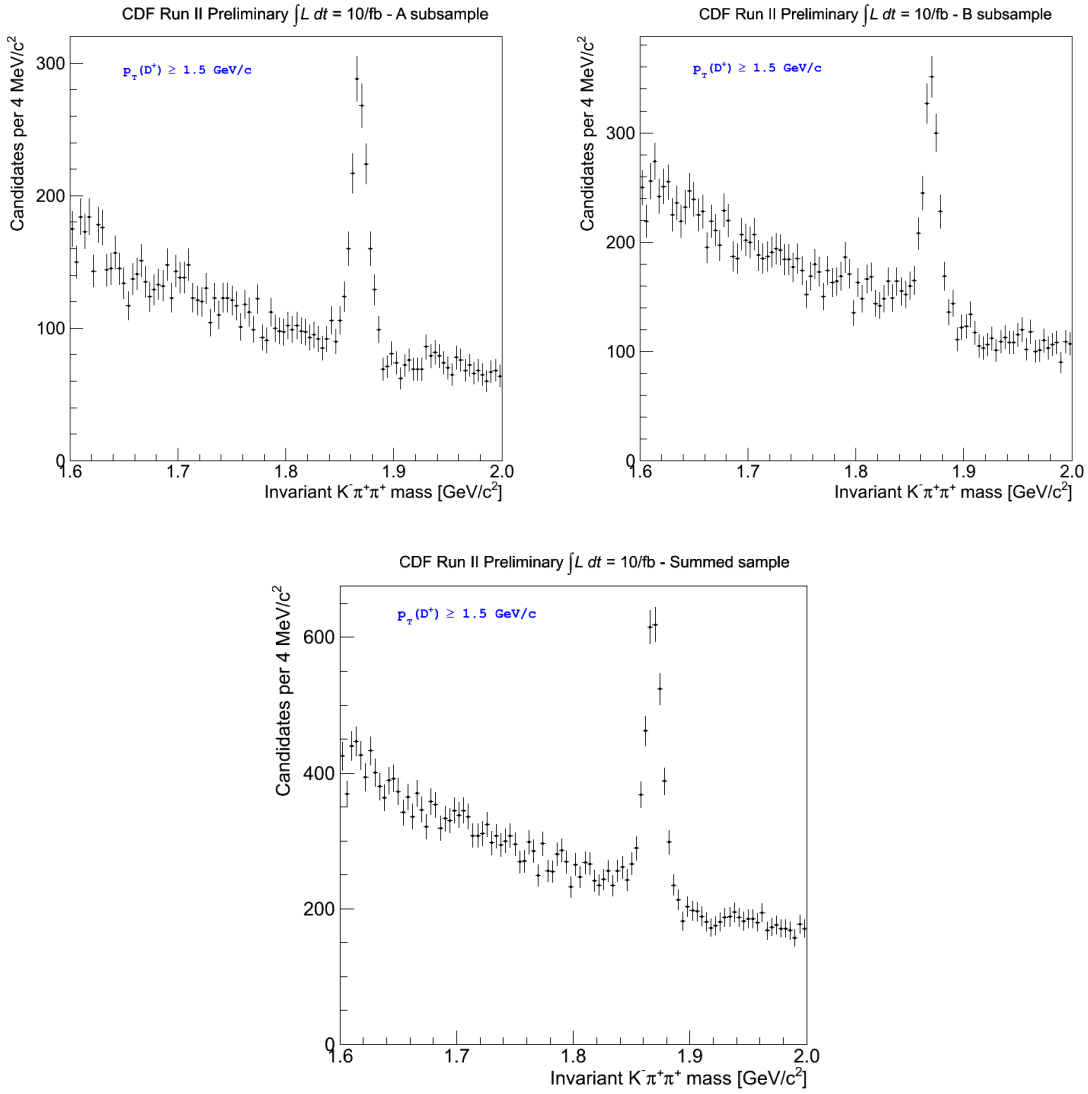

Figure 3.4: *Invariant $K^-\pi^+\pi^+$ mass distribution for the $\mathcal{A}$ (top-left), $\mathcal{B}$ (top-right) subsamples and the summed sample, $\mathcal{M}$, (bottom) obtained through the optimization in the $p_T(D^+)$-integrated sample.*

within 2σ around the D^+ peak, as we will describe in Sec. 5.2. As figure of merit we choose the following:

$$f(\mathcal{S}_i, \mathcal{B}_i) = \frac{\mathcal{S}_i}{\sqrt{\mathcal{S}_i + \mathcal{B}_i}}. \tag{3.4}$$

We use it because it minimizes the statistical uncertainty on the measured signal.

2. We use the event number as random criterion to divide the sample $\mathcal{M}$: we obtain two statistically independent subsamples with approximately same size, **even** and **odd** events respectively.

3. The selection of cuts used is listed in Table 3.2. We scan each variable for several different values, referred to as "steps". We consider 10 steps over the variable range.

   A selection configuration is defined as:

   - Any two $p_T(TRK^3) \geq p_{T,j}$;
   - $\gamma \leq \gamma_k$;
   - $|d_{0,max}| \geq d_{0,l}$ or $|d_{0,min}| \geq d_{0,l}$;
   - $\chi^2_{red} \leq \chi^2_{red,m}$;
   - $L_{xy} \geq L_{xy,n}$.

Variable	Range	Step
Any two $p_T(TRK)$	[0.4; 1.3] GeV/c	$p_{T,j}$ [0.1 GeV/c]
γ	[15; 1.5] deg	γ_k [1.5 deg]
$\|d_{0,max}\|$ or $\|d_{0,min}\|$	$[0; 675]\mu m$	$d_{0,l}$ [75 μm]
χ^2_{red}	[10; 0]	$\chi^2_{red,m}$ [1]
L_{xy}	$[0; 1450]\mu m$	$L_{xy,n}$ [150 μm]

Table 3.2: *Variables used for the optimization procedure. It is shown the range and the formalism adopted for the different steps.*

We evaluate all the possible combinations of cuts acting on the five variables, building a 5D cuts matrix, as visually described in Figure 3.5. Each configuration is coded with a simple number, C, where every digit represents the considered step for each variable: $C = jklmn$. For instance the code 50166, built using the matrix element within the dashed shapes, specifies the configuration: two $p_T(TRK) \geq 0.9 GeV/c$, $\gamma \leq 15°$, $|d_{0,max}| \geq 75\mu m$ or $|d_{0,min}| \geq 75\mu m$, $\chi^2_{red} \leq 4$ and $L_{xy} \geq 900\mu m$.

[3] From now, we write TRK meaning one of the decay TRacKs.

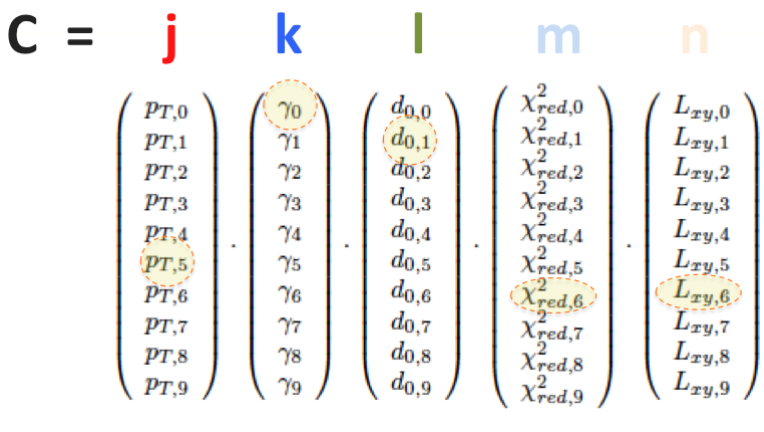

Figure 3.5: *5D cuts matrix, used for the optimization strategy.*

We maximimize the figure of merit over the space of selection cuts built by all combinations of requirements, *C-space*. The maximum of the figure of merit corresponds to the optimized cuts for the even subsample: C_E^{opt}.

4. We repeat the points 2 and 3 in the odd subsample finding the optimized code for the odd subsample: C_O^{opt}.

5. We swap the optimal configurations applying C_E^{opt} to the odd subsample and C_O^{opt} to the even subsample. The sum of the two optimized subsamples is our final sample.

Figure 3.6 graphically describes the complete procedure.

A typical plot of the figure of merit versus the configuration number is shown in Figure 3.7: several peaks are clearly visible, the highest one represents the best selection for the $p_T(D^+)$ considered bin.

Figures 3.8 and 3.9 show the distributions for the p_T bins we consider in this analysis: each one is obtained performing the optimization procedure discussed above.

In Table 3.3 we show the optimized cuts in different bins of $p_T(D^+)$ for the even subsample and odd subsamples.

3.3.6 Check of the optimization procedure

The criterion used for splitting the sample $\mathcal{M}$ is random. In case of infinite statistics, the optimized configuration found for a subsample should be the same as for the other subsample, otherwise it may be dominated by the fluctuations due to the optimization procedure. In order to check that this is not the case, we study the marginal-distributions: for each subsample, we fix 4 variables to the optimum

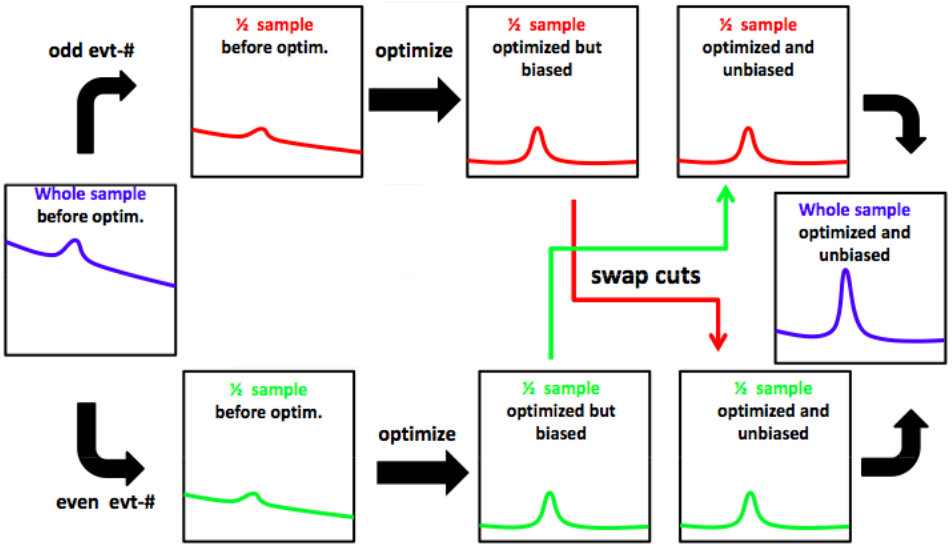

Figure 3.6: *Graphical scheme of the complete optimization strategy [23].*

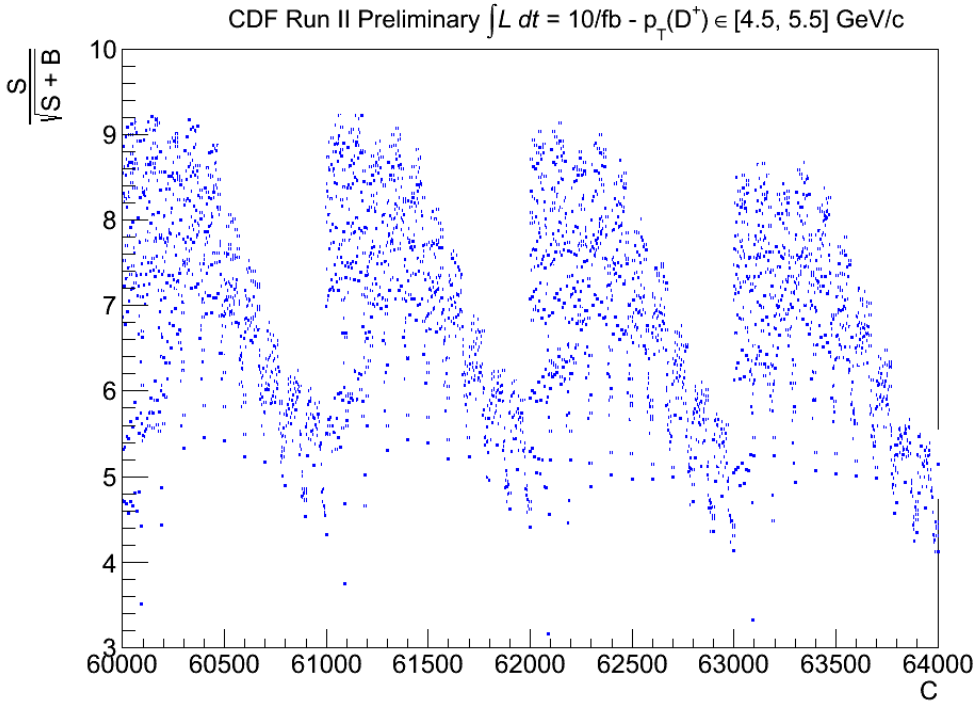

Figure 3.7: *Figure of merit versus the configuration number, C, for the even subsample in the range* $p_T(D^+) \in [4.5; 5.5]\ GeV/c$.

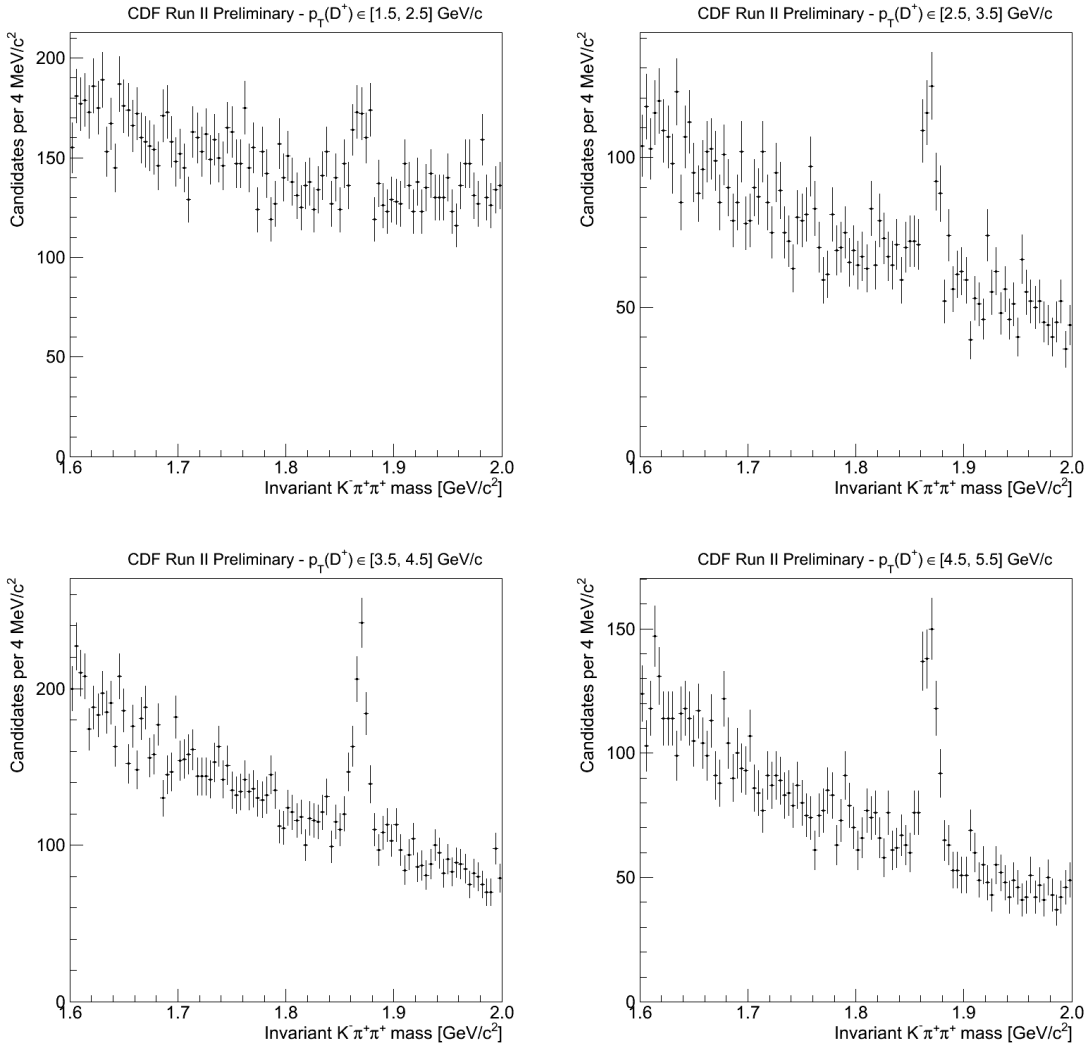

Figure 3.8: *Invariant $K^-\pi^+\pi^+$ mass distribution for the summed optimized sample in 1 GeV/c intervals of $p_T(D^+)$. The whole data sample is used.*

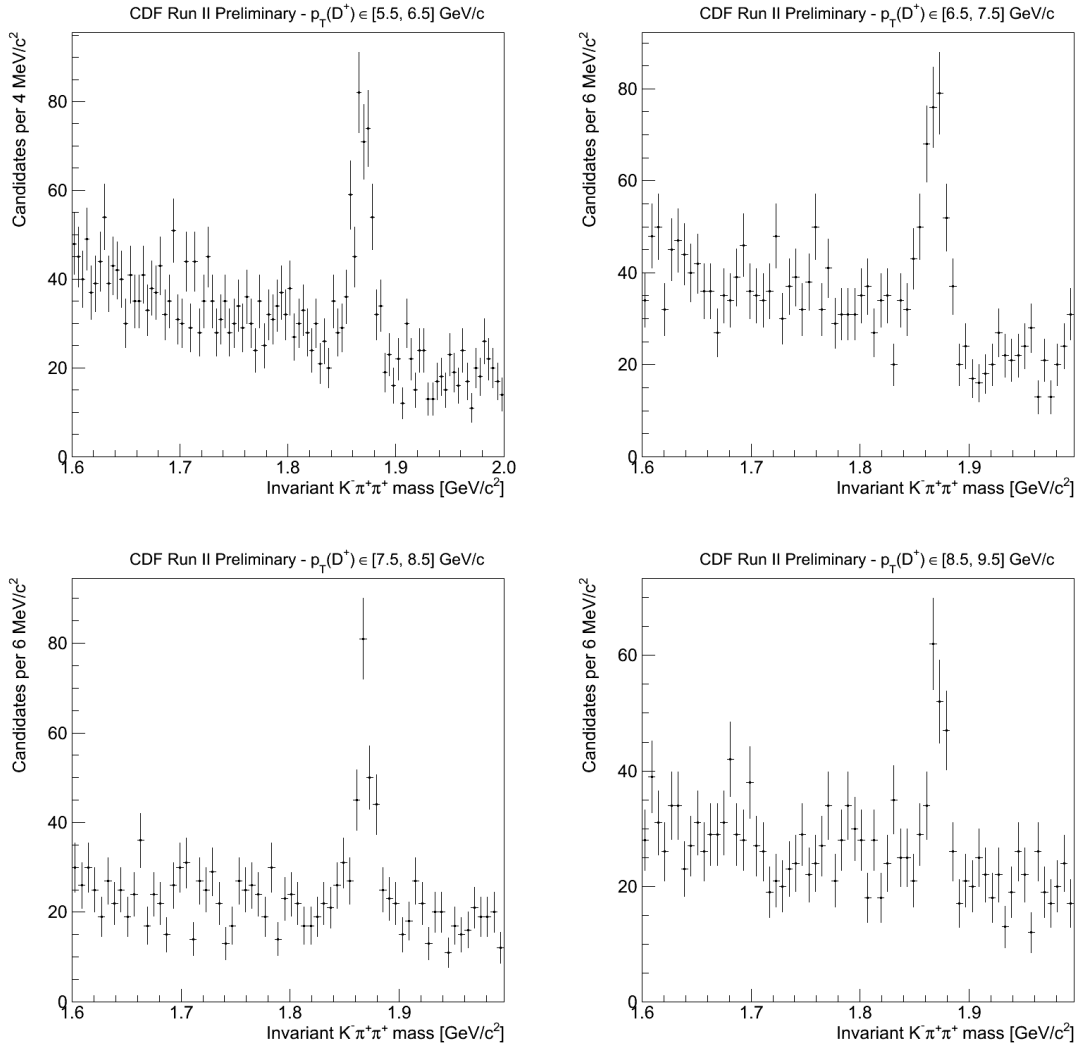

Figure 3.9: *Invariant $K^-\pi^+\pi^+$ mass distribution for the summed optimized sample in 1 GeV/c intervals of $p_T(D^+)$. The whole data sample is used.*

$p_T(D^+)[GeV/c]$	Parity	$p_{T,j}$ [GeV/c]	γ_k *deg*	$d_{0,l}$ $[\mu m]$	$\chi^2_{red,m}$	$L_{xy,n}$ $[\mu m]$
[1.5; 2.5]	Even	0.6	9	375	2	600
	Odd	0.6	10.5	300	4	450
[2.5; 3.5]	Even	0.5	7.5	375	4	450
	Odd	0.6	7.5	300	4	900
[3.5; 4.5]	Even	0.8	15	0	2	600
	Odd	0.8	15	150	6	600
[4.5; 5.5]	Even	0.8	15	0	6	900
	Odd	0.8	15	0	8	750
[5.5; 6.5]	Even	1.1	15	0	4	1050
	Odd	1.1	15	75	6	750
[6.5; 7.5]	Even	1.0	15	0	9	900
	Odd	1.0	15	75	4	750
[7.5; 8.5]	Even	1.0	15	150	9	450
	Odd	1.0	15	0	6	1050
[8.5; 9.5]	Even	1.2	15	0	6	300
	Odd	1.2	15	0	5	750

Table 3.3: *Optimized cuts in different bins of* $p_T(D^+)$ *for the even and odd subsamples.*

values determined by the optimization procedure and we scan the last one over its optimization steps.
The marginal-distributions, considering the optimized selection for the $p_T(D^+)$-integrated sample, are shown in Figure 3.10.

The maximum determined by the two subsamples coincides for γ[4] and χ^2_{red}. For L_{xy}, $p_T(TRK)$ and $|d_{0,max}|, |d_{0,min}|$ the overlapping is within one or two optimization steps: this behaviour is still acceptable because these three variables are highly correlated: fluctuations due to one of them can be balanced by the fluctuations due to the others. The correlation between these three variables is illustrated in Figures from 3.11 to 3.13, for different cuts on $p_T(D^+)$.

3.3.7 Selection requirements

The selection used (Table 3.2) relies on cutting on the p_T of two of the tracks and on the maximum and minimum d_0 among all three tracks. We verify if it's possible to improve the candidate yield by requiring a cut on all three tracks for the variables p_T or d_0 respectively.

[4]For both even and odd γ distributions in Figure 3.10, the first experimental point is the maximum.

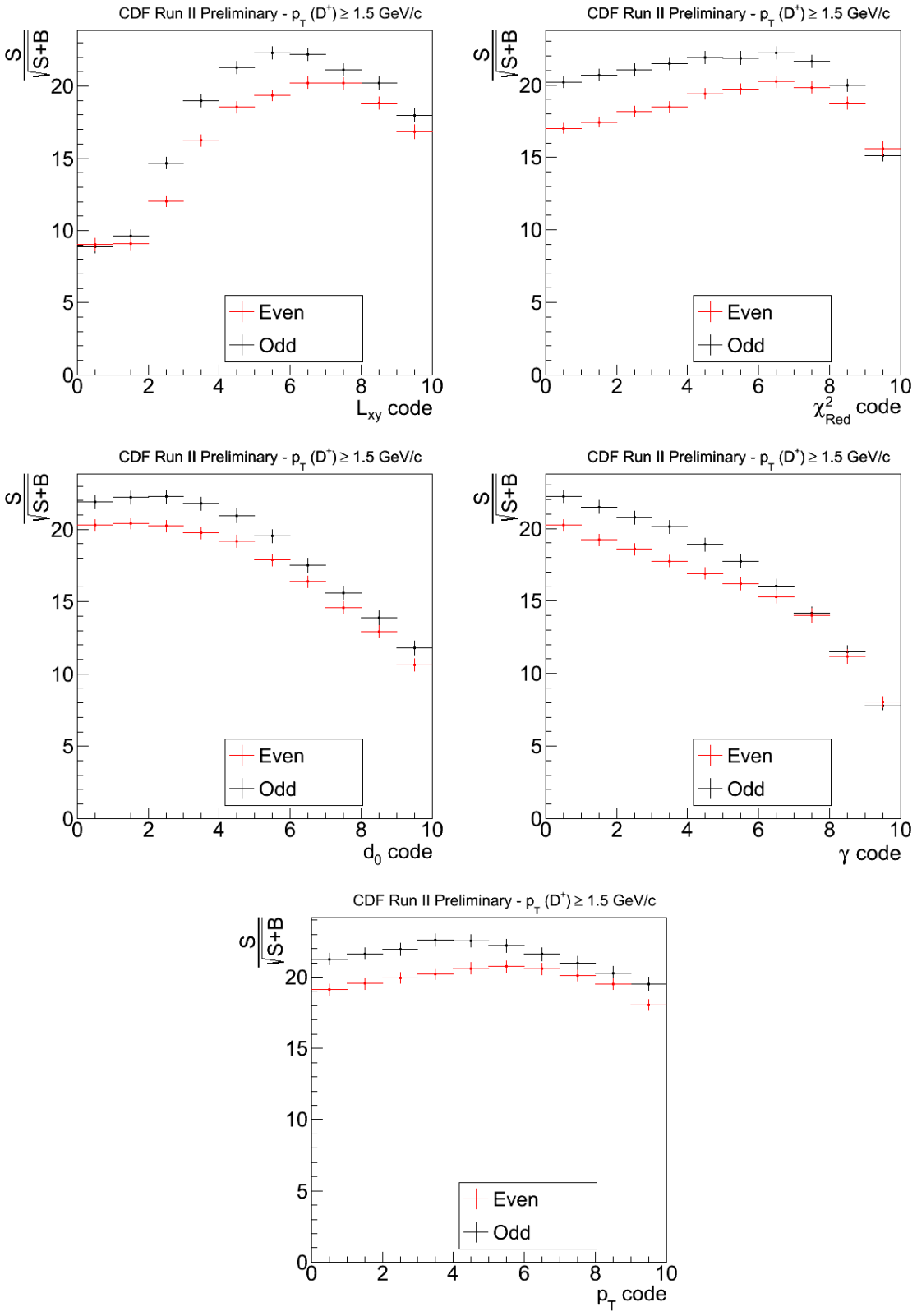

Figure 3.10: *Marginal-distributions for L_{xy}, χ^2_{red}, $|d_{0,max}|$, $|d_{0,min}|$, γ and $p_T(TRK)$. Both even (red) and odd (black) distributions are shown. The whole data sample is used.*

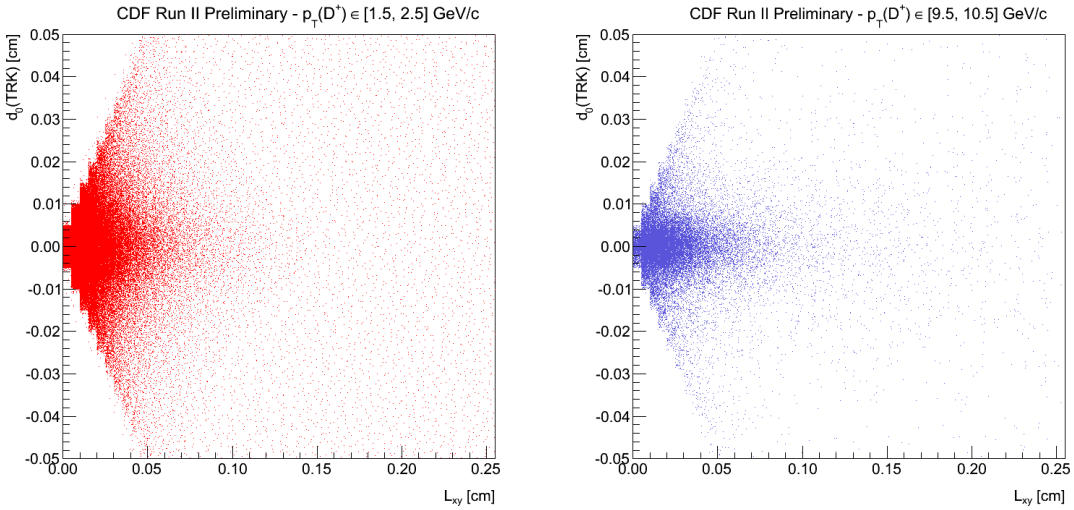

(a)

(b)

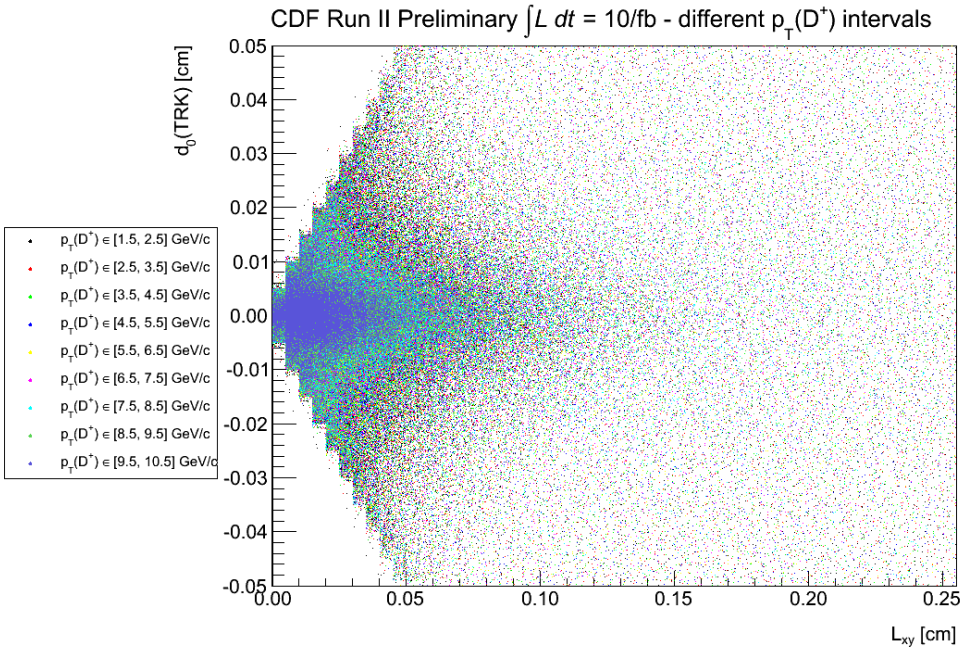

(c)

Figure 3.11: *2D-scatter plot between the variables L_{xy} and $d_0(TRK)$ for two intervals of $p_T(D^+)$ and for all the intervals of $p_T(D^+)$: (a) $p_T(D^+) \in$ [3.5; 4.5] GeV/c; (b) $p_T(D^+) \in$ [9.5; 10.5] GeV/c and (c) all the intervals of $p_T(D^+)$. The whole data sample is used.*

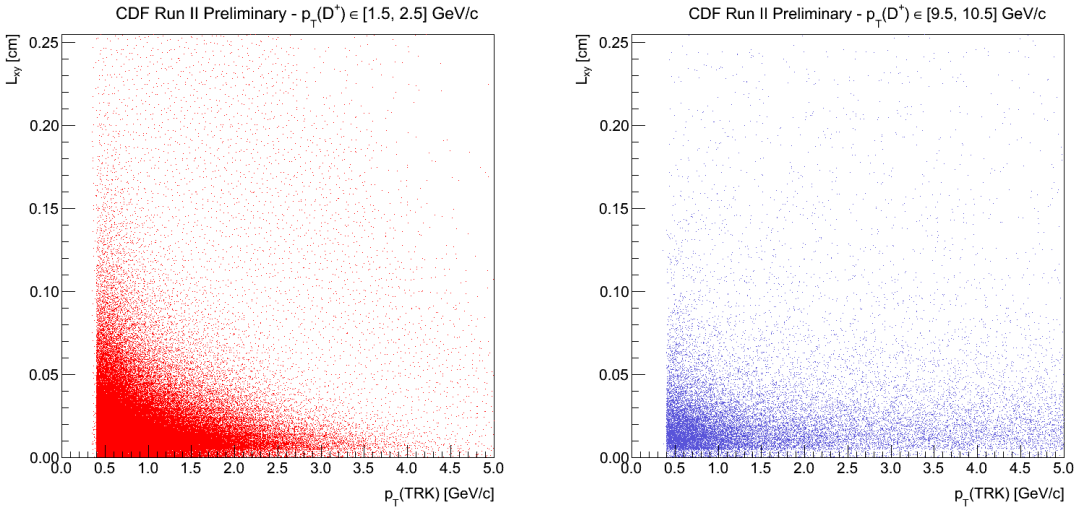

(a)

(b)

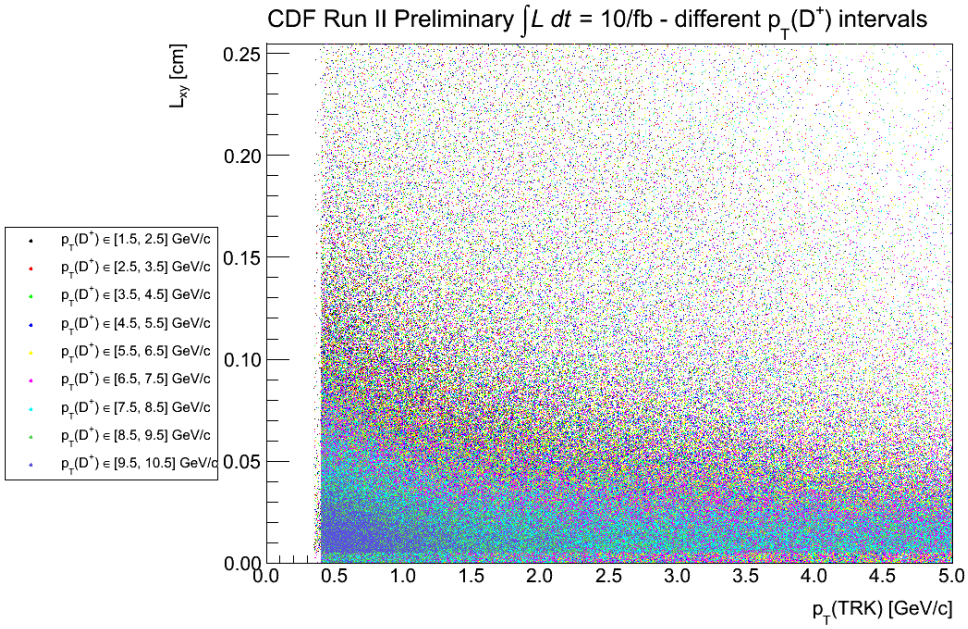

(c)

Figure 3.12: *2D-scatter plot between the variables $p_T(TRK)$ and L_{xy} for two intervals of $p_T(D^+)$ and for all the intervals of $p_T(D^+)$: (a) $p_T(D^+) \in$ [3.5; 4.5] GeV/c; (b) $p_T(D^+) \in$ [9.5; 10.5] GeV/c and (c) all the intervals of $p_T(D^+)$. The whole data sample is used.*

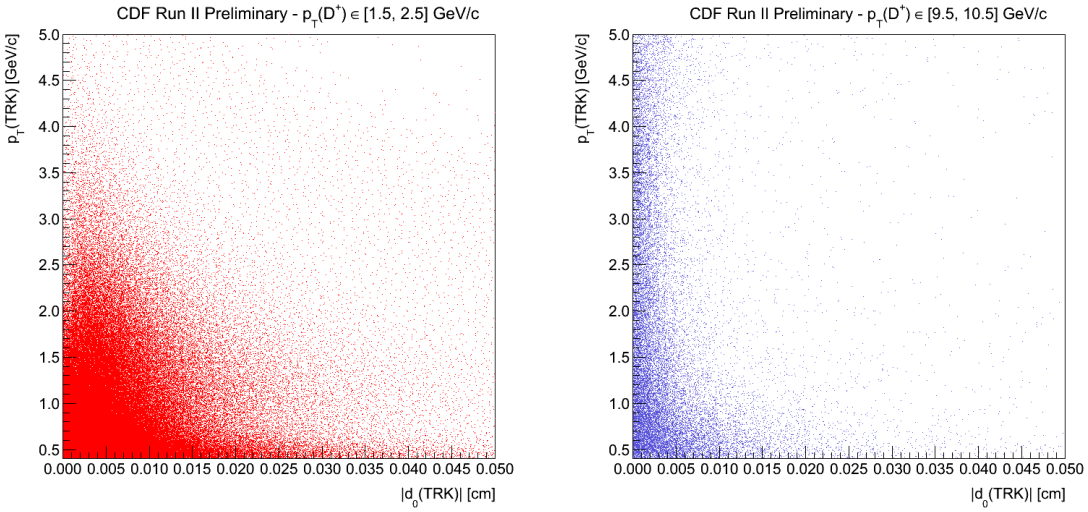

(a)

(b)

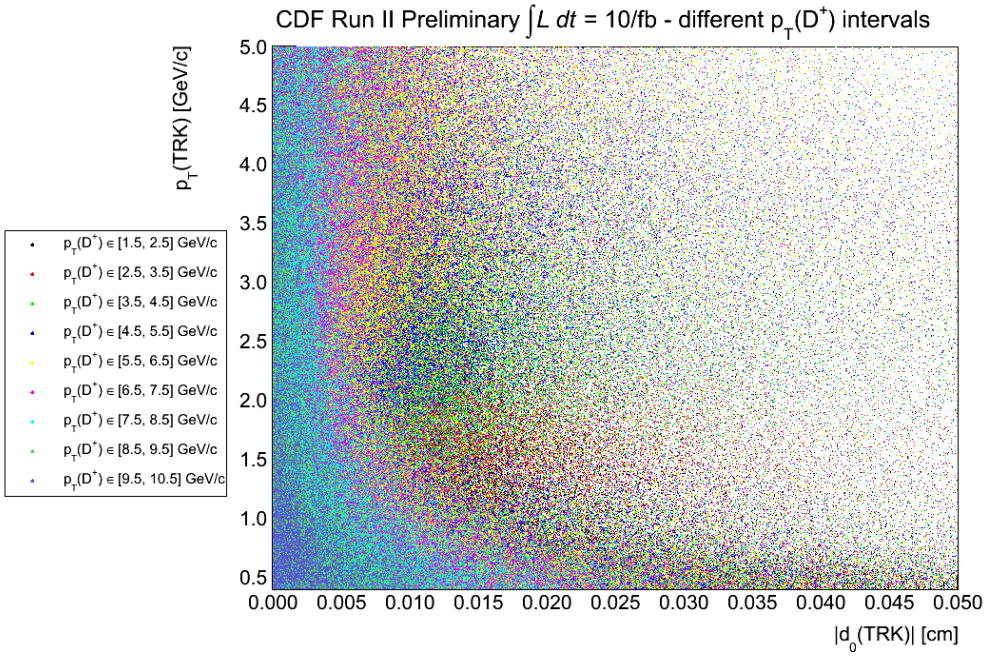

(c)

Figure 3.13: *2D-scatter plot between the variables $p_T(TRK)$ and $|d_0(TRK)|$ for two intervals of $p_T(D^+)$ and for all the intervals of $p_T(D^+)$: (a) $p_T(D^+) \in$ [3.5; 4.5] GeV/c; (b) $p_T(D^+) \in$ [9.5; 10.5] GeV/c and (c) all the intervals of $p_T(D^+)$. The whole data sample is used.*

A good selection of the sample should be efficient and pure: it should maximize the number of D^+ which pass the selection and it should minimize the contamination by fake candidates. We use the signal yield and the figure of merit $\frac{S}{\sqrt{S+B}}$ for testing the efficiency and purity of the selection. For this reason, considering the optimized selection for the $p_T(D^+)$-integrated sample, we extract the signal yield and we calculate the figure of merit fitting the invariant $K^-\pi^+\pi^+$ mass (the fitting procedure will be explained in more details in Sec. 5.2). We perform two different studies in order to test separately the goodness of the cut on the $p_T(TRK)$ and on the $d_0(TRK)$.

We fix the cuts on all variables, but we vary the cut on the $p_T(TRK)$. We cut on the p_T of all three tracks, as shown in Figure 3.14(a), and on the p_T of only two tracks, as shown in Figure 3.14(c). For both selections we determine the signal yield and the figure of merite and we compare them. By cutting on two tracks we increase of the 51% the signal efficiency and of the 17% the signal purity. We cut on two tracks in p_T.

We perform the same study for the variable $d_0(TRK)$. Again, fixing the cuts on all variables we vary the cut on $d_0(TRK)$. We cut on the d_0 of all three tracks, as shown in Figure 3.14(b), and only on the maximum and minimum $d_0(TRK)$, as shown in Figure 3.14(c). We compare the figure of merit and the signal yield determined from both selections. In this case, by cutting on two tracks, we increase of the 91% the signal efficiency and of the 33% the signal purity. We cut on the maximum and minimum $d_0(TRK)$.

Other selection requirements, studied in this analysis, are described in Appendix B.

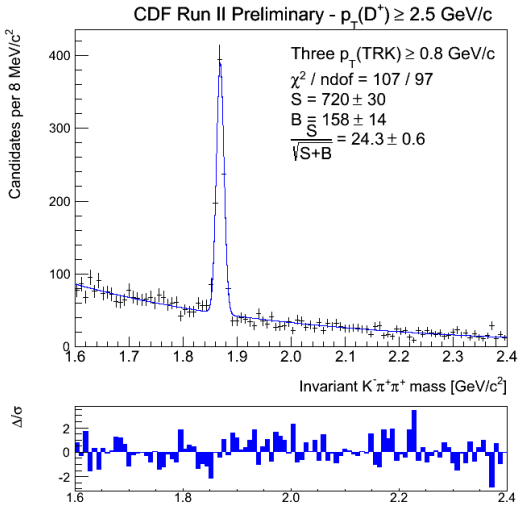

(a) three p_T cuts and on $|d_{0,max}|$ or $|d_{0,min}|$.

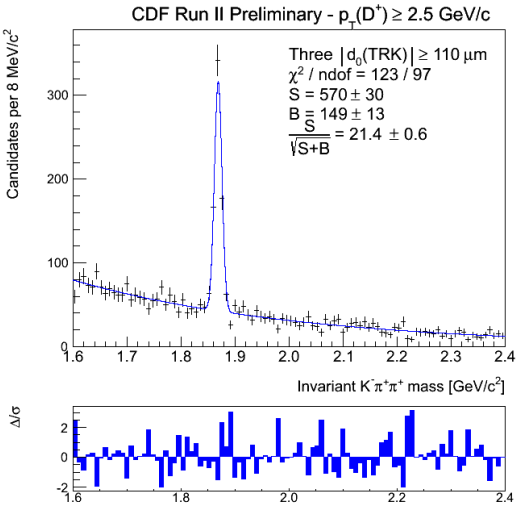

(b) three d_0 cuts and two p_T cuts.

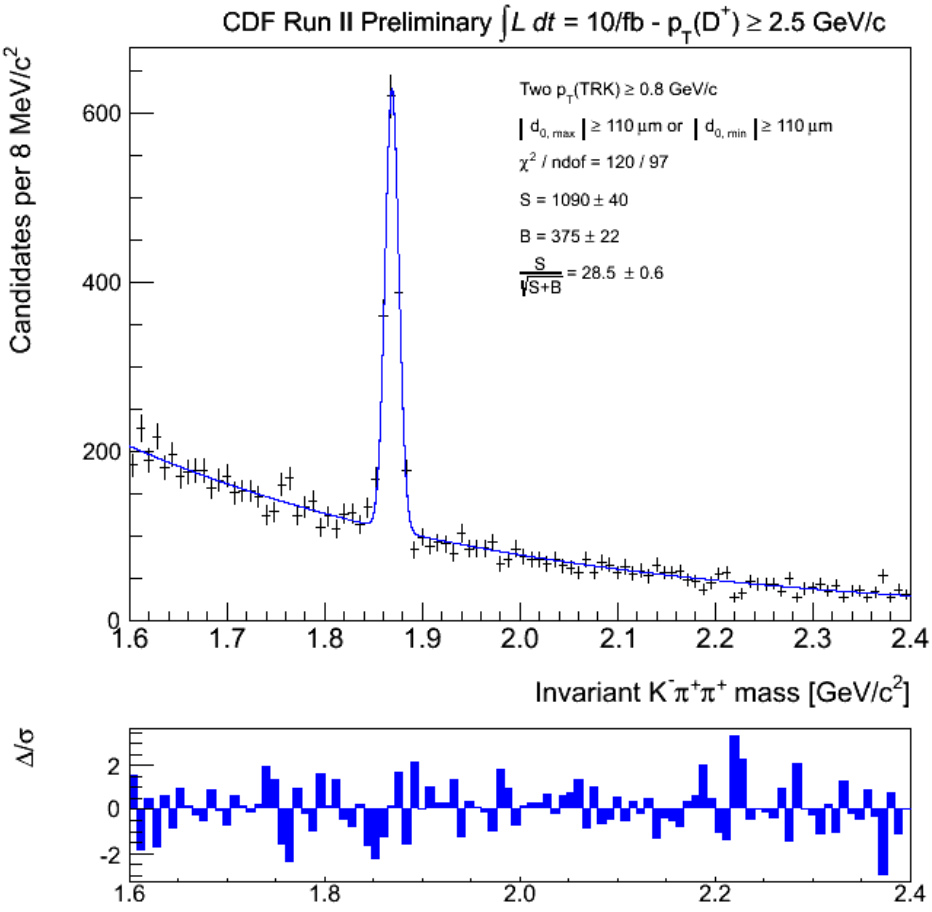

(c) two p_T cuts and on $|d_{0,max}|$ or $|d_{0,min}|$.

Figure 3.14: *Invariant $K^-\pi^+\pi^+$ mass fit of data for different $p_T(D^+)$-integrated selections. The whole data sample is used.*

Chapter 4

Data and Monte Carlo comparison

This chapter briefly describes the MC samples used in this analysis. A simulation is needed in order to model the signal shape and to evaluate the reconstruction efficiency. We also compare the distributions for the variables we use in the optimization procedure with their MC simulations.

4.1 Monte Carlo (MC) samples

In high energy physics experiments, like CDF II, it is often necessary to estimate the fraction of events escaping from the detector (i.e. the detector acceptance), the expected detector response to the passage of a particle or to predict the shape of a particular signal. To fulfill these requirements, Monte Carlo (MC) simulation techniques are generally used. In fact, the complex geometry of the experiment, the enormous number of variables to consider or the number of effects to take into account, don't allow an analytical prediction of the relevant distributions.

These MC techniques can be applied at two different levels:

1. event generation;

2. detector simulation;

Sometimes it is also required a trigger simulation, but for this analysis we don't need it.

1. Generation simulation. The event generation describes all the processes that originate from the $p\bar{p}$ collision, starting from the partons interactions up to the final formation of the hadrons. CDF II exploits different generators according to the various purposes. We use only the *BGENERATOR* [31].

2. Detector simulation. The detector simulation, instead, mimics the passage of the generated particles inside the detector volume, the signals they produce and the response of the CDF II subdetectors.

We use a MC sample in this analysis for different purposes:

- determine the signal shape for each bin of p_T. Such shape is needed to perform the fit of the yields (See Sec. 5.3);

- estimate the reconstruction efficiency of our selection (See Sec. 6.1.2).

4.1.1 Generation: BMC

The BGENERATOR is used in the CDF B Monte Carlo (BMC). This generator is explicity thought for beauty and charm physics. It simulates the production and fragmentation of b and c quarks and the resulting hadrons are decayed using QQ (the CLEO Monte Carlo generator adapted for CDF II package) [32]. We force the generated D^+ to decay into the $K^-\pi^+\pi^+$ channel we are studying. Finally, it is simulated the propagation of the decay products toward the CDF II detector. The BGENERATOR algorithm needs the joint distribution of transverse momentum and rapidity for the generated quark as input information. We use realistic input distributions that scan the $y - p_T$ plane in $[-1.3,\ 1.3] \times [0,\ 15]$ GeV/c. In order to reproduce the same online selection, no trigger simulation and selection is performed.

4.1.2 Detector simulation

After the decay particles are generated, they are propagated towards the detector volume. Interactions with detectors materials are reproduced. Also, the responses of the different sub-detectors are simulated. To model the detector geometry and materials, the standard CDF II simulation uses the version 3 of the GEANT package [33]. It is tuned by data from test-beams and collision data. Position and four-momentum of each particle produced by the simulated collisions and able to overtake the beam pipe, are requested by GEANT in input. Then, it is reproduced their passage through the detector and all the interactions that take place: bremmstrhalung losses, multiple scattering, pairs production etc ...

Many sub-detectors are simulated by specific packages rather than GEANT. For instance, GFLASH [34] replaces GEANT to mimic the calorimeter response. It is a parametric shower-simulator tuned from single particle response and shower shape using test beam data (8-230 GeV/c electrons and charged pions) and collision data (0.5-40 GeV/c single isolated tracks).

For the silicon detector, a parametric charge deposition model, tuned on data, is exploited. It accounts for restricted Landau distribution, production of δ rays, capacitive charge sharing between neighboring strips, noise, etc ... While the GARFIELD standard package [35], tuned on data, mimics the drift time within the COT.

Between the data acquisition periods, the detector and trigger configuration underwent several changes. For instance, after major hardware improvements, large modifications occurred. At the same time, relative mis-alignments between subdetectors, local or temporary inefficiencies of the silicon tracker (active coverage, noisy

channels, etc ...) must be considered. In order to have a more detailed simulation of the actual experimental conditions, the off-line database is used to tune the simulation. In such a way, on a run by run basis, all known variations in configuration are taken into account. So, a detailed simulation of real runs is available, allowing to match, in any given sample, the distribution of data and MC. To analyse simulated data with the same reconstruction programs used for data, the two samples share the same output format. The MC events follow the same reconstruction chain as data and, after the detector simulation, we apply the same candidate selection performed on data. In Figure 4.1 the resulting invariant $K^-\pi^+\pi^+$ mass distribution in linear and logarithmic scale is shown. A long tail at lower masses is evident: it represents the soft photon emission.

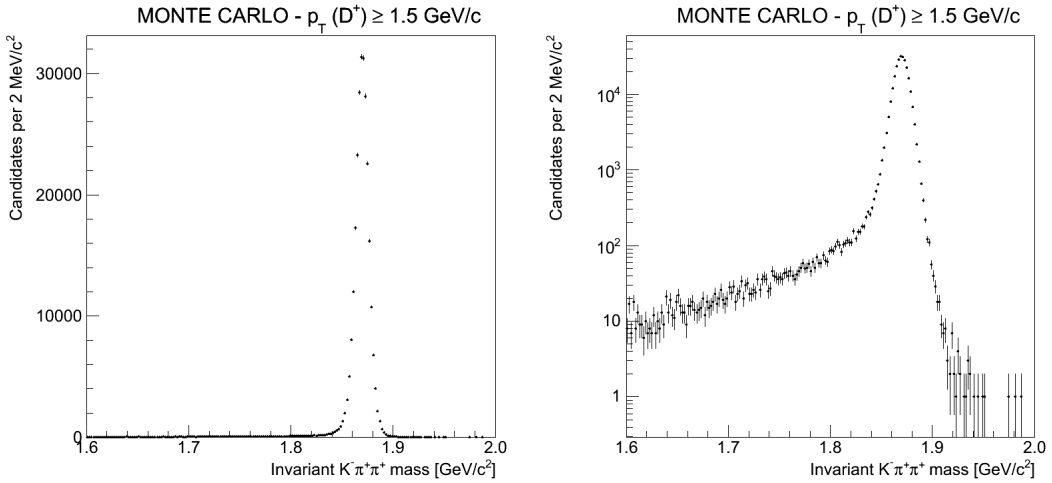

Figure 4.1: *Invariant $K^-\pi^+\pi^+$ mass distribution of candidates reconstructed in the $D^+ \to K^-\pi^+\pi^+$ MC sample. Left side: linear scale; right side: logarithmic scale.*

4.2 Signal shape

The statistics in our data allow us to measure the D^+ yields as a function of $p_T(D^+)$. The invariant $K^-\pi^+\pi^+$ mass plot is made by two components: signal and backgorund. To extract the raw yield of candidates for each bin, we have to model the shapes of these components. For the signal we use the BMC sample. We simulate the shape of the signal for each bin, using the MC sample: the shapes obtained are then parametrized and used to fit the data. We parametrize the mass line shape of the signal candidate with a sum of two Gaussians plus a long tail at lower masses to take into account the soft photon emission. The probability density function (PDF)

is defined as follows:

$$\wp_{\mathrm{Sgl}}(m;\vec{\theta}_{\mathrm{Sgl}}) = f\cdot[s\cdot\mathscr{G}(m;m_{D^+}+\delta_1,\sigma_{D^+}) + (1-s)\cdot\mathscr{G}(m;m_{D^+}+\delta_2,\sigma_2)]+ \\ +(1-f)\cdot\mathscr{T}(m;b,c,m_{D^+}+\delta_1) \tag{4.1}$$

where:

- f is the relative fraction of the double Gaussian contribution with respect to the total;
- $\mathscr{G}(m;\mu,\sigma)$ represents the parametrization of the gaussian functions; it is defined as follows:
$$\mathscr{G}(m;\mu,\sigma) = \frac{1}{\sigma\sqrt{2\pi}}e^{-\frac{(m-\mu)^2}{2\sigma^2}}; \tag{4.2}$$
- s is the relative fraction of the Gaussian labeled with the index *1* with respect to the sum of the two Gaussians;
- σ_{D^+} and σ_2 are the width of the Gaussian 1 and 2; $\delta_{1(2)}$ is a mass shift from the imput mass value m_{D^+}, due to the asymmetry induced by the soft photon emission.
- $\mathscr{T}(m;b,c,\mu)$ represents the parametrization of the radiative tail; it is defined as follows:
$$\mathscr{T}(m;b,c,\mu) = \frac{1}{K}e^{b(m-\mu)}\cdot\mathrm{Erfc}[c(m-\mu)] \tag{4.3}$$
$$K = \int_{m_{\min}}^{m_{\max}} e^{b(m-\mu)}\cdot\mathrm{Erfc}[c(m-\mu)]dm \tag{4.4}$$
$$\mathrm{Erfc}(x) = 1-\mathrm{Erf}(x) = \frac{2}{\sqrt{\pi}}\int_x^{+\infty} e^{-t^2}dt. \tag{4.5}$$
- $\vec{\theta}_{\mathrm{Sgl}}$ is the vector of the signal parameters that have to be fitted: $\vec{\theta}_{\mathrm{Sgl}} = \{m_{D^+}, s, \delta_1, \sigma_{D^+}, \delta_2, \sigma_2, f, b, c\}$. It is extracted by fitting the simulated invariant $K^-\pi^+\pi^+$ mass distribution when a D^+ is generated.

Figures from 4.2 to 4.5 show the result of this parametrization for the signal, for each bin of $p_T(D^+)$ between 1.5 GeV/ and 9.5 GeV/c. The small discrepancies in the tails are negligible with respect to the measurement uncertainties. We find no dependence on $p_T(D^+)$ for the signal width.

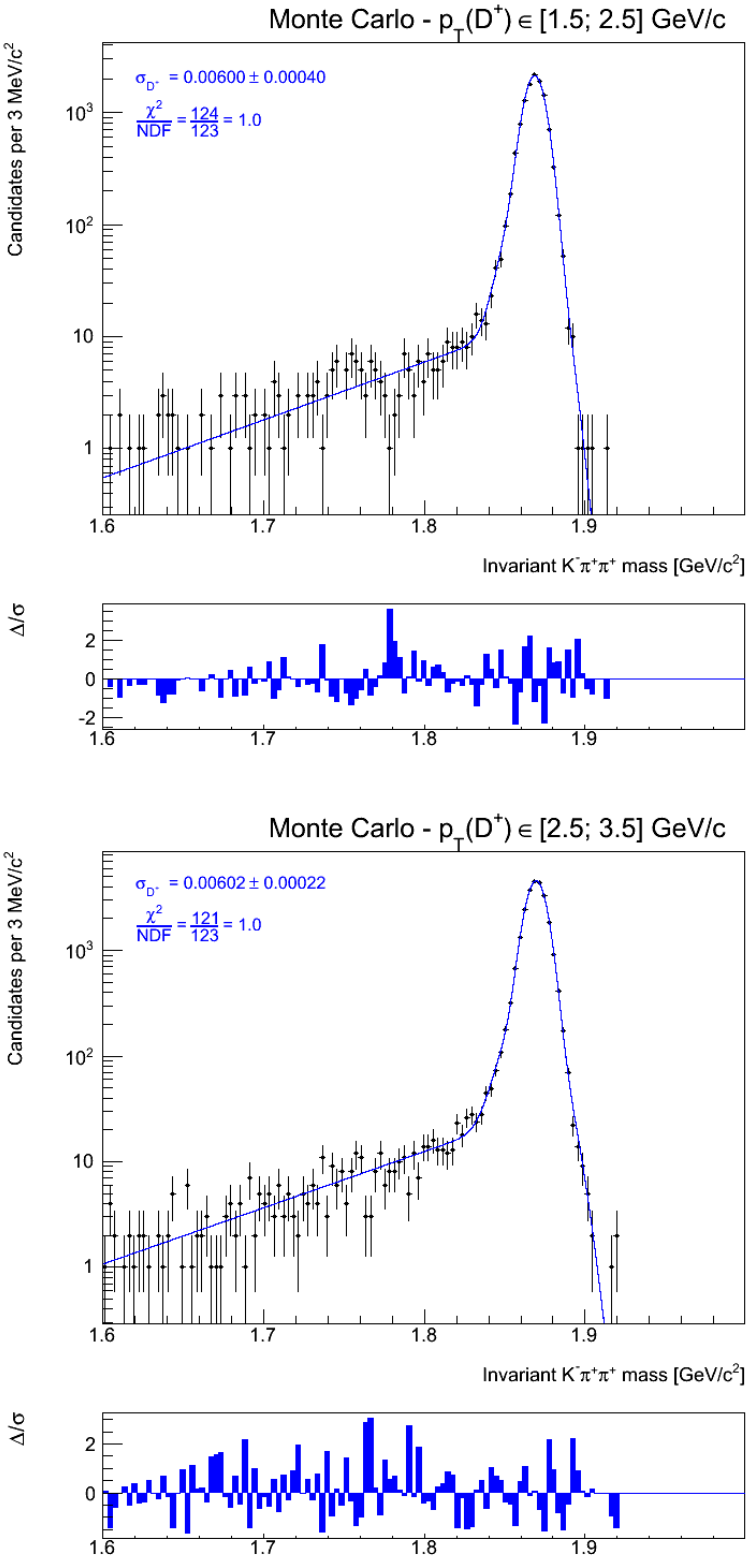

Figure 4.2: *Invariant $K^-\pi^+\pi^+$ mass fit of MC events in 1 GeV/c intervals of $p_T(D^+)$. Fit residuals are also shown.*

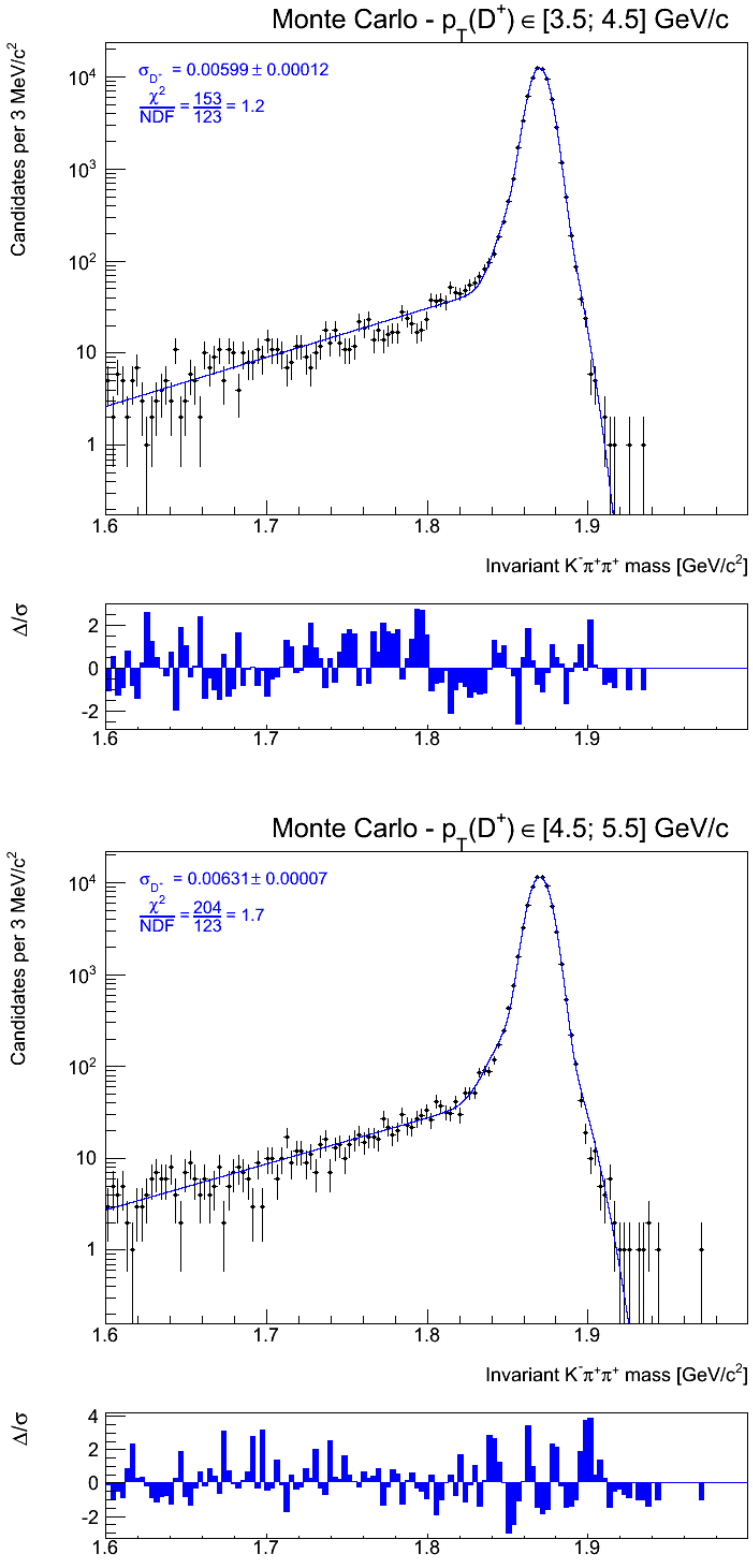

Figure 4.3: *Invariant $K^-\pi^+\pi^+$ mass fit of MC events in 1 GeV/c intervals of $p_T(D^+)$. Fit residuals are also shown.*

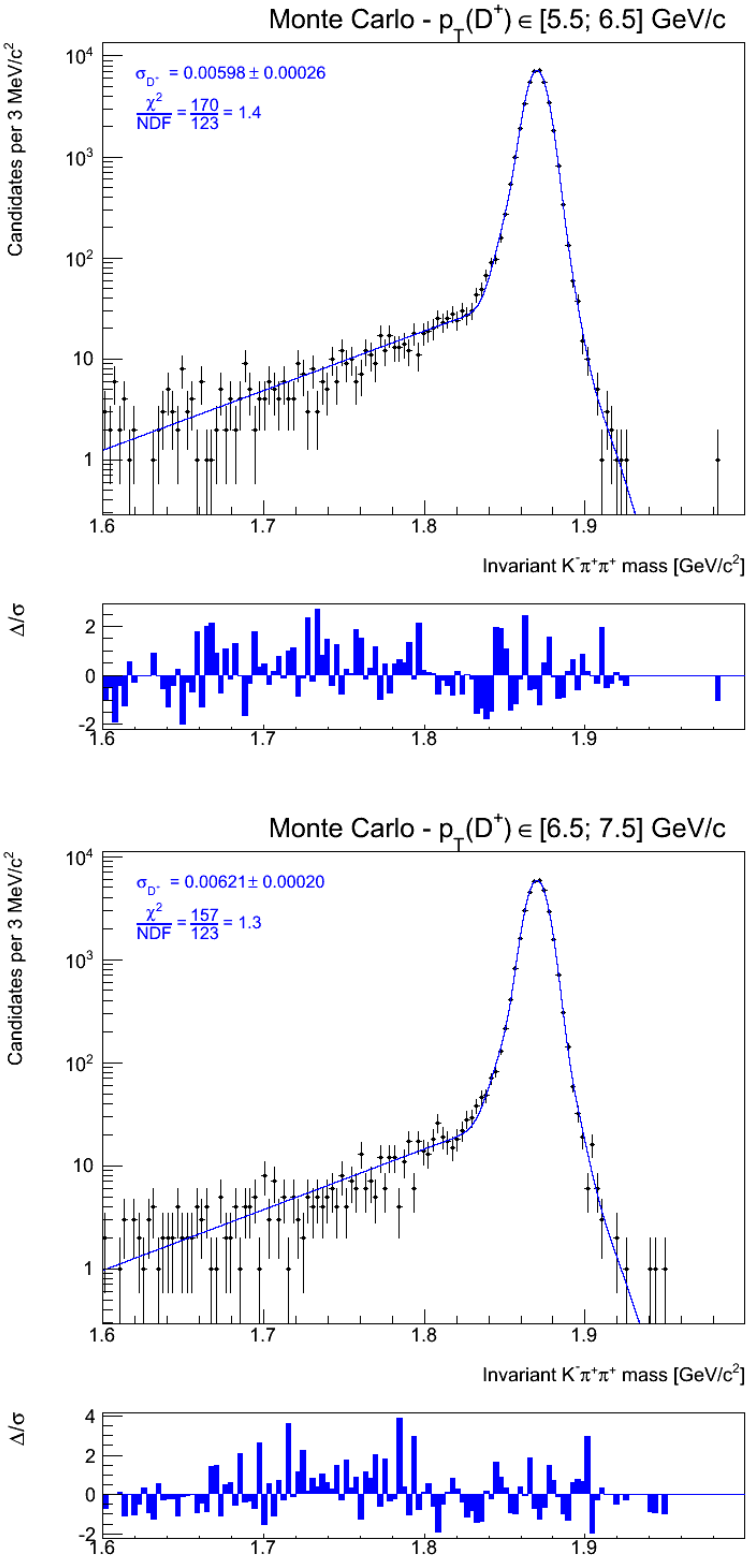

Figure 4.4: *Invariant $K^-\pi^+\pi^+$ mass fit of MC events in 1 GeV/c intervals of $p_T(D^+)$. Fit residuals are also shown.*

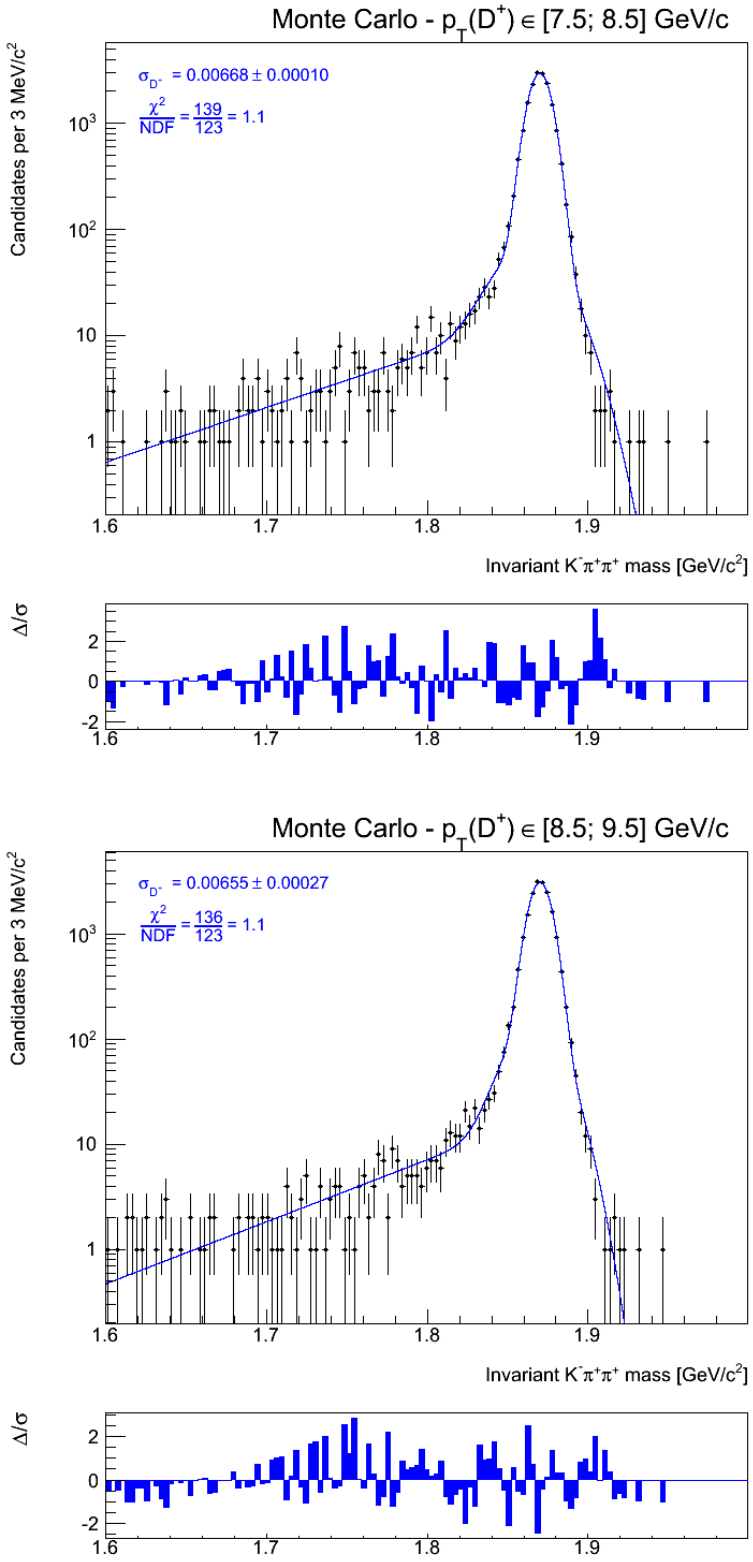

Figure 4.5: *Invariant $K^-\pi^+\pi^+$ mass fit of MC events in 1 GeV/c intervals of $p_T(D^+)$. Fit residuals are also shown.*

4.3 Variables simulation

When analyses make use of MC simulations, it is recommended to test their accuracy in reproducing the real data. In our case, we need MC samples to evaluate the reconstruction efficiencies. When simulations are not reliable, a bias in the efficiencies is introduced and it propagates to the final cross section measurement.

We scan the sample using the optimized selection integrated in $p_T(D^+)$:

- two $p_T(TRK) \geq 0.8$ GeV/c.
- $\gamma \leq 15°$;
- $|d_{0,max}| \geq 110\mu m$ or $|d_{0,min}| \geq 110\mu m$;
- $\chi^2_{red} \leq 4$.
- $L_{xy} \geq 900$ μm.

We test the MC simulation of each variable used in our analysis by comparing three distributions: side band, signal region and MC distributions.

On the basis of the parametrization used for the signal shape, we define the **signal region** as the region of 2σ around the D^+ peak: $[m_{D^+} - 2\sigma_{D^+};\ m_{D^+} + 2\sigma_{D^+}]$; this region contains both background and signal candidates. We define also the **Side Bands (SB)** as the regions of the invariant mass plot comprised in $[m_{D^+} - 5\sigma_{D^+},\ m_{D^+} - 7\sigma_{D^+}]$ and $[m_{D^+} + 5\sigma_{D^+},\ m_{D^+} + 7\sigma_{D^+}]$; only background candidates are present in these regions. The colored regions in Figure 4.6 indicate the SB for the $p_T(D^+)$-integrated sample.

In order to obtain the distribution of the signal only candidates, we extrapolate the SB yield in the signal region and we subtract it from the signal region. Figures 4.7 and 4.8 show the comparison of the distributions for a single variable in the MC sample (red), in the data SB (green) and in the signal region after subtracting the side bands (blue). The SB distribution of the $d_0(TRK)$ exhibits a peak centered at about 0 μm: combinatorial tracks produced in the $p\bar{p}$ interaction originate it.

An overlap for blue and red distributions means that the MC simulation is able to reproduce the signal shape. That's true for all the variables but for the χ^2_{red}, as evident in Figure 4.7(a).

The actual regions used to define the SB samples ($[m_{D^+} - 7\sigma_{D^+};\ m_{D^+} - 5\sigma_{D^+}]$ and $[m_{D^+} + 5\sigma_{D^+};\ m_{D^+} + 7\sigma_{D^+}]$) could be not representative of the background in the signal region.

We define an alternative SB as the regions $[m_{D^+} - 5\sigma_{D^+};\ m_{D^+} - 3\sigma_{D^+}]$ and $[m_{D^+} + 3\sigma_{D^+};\ m_{D^+} + 5\sigma_{D^+}]$. The new distributions for the χ^2_{red} is shown in Figure 4.7(b).

The disagreement still persists. We conclude that the discrepancy could be originated by a mismodeling of the tail in the MC. Such discrepancy shall be taken into account as a systematic uncertainty.

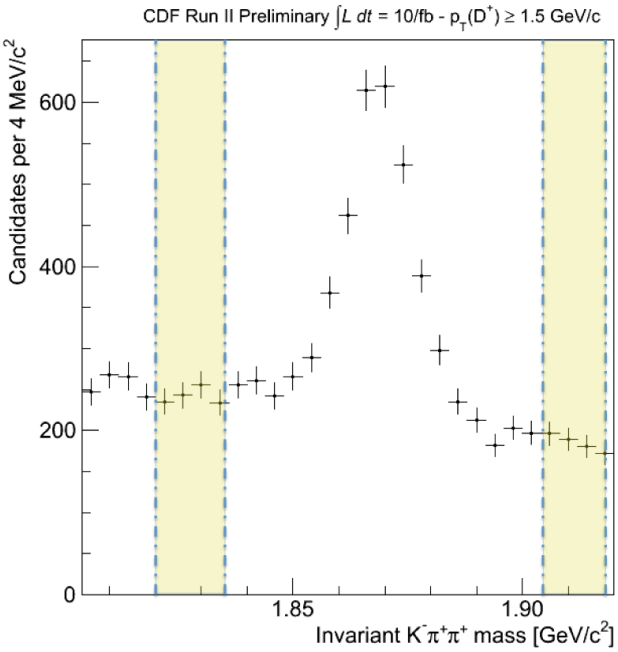

Figure 4.6: *Invariant $K^-\pi^+\pi^+$ mass distribution for the $p_T(D^+)$-integrated sample: the colored regions represent the SB.*

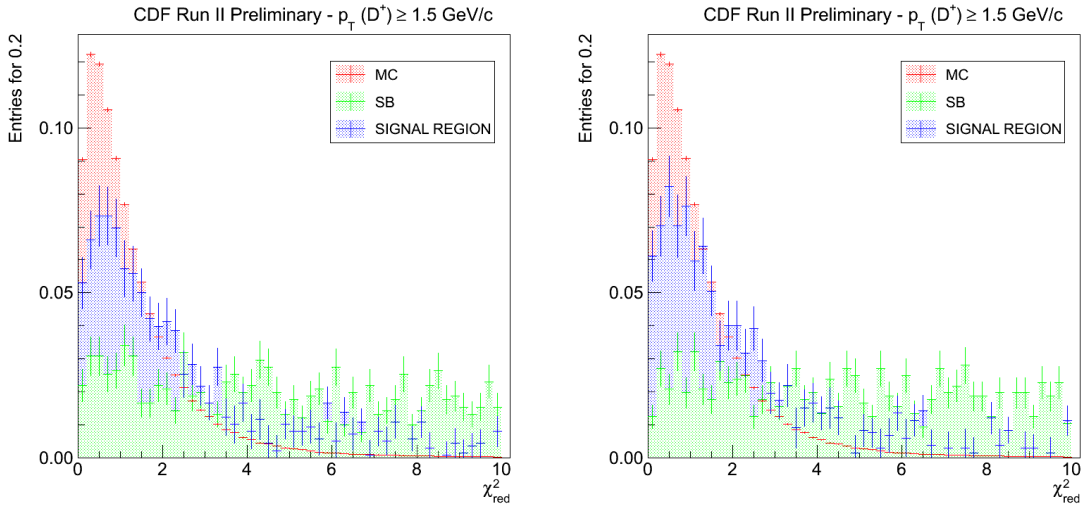

(a) (b)

Figure 4.7: *Distribution of χ^2_{red} in the signal region after applying the background subtraction (blue), in the side bands (SB) samples (green) and in the signal region only for the MC sample (red). We test different SB prototypes: (a) SB: $[m_{D^+} - 7\sigma_{D^+};\ m_{D^+} - 5\sigma_{D^+}]$ and $[m_{D^+} + 5\sigma_{D^+};\ m_{D^+} + 7\sigma_{D^+}]$; (b) SB: $[m_{D^+} - 5\sigma_{D^+};\ m_{D^+} - 3\sigma_{D^+}]$ and $[m_{D^+} + 3\sigma_{D^+};\ m_{D^+} + 5\sigma_{D^+}]$. The whole data sample is used.*

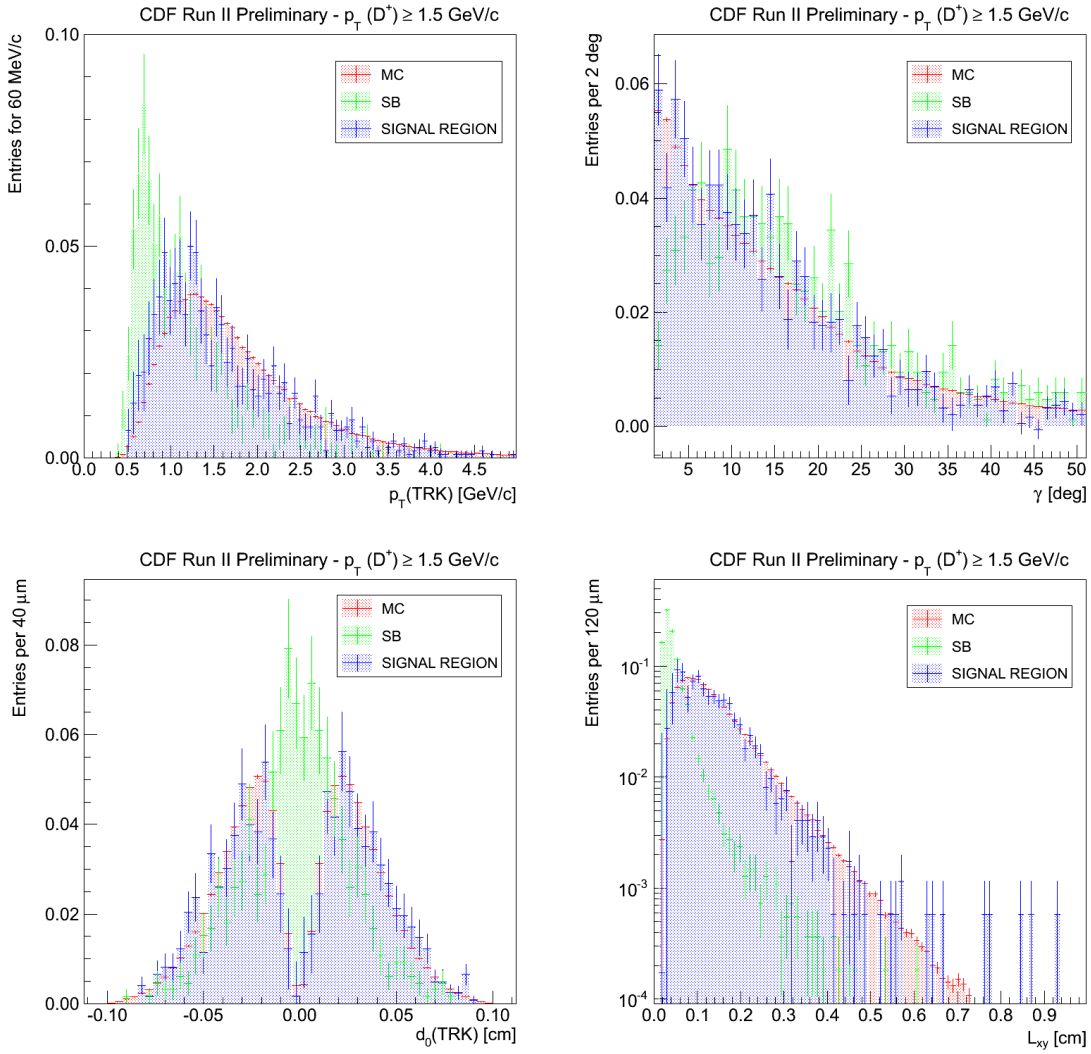

Figure 4.8: *Distribution of $p_T(TRK)$, γ, $d_0(TRK)$ and L_{xy} in the signal region after applying the background subtraction (blue), in the side bands (SB) samples (green) and in the signal region only for the MC sample (red). The whole data sample is used.*

Chapter 5

Yields as a function of $p_T(D^+)$

In this chapter we measure the signal yield obtained after applying the strategy described in the previous chapters, as a function of $p_T(D^+)$. First, we describe the parametrization for the background shapes; then we introduce the fitting procedure used and finally, the differential yields.

5.1 Combinatorial background

In the mass window we use for the fit, [1.6; 2.0] GeV/c^2, the background is due only to combinatorial (fake) candidates: when three unrelated tracks accidentally satisfy our selection requirements on candidates, they generate a fake candidate. In this case, MC doesn't help because it doesn't simulate the whole event, but only the signal. From the MC simulation of the signal we know that the signal appears in the invariant $K^-\pi^+\pi^+$ mass plot as a narrow peak with an average width of about 7 MeV/c^2.
We can use the other two regions at lower and higher mass to model the shape of the combinatorial background: $[m_{min};\ m_{D^+} - 5\sigma_{D^+}]$ and $[m_{D^+} + 5\sigma_{D^+};\ m_{max}]$, where m_{max} and m_{min} define the range of the fitting region; only background candidates are present in these regions.
A decreasing exponential shape is a good approximation of the trend we observe:

$$\wp_{\mathrm{Bkg}}(m;\vec{\theta}_{\mathrm{Bkg}}) = \frac{t}{e^{-t\cdot m_{min}} - e^{-t\cdot m_{max}}} e^{-t\cdot m} \tag{5.1}$$

where $\vec{\theta}_{\mathrm{Bkg}}$ is the vector of background parameters. It is defined as $\vec{\theta}_{\mathrm{Bkg}} = \{\mathrm{t}\}$, where t is the slope of the exponential. It is extracted by fitting the simulated invariant $K^-\pi^+\pi^+$ mass for combinatorics only. Figure 5.1 shows an example of the result of this parameterization in the interval $p_T(D^+) \in [2.5; 3.5]\ GeV/c$.

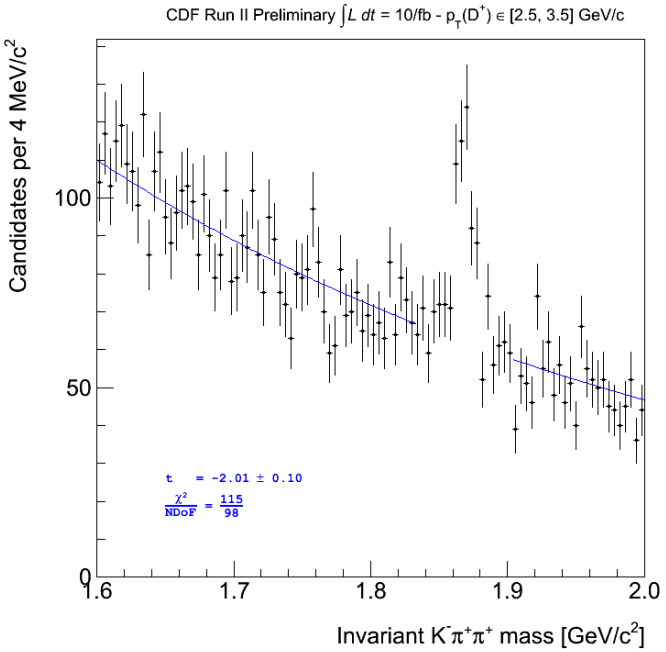

Figure 5.1: *Invariant $K^-\pi^+\pi^+$ mass fit of data in the interval $p_T(D^+) \in [2.5; 3.5]$ GeV/c for the backgorund only, in the regions comprised in $[m_{min};\ m_{D^+} - 5\sigma_{D^+}]$ and $[m_{D^+} + 5\sigma_{D^+};\ m_{max}]$.*

5.2 Fitting procedure

In order to find the D^+ yield, we perform a binned maximum likelihood fit of the invariant $K^-\pi^+\pi^+$ mass (m) distribution on data. We prefer the maximum likelihood method rather the least squares fitting because the former one has the advantage of treating correctly the empty bins used in the fitting procedure.

In binned cases, the shape model is compared, depending on the parameters vector, $\mathbf{p}$, with a binned histogram. The probability density function of data, $f(m, \mathbf{p})$, is approximated by the bin contents of the histogram normalized to unity. The number of events in each bin follows the multinomial distribution. Name O_k the observed count in *k-th* bin of width Δk.
Let E_k be the expected value of count in that *k-th* bin, then $E_k(\mathbf{p}) = \int_{\Delta k} f(m, \mathbf{p}) dm$. Thus, the likelihood function results:

$$\mathscr{L}(\mathbf{p}) = \frac{O_{tot}!}{O_1! \dots O_N!} \left(\frac{E_1}{O_{tot}}\right)^{O_1} \dots \left(\frac{E_N}{O_{tot}}\right)^{O_N} \tag{5.2}$$

where $\sum_{k=1}^{N} O_k = O_{tot}$ is the total entries number of the histogram.

The quantity to minimize is:

$$\mathscr{F}(\mathbf{p}) = -ln\mathscr{L}(\mathbf{p}) = -lnO_{tot}! - \sum_{k=1}^{N} lnO_k! - O_{tot}\, lnO_{tot} + \sum_{k=1}^{N} O_k\, lnE_k(\mathbf{p}) \tag{5.3}$$

The only term which depends on $\mathbf{p}$ is the last one, so the minimization is done ignoring all the other terms.
For us, the parameters vector is $\mathbf{p} = \{n_S, n_B, t\}$, where n_S and n_B are the signal and background yields respectively; while t is the slope of the exponential used for modeling the combinatorics. In fact, the fit function is defined as follows:

$$f(m;\mathbf{p}) = n_S \cdot \wp_{\mathrm{Sgl}}(m) + n_B \cdot \wp_{\mathrm{Bkg}}(m;t) \tag{5.4}$$

where $\wp_{\mathrm{Sgl}}(m)$ and $\wp_{\mathrm{Bkg}}(m;t)$ are the probability density functions of signals and background, defined and described in Sec. 4.2 and Sec. 5.1.

5.3 D^+ yields

We consider the optimized selection for each $p_T(D^+)$ bin and, following the fitting procedure described, we perform a fit to extract the D^+ yield. The fit of the raw yields is performed under the following assumptions:

- the signal shape is taken and fixed for each $p_T(D^+)$ bin from MC simulation, as described in Section 4.2. The parametrization used is p_T independent;
- the combinatorial background is assumed to be modeled by a decreasing exponential, as described in Section 5.1;
- the normalization of the signal and the background pdfs are two of the free parameters of the fit; the first one represent the raw yield of the signal;
- assuming the C-invariance of the strong interaction production, the number of D^+ candidates is equal to that of D^- candidates. The extracted signal yield is the sum of the two contributions.

Figures from 5.2 to 5.5 show the results of the fits on data bin by bin and in Table 5.1 we summarize the results. Finally, the resulting yields are visually shown in Figure 5.6, in linear and logarithmic scale.

Using a $p_T(D^+)$-differential optimization strategy rather than a $p_T(D^+)$-integrated optimization strategy, we increase the number of candidates for each bin of $p_T(D^+)$. This is extremely evident in the first and last bin studied in this analysis, as shown in Figure 5.7. The fit in Figure 5.7(a) has to be compared to the one developed using the selection for that specific bin (first plot in Figure 5.2), while the fit in Figure 5.7(b) has to be compared with the second plot in Figure 5.5. The optimized selection evaluated for the $p_T(D^+)$-integrated sample, is not the best one for situations of low statistics, as the last bin, or for cases where the background is predominant, as the first bin.

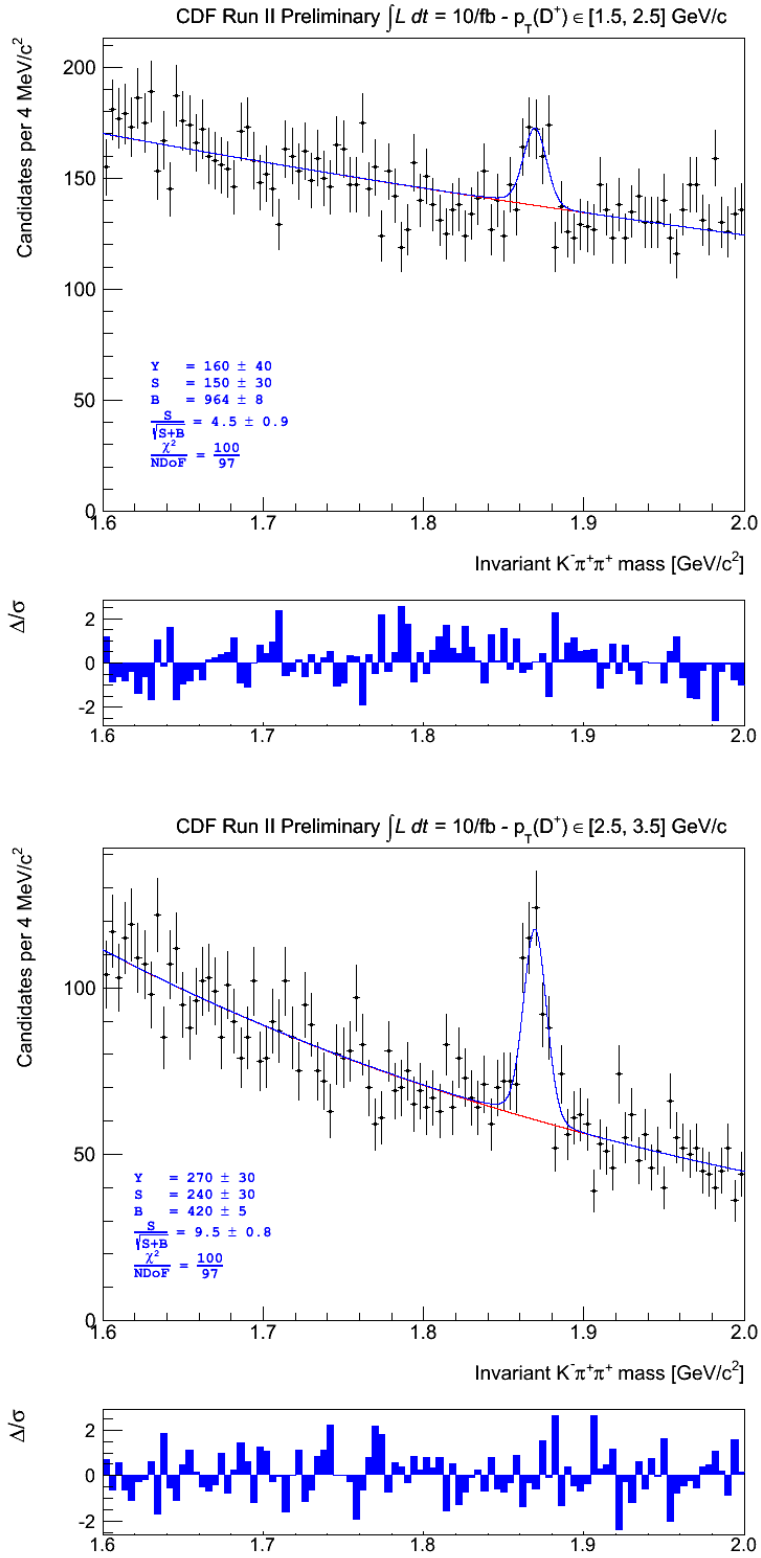

Figure 5.2: *Invariant $K^-\pi^+\pi^+$ mass fit on data in 1 GeV/c intervals of $p_T(D^+)$. Fit residuals are also shown. The blue line represents the result of the fit, while the combinatorial background contribution is shown by the red line.*

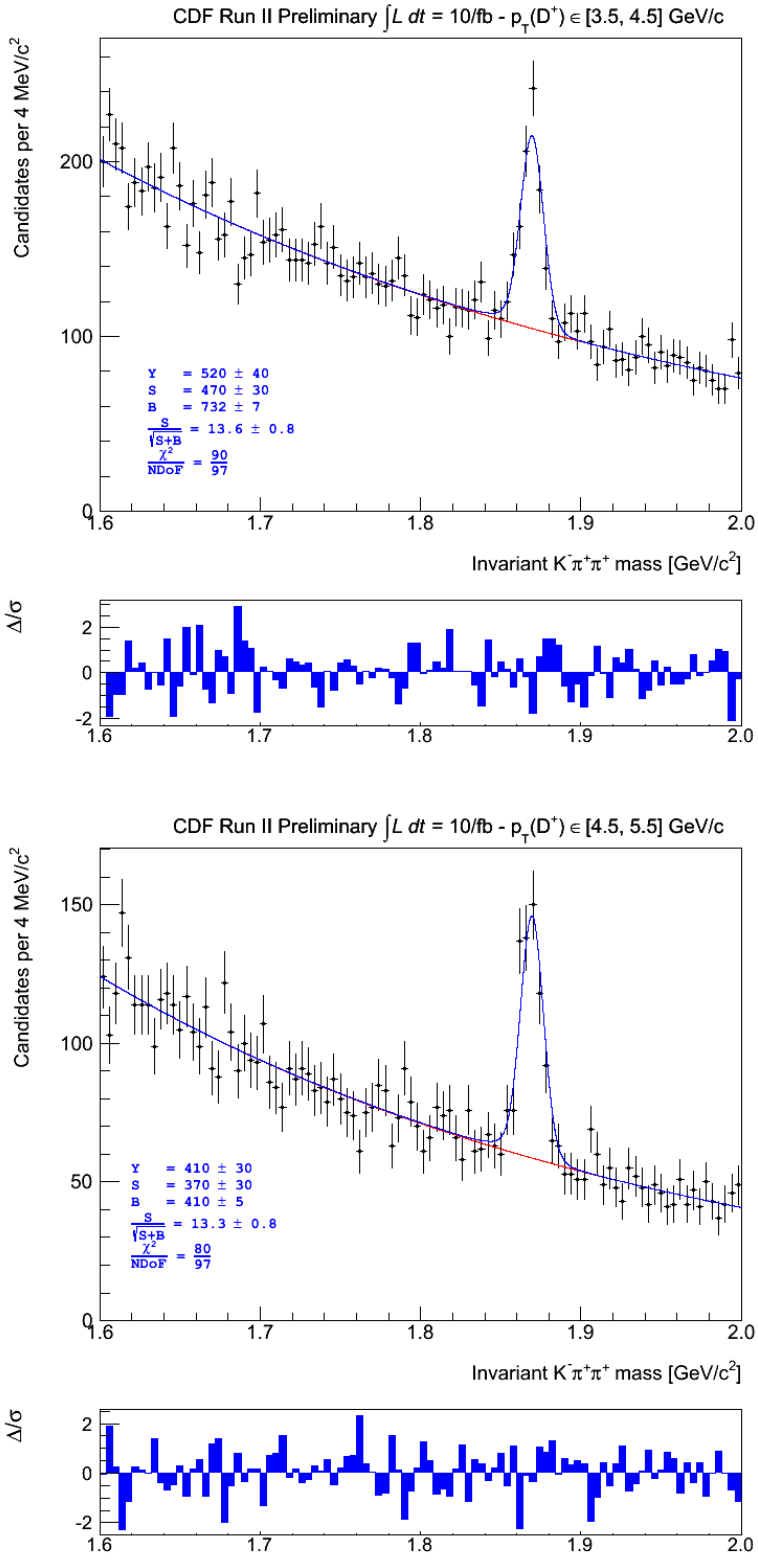

Figure 5.3: *Invariant $K^-\pi^+\pi^+$ mass fit on data in 1 GeV/c intervals of $p_T(D^+)$. Fit residuals are also shown. The blue line represents the result of the fit, while the combinatorial background contribution is shown by the red line.*

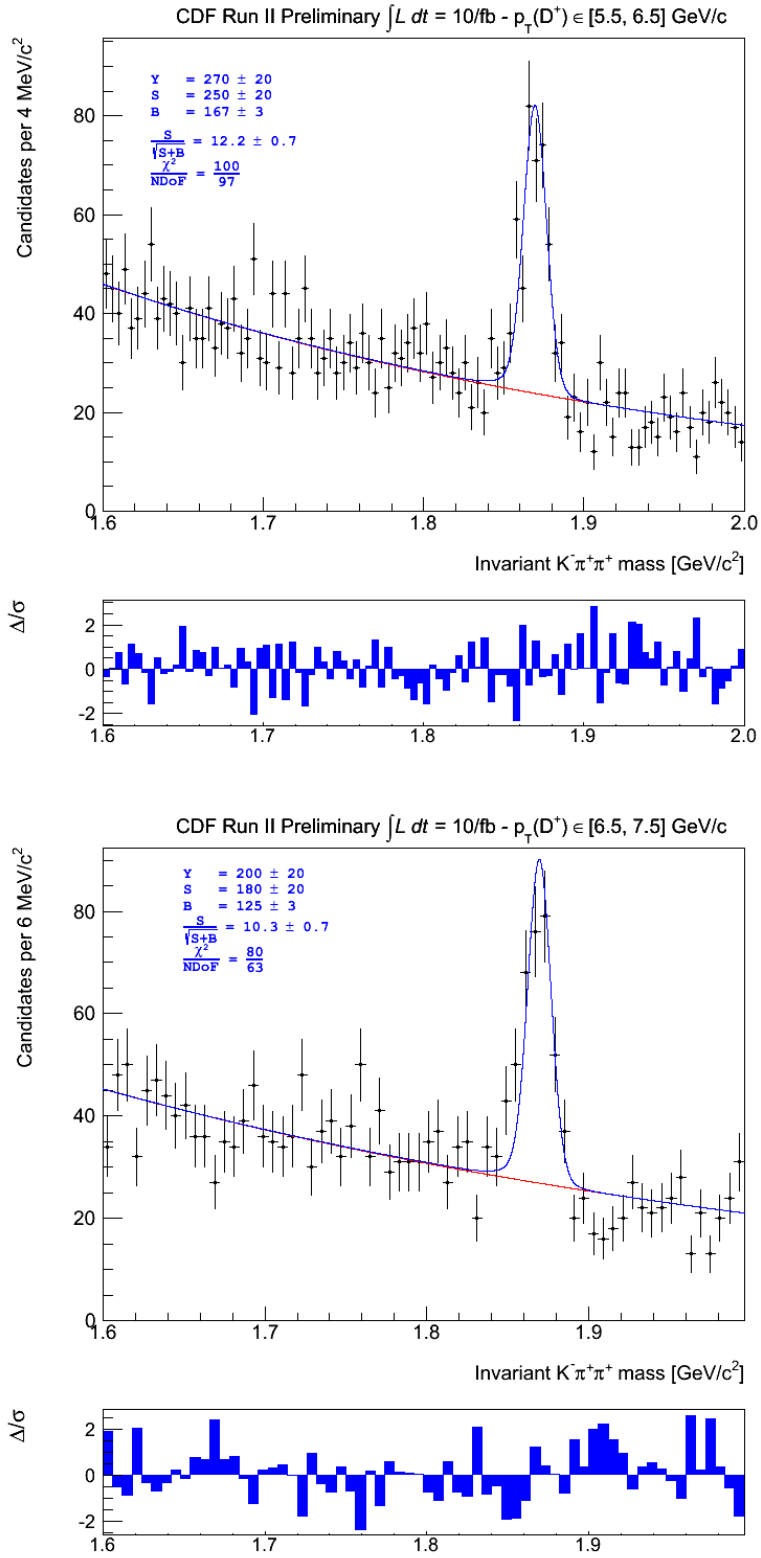

Figure 5.4: *Invariant $K^-\pi^+\pi^+$ mass fit on data in 1 GeV/c intervals of $p_T(D^+)$. Fit residuals are also shown. The blue line represents the result of the fit, while the combinatorial background contribution is shown by the red line.*

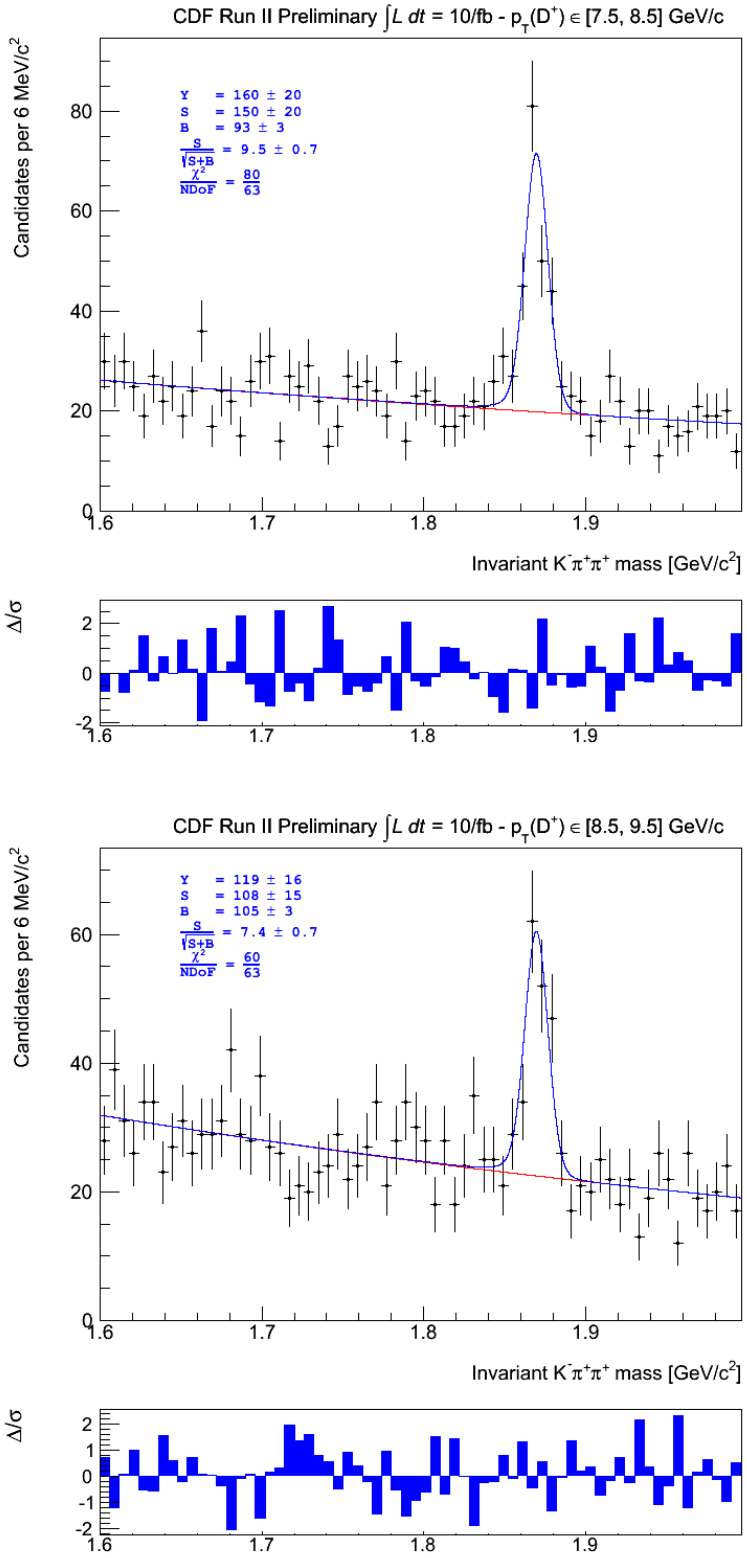

Figure 5.5: *Invariant $K^-\pi^+\pi^+$ mass fit on data in 1 GeV/c intervals of $p_T(D^+)$. Fit residuals are also shown. The blue line represents the result of the fit, while the combinatorial background contribution is shown by the red line.*

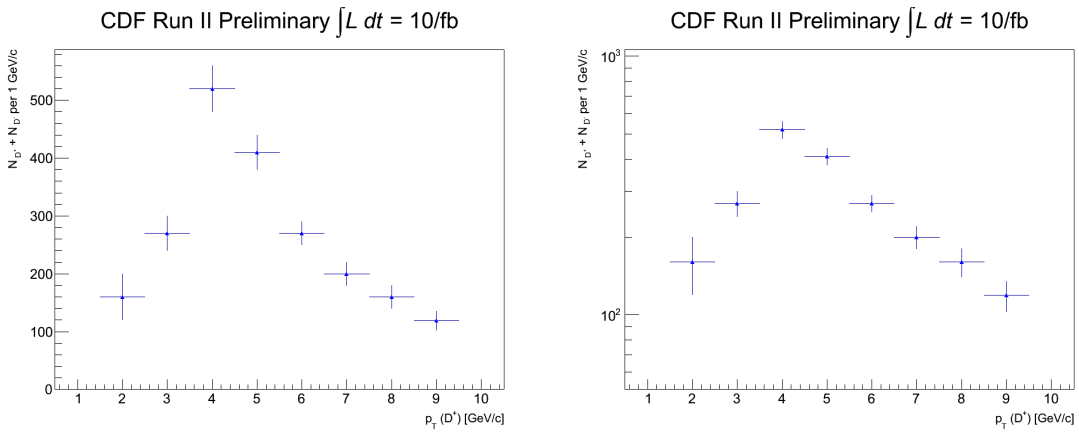

Figure 5.6: *Signal yields ($N_{D^+} + N_{D^-}$) as a function of $p_T(D^+)$, in linear and logarithmic scale.*

p_T [GeV/c]	$N_{D^+} + N_{D^-}$	$\frac{S}{\sqrt{S+B}}$
1.5 – 2.5	160 ± 40	4.5 ± 0.9
2.5 – 3.5	270 ± 30	9.5 ± 0.8
3.5 – 4.5	520 ± 40	13.6 ± 0.8
4.5 – 5.5	410 ± 30	13.3 ± 0.8
5.5 – 6.5	270 ± 20	12.2 ± 0.7
6.5 – 7.5	200 ± 20	10.3 ± 0.7
7.5 – 8.5	160 ± 20	9.5 ± 0.7
8.5 – 9.5	119 ± 16	7.4 ± 0.7

Table 5.1: *Results of the signal yield.*

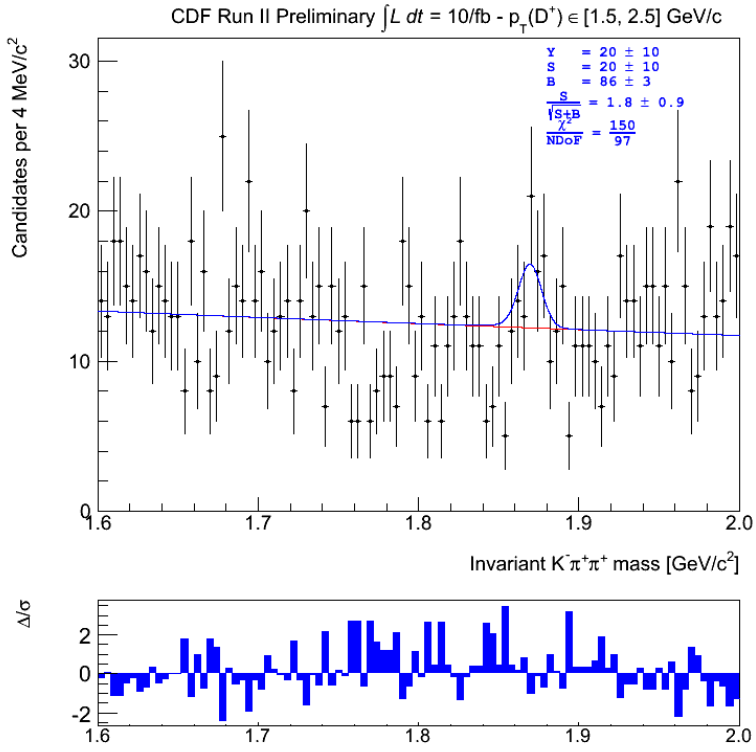

(a)

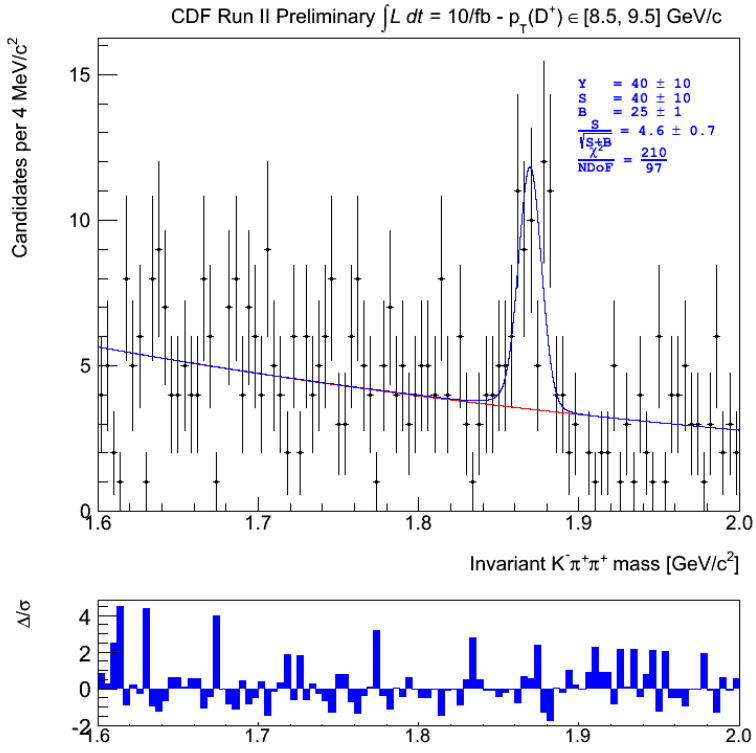

(b)

Figure 5.7: *Invariant* $K^-\pi^+\pi^+$ *mass fit on data in the interval* $p_T(D^+) \in [1.5;\ 2.5]\,GeV/c$ *(a) and in the interval* $p_T(D^+) \in [8.5;\ 9.5]\,GeV/c$ *(b), selected using the* $p_T(D^+)$*-integrated optimization.*

Chapter 6

Efficiencies

In this chapter we discuss the method to assess the efficiencies and acceptances of this analysis. The data taking process and the procedure described in the previous chapters let us to observe only a fraction of the total number of D^+ mesons produced in the $p\bar{p}$ collisions. We want to assess the lost fraction in order to correct the measured yields.

6.1 Global efficiency

The D^+ global efficiency, $\varepsilon(D^+)$, can be defined as the probability a D+ has to pass the trigger, the reconstruction and the offline selection criteria. We estimate the $\varepsilon(D^+)$ in a limited η region only:

$$\varepsilon(D^+) = \left. \frac{N_{candidates}(p_T)\ passing\ the\ Trig\ \&\ Rec}{N_{generated}(p_T)} \right|_{|y|\leq 1} \tag{6.1}$$

It is possible to factorize the efficiency into two main contributions: trigger, ε_{trig}, and reconstruction, ε_{rec}:

$$\varepsilon(D^+) = \varepsilon_{trig} \cdot \varepsilon_{rec}(p_T) \Big|_{|y|\leq 1} \tag{6.2}$$

6.1.1 Trigger efficiency

The term ε_{trig} represents the correction for any inefficiency due to the online data acquisition process and the trigger selection. Each trigger has its own efficiency:

ε_{ZB} and ε_{MB}.

6.1.1.1 ZB

The ZB trigger is synchronized with the Tevatron's bunch crossing frequency: it doesn't require a start signal from any CDF subdetectors (see Sec. 3.2.1). For this reason, only the dead time through the three-level trigger chain could compromise the ZB efficiency, but this is taken into account when computing the luminosity. In such a way, the ZB trigger is 100% efficient ($\varepsilon_{ZB} = 1$).

6.1.1.2 MB

On the contrary of the ZB, the MB trigger efficiency is strongly dependent on beam conditions and event topology (see Sec. 3.2.2). After studying many event variables [36] [37] [38], it has been observed that it is mainly related to three quantities:

- the instantaneous luminosity, L_{inst};
- the number of tracks in the event;
- the number of reconstructed primary vertices.

The quantities listed are closely related: increasing the luminosity, the number of interactions grows up, as well as the reconstructed primary vertices. Also the number of charged tracks increases and hence, the probability of a coincidence in both East and West CLCs: the efficiency rises as a function of these variables.

Being $\varepsilon_{ZB} = 1$, we can use the ZB data sample to evaluate ε_{MB}. In fact, each CDF event is labeled according to the trigger status of all the active triggers: we can easily check if a particular ZB event has also been triggered by the MINBIAS trigger. Then, the number of D^+ candidates found in the ZB events with the MB trigger fired ($Y_{ZB\cap MB}$) over the number of D^+ candidates found in the total ZB events (Y_{ZB}) represents the MB trigger efficiency for events with a D^+ candidate:

$$\varepsilon_{MB}(D^+) = \frac{Y_{ZB\cap MB}}{Y_{ZB}} \tag{6.3}$$

We perform a combined fit of the invariant $K^-\pi^+\pi^+$ mass distribution for ZB events that fired or not the MB trigger, $ZB\cap MB$ and $\overline{ZB \cap MB}$ subsets respectively. We perform the fit using the same function used for the other invariant $K^-\pi^+\pi^+$ mass plots (see equation 5.4), but setting the slope of the exponential function used for the background as a common parameter. We extract the yield from the fit. The result of the combined fit is shown in Figure 6.1.

The MB trigger efficiency for the D^+ is: $\varepsilon_{MB}(D^+) = 0.994 \pm 0.004$. This correction has negligible dependence on the candidates transverse momentum, with

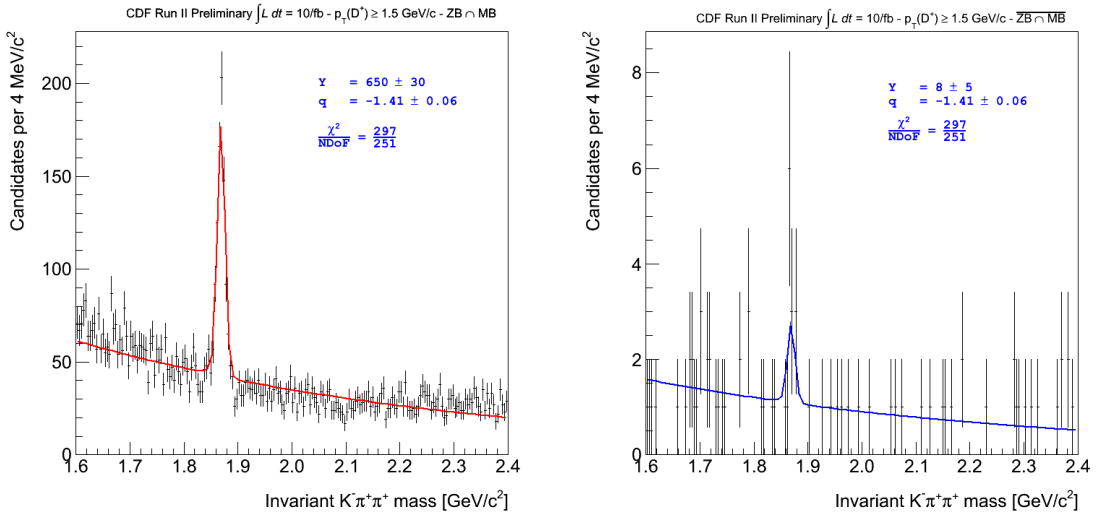

(a) $Y_{ZB \cap MB}$ (b) $Y_{\overline{ZB \cap MB}}$

Figure 6.1: *Invariant $K^-\pi^+\pi^+$ mass combined fit of data for the ZB events that fired or not the MB trigger, $ZB \cap MB$ (a) and $\overline{ZB \cap MB}$ (b) subsets respectively .*

fluctuations around 1 ‰. The MB subsample is about the 40% of the total sample, so the final effect is at about 1.6‰ level; considering the statistical uncertainties on the yields measurements (~ 10%), the effect of this correction is completely negligible on the cross section measurement. This means that the two subsamples can be safely added; we consider this small correction as a systematic error.

6.1.2 Reconstruction

The term ε_{rec} defines a global reconstruction efficiency for our candidates; it takes into accounts different corrections:

1. detector response to the passage of particles;
2. tracking efficiency;
3. efficiency and acceptance due to our selection of the candidates.

We use the BMC sample discussed in Sec. 4.1.1. MC events are distributed across the data-taking periods in proportions that approximate the integrated lunimosity collected in each period. We count the BMC fraction of D^+ and D^- which pass the selection with respect to the total number of generated candidates in $|y| \leq 1$. In Figure 6.2 we show the general trend and the results obtained, bin by bin, are summarized in Table 6.1.

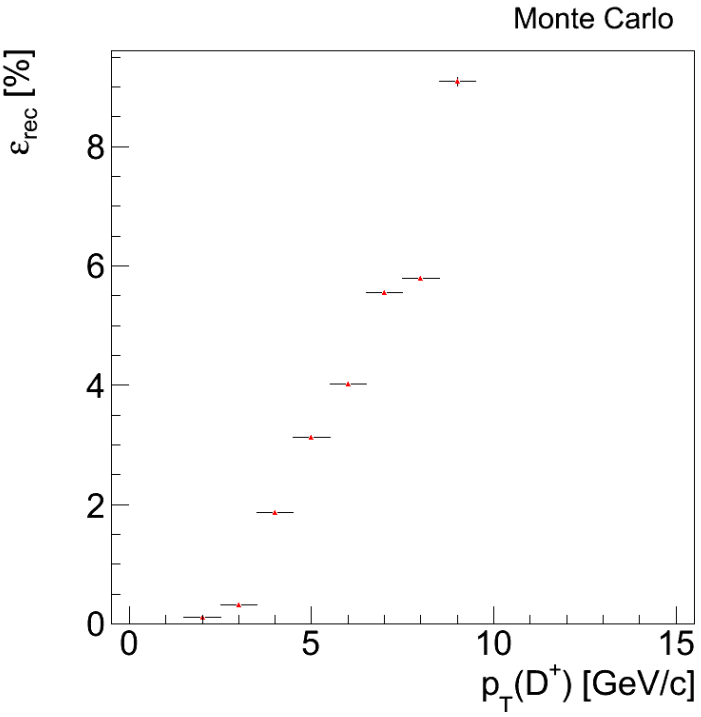

Figure 6.2: *Reconstruction efficiency as a function of* $p_T(D^+)$.

p_T [GeV/c]	ε_{rec} [%]
1.5 – 2.5	0.1044 ± 0.0010
2.5 – 3.5	0.3149 ± 0.0021
3.5 – 4.5	1.872 ± 0.007
4.5 – 5.5	3.133 ± 0.012
5.5 – 6.5	4.018 ± 0.019
6.5 – 7.5	5.56 ± 0.03
7.5 – 8.5	5.79 ± 0.04
8.5 – 9.5	9.09 ± 0.06

Table 6.1: *Reconstruction efficiency as a function of* $p_T(D^+)$.

6.2 Reliability of the MC samples

As discussed in Sec. 4.3 the MC simulation for the χ^2_{red} is not perfectly representative of the data. In this section we try to quantify the discrepancy between simulations and data for each variable.

Consider a sample of data, made up by two sources in different proportions. If we analyse that sample looking at different variables, but with the same selection,

we expect to determine the same ratio of the two sources.

The problem of the evaluation of different sources in a sample of data is quite common in high energy physics. Often there is no analytic form available for the distributions of these sources, but only sample generated by MC simulation or subsamples of data. In our case we have a sample of data, to which we refer as signal region, and two different sources, MC for the signal only and SB for the background only. We wish to determine their proportions in the signal region, P_B and P_S.

Let's name d_i the number of events in the data that fall into bin i (we are assuming n bins). Let a_{iS} and a_{iB} be the counts into bin i for the MC and SB respectively. The probability for observing a particular d_i is given by the Poisson distribution. Then f_i, the predicted number of events for real data in the same bin, is given by:

$$f_i = N_D \cdot \left(\frac{P_B \cdot a_{iB}}{N_B} + \frac{P_S \cdot a_{iS}}{N_S} \right) \tag{6.4}$$

where N_D is the total number in the data sample, N_S and N_B are the total number in the MC and SB samples:

$$N_D = \sum_{i=1}^{n} d_i, \quad N_S = \sum_{i=1}^{n} a_{iS}, \quad N_B = \sum_{i=1}^{n} a_{iB} \tag{6.5}$$

It is convenient to incorporate these normalization factors into the proportion factors, writing $p_S = N_D \cdot P_S/N_S$ and $p_B = N_D \cdot P_B/N_B$. In such a way the equation (6.4) becomes:

$$f_i = p_B \cdot a_{iB} + p_S \cdot a_{iS} \tag{6.6}$$

The sources used are of finite size and so they may fluctuate, leading to statistical fluctuations in the a_{iS} and a_{iB} respectively. Disagreements between a particular d_i and f_i arise fom incorrect p_B and p_S and from fluctuations in the a_{iS} and a_{iB}. Let's call the expected counts A_{iS} and A_{iB}

The distributions followed by the sources is in fact binomial, but can be approximated to a Poisson distribution if $A_{iS} << N_S$ and $A_{iB} << N_B$. Under this assumption, the equation (6.6) can be written as:

$$f_i = p_B \cdot A_{iB} + p_S \cdot A_{iS} \tag{6.7}$$

It is possible to find p_B, p_S, A_{iB} and A_{iS} maximizing the total likelihood which is the combined probability of the observed d_i, a_{iB} and a_{iS} :

$$ln\mathcal{L} = \sum_{i=1}^{n} d_i ln f_i - f_i + \sum_{i=1}^{n} a_{iB} - A_{iB} + \sum_{i=1}^{n} a_{iS} - A_{iS}, \tag{6.8}$$

To perform this maximization we use a tool of the ROOT package called TFractionFitter: it takes in account the fact that the MC statistics used are finite and thus subject to statistical fluctuations [40].

The study of the residuals $\frac{\Delta_B}{\sigma_{a_{i,B}}} = \frac{a_{iB}-A_{iB}}{\sigma_{a_{i,B}}}$, $\frac{\Delta_S}{\sigma_{a_{i,S}}} = \frac{a_{iS}-A_{iS}}{\sigma_{a_{i,S}}}$ can be helpful for understanding which templates are not consistent with the expected Poisson values and then, which variable is not helpful or mismodeled.

For the final cross section measurement, the most accurate variable is the invariant mass. In fact, it allows to estimate the smallest uncertainty for the cross section measurement. So, to check the other variables, we compare each one with the invariant mass. For instance, we observe L_{xy} cutting on all the variables, but L_{xy} itself. Considering the invariant mass plot, we fit S and B estimating $\frac{S}{\sqrt{S+B}}$. On the other hand, using the TFractionFitter [39] on the L_{xy} distribution, we extract signal, S, and background, B, and evaluate the same figure of merit $\frac{S}{\sqrt{S+B}}$.

The two results should be consistent within the errors.

Figures from 6.3 to 6.5 summarize the distributions for a_{ij} and A_{ij} ($j = S, B$) with the corrispondent residuals for each variable considered. It's evident the mismodeling of the MC on tails of the distributions. In fact, on the tails of the distributions the a_{iS} understimate the A_{iS}. Still, the residuals are quite small. On the contrary, by looking at the residuals it's evident the finite size of SB sample. Nevertheless, the residuals are within 2σ, except for the χ^2_{red} where a residual is null within 4σ. We can argue that no one of the studied variable is rejectable.

Figures from 6.6 to 6.10 synthesize the result of this check. On the (a) side of each figure, we show the result of the fit on the invariant mass plot; while, on the (b) side we plot the distributions of the variable on which we are not cutting, before (black markers) and after (red markers) the TFractionFitter. Then we comparte their figures of merit. In Table 6.2 the results obtained are summarized.

Variable	$\frac{S}{\sqrt{S+B}}$(m)	$\frac{S}{\sqrt{S+B}}$(TFF)	Δ/σ_Δ
$p_T(TRK)$	28.7±0.6	22.7±2.7	2.3
γ	35.4±0.6	34±3	0.5
$d_0(TRK)$	27.3±0.6	28.9± 2.0	0.8
χ^2_{red}	28.5±0.6	17.5±1.5	8
L_{xy}	24.6±0.7	22.7±1.2	1.9

Table 6.2: *Comparison of figure of merit obtained from the invariant mass plot and the TFractionFitter using the SB defined as* $[m_{D^+} - 7\sigma_{D^+},\ m_{D^+} - 5\sigma_{D^+}]$ *and* $[m_{D^+} + 5\sigma_{D^+},\ m_{D^+} + 7\sigma_{D^+}]$.

We don't consider the discrepancy for L_{xy} signifcant, while the discrepancy is significant for the variable $p_T(TRK)$ and highly significant for the variable χ^2_{red}. For the last variable we also verify an alternative SB prototype ($[m_{D^+}-5\sigma_{D^+},\ m_{D^+}-3\sigma_{D^+}]$ and $[m_{D^+}+3\sigma_{D^+},\ m_{D^+}+5\sigma_{D^+}]$). The new results is shown in Table 6.3; it is consistent within 1σ with the previous one.

These small dicrepancies suggest new ideas that there may be space for future improvements.

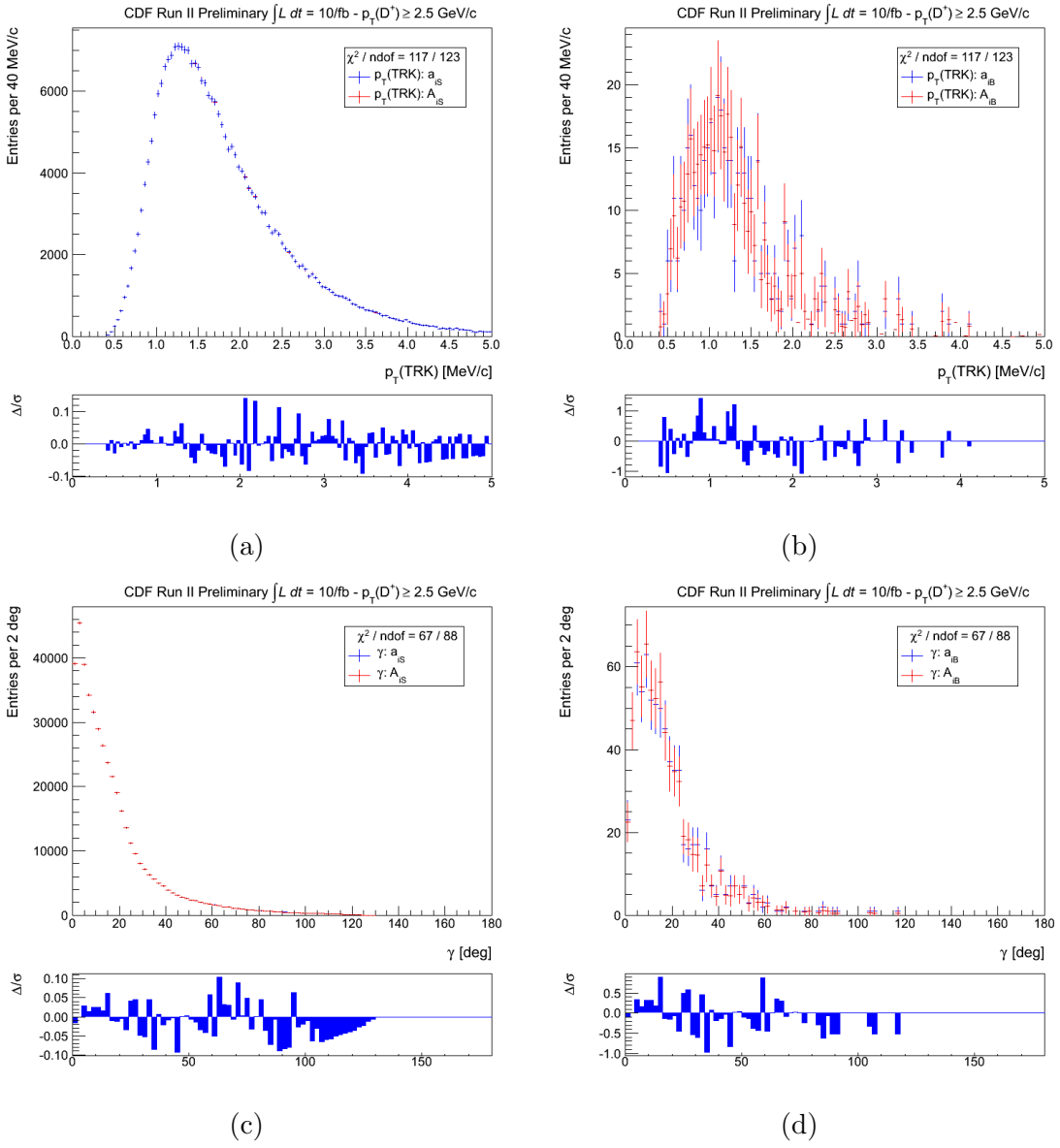

Figure 6.3: *Distribution of a_{iS} (blue markers) and A_{iS} (red markers) for the variable $p_T(TRK)$ (a) and γ (c); distribution of a_{iB} (blue markers) and A_{iB} (red markers) for the variables $p_T(TRK)$ (b) and γ (d). Fit residuals are also shown.*

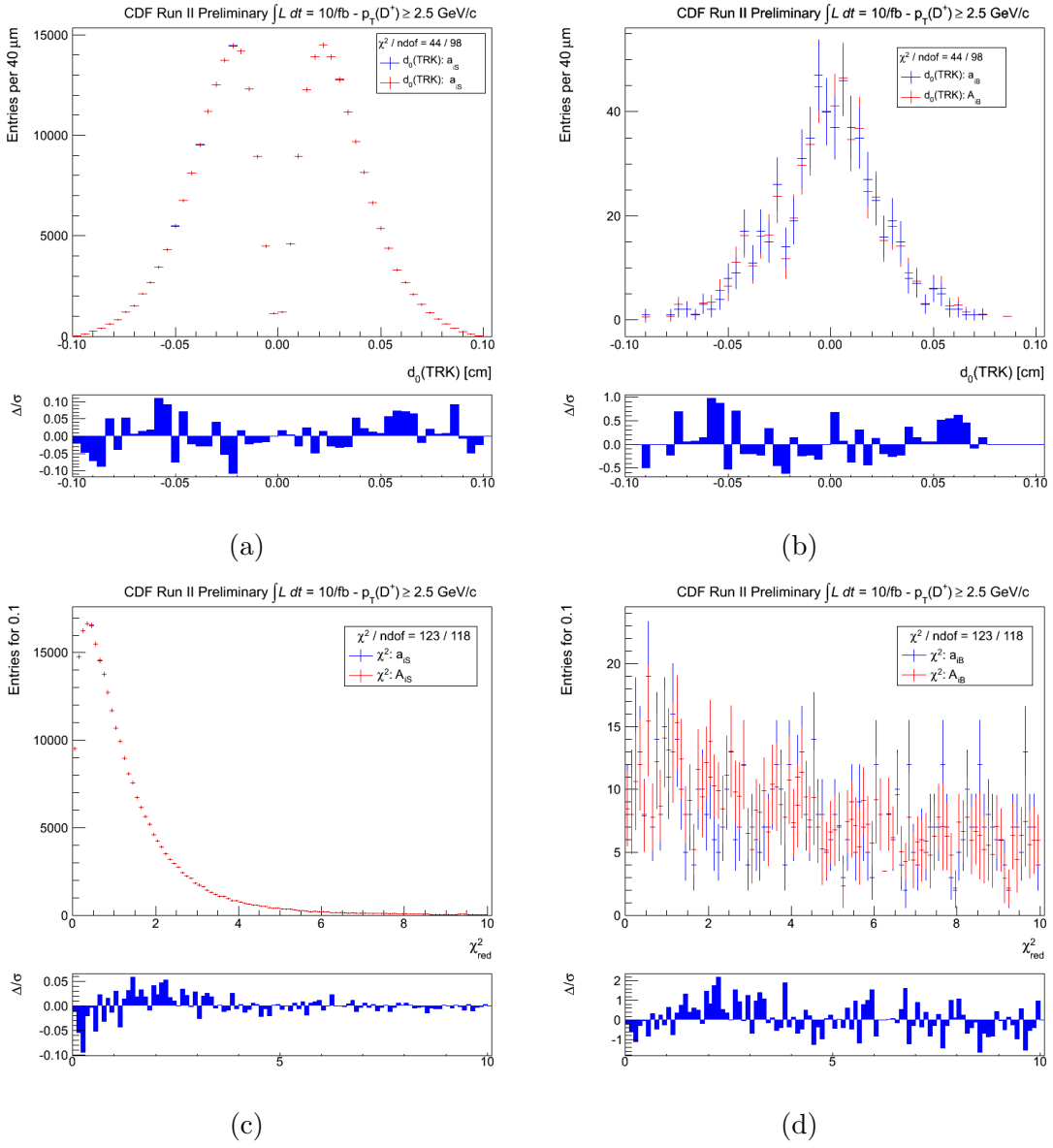

Figure 6.4: *Distribution of a_{iS} (blue markers) and A_{iS} (red markers) for the variable $d_0(TRK)$ (a) and χ^2_{red} (c); distribution of a_{iB} (blue markers) and A_{iB} (red markers) for the variables $d_0(TRK)$ (b) and χ^2_{red} (d). Fit residuals are also shown.*

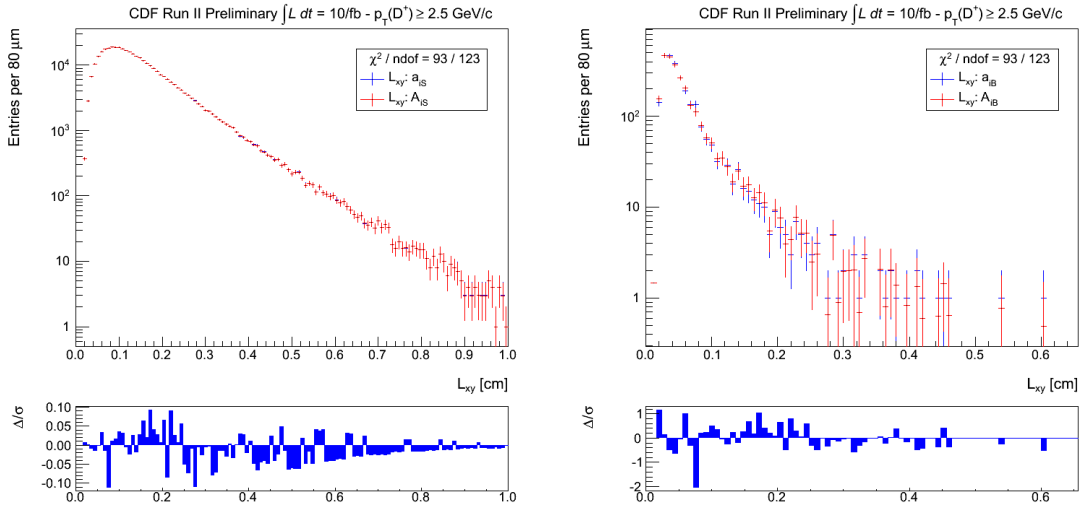

(a) (b)

Figure 6.5: *(a) Distribution of a_{iS} (blue markers) and A_{iS} (red markers) for the variable L_{xy}; (b) distribution of a_{iB} (blue markers) and A_{iB} (red markers) for the variable L_{xy}. Fit residuals are also shown.*

Variable	$\frac{S}{\sqrt{S+B}}$(m)	$\frac{S}{\sqrt{S+B}}$(TFF)	Δ/σ_Δ
χ^2_{red}	28.5±0.6	19.3± 1.4	7

Table 6.3: *Comparison of figure of merit obtained from the invariant mass plot and the TFractionFitter using a different prototype of SB ($[m_{D^+} - 5\sigma_{D^+},\ m_{D^+} - 3\sigma_{D^+}]$ and $[m_{D^+} + 3\sigma_{D^+},\ m_{D^+} + 5\sigma_{D^+}]$).*

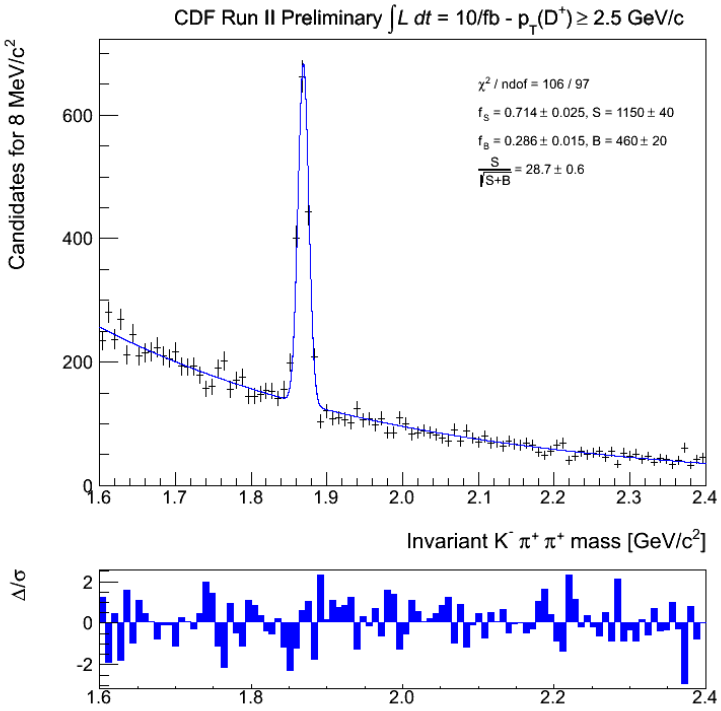

(a) Fit on the invariant $K^-\pi^+\pi^+$ mass.

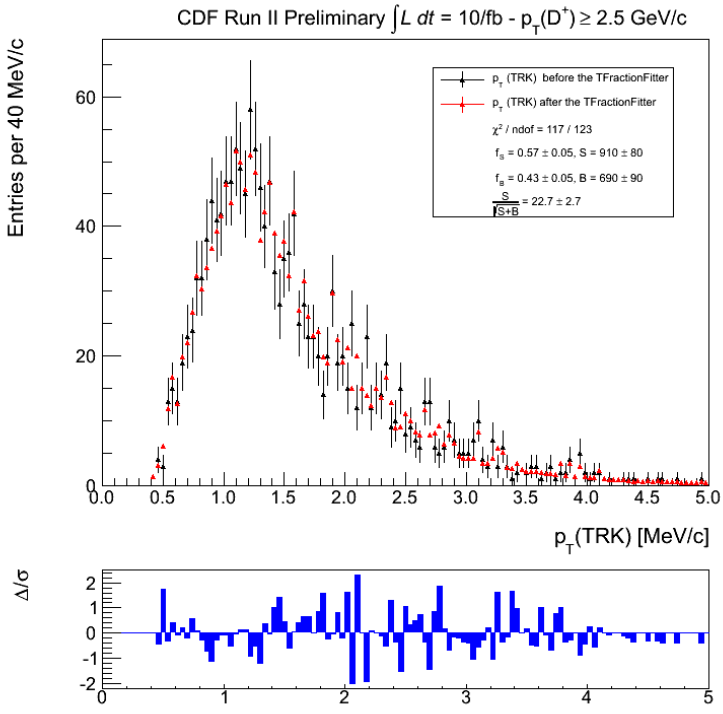

(b) TFractionFitter.

Figure 6.6: *(a) Result of the fit on the invariant $K^-\pi^+\pi^+$ mass plot when we don't cut on $p_T(TRK)$; (b) $p_T(TRK)$ before (black markers) and after (red markers) the TFractionFitter. Fit residuals are also shown.*

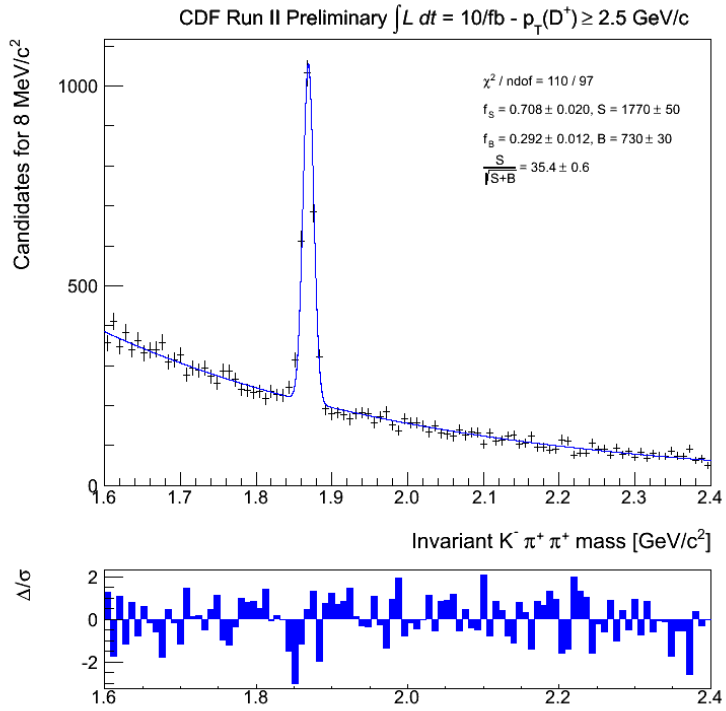

(a) Fit on the invariant $K^-\pi^+\pi^+$ mass.

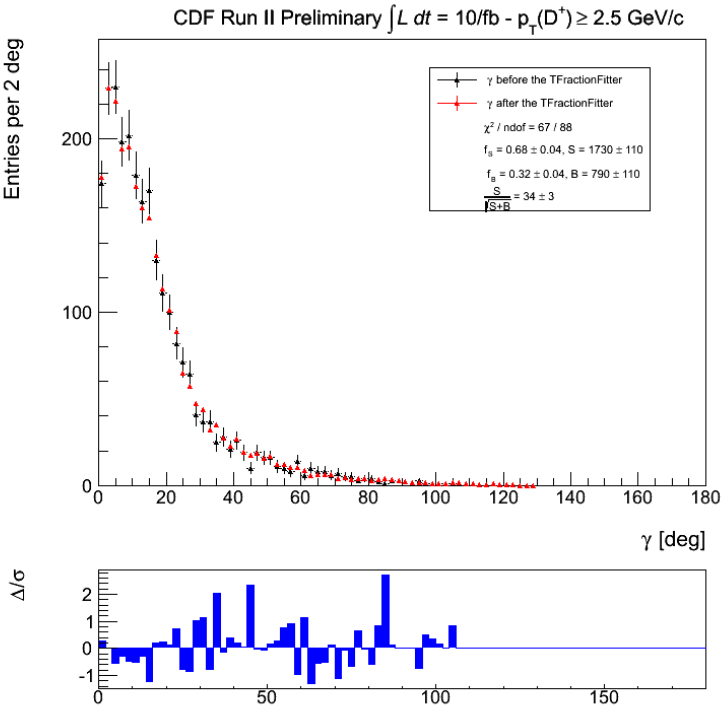

(b) TFractionFitter.

Figure 6.7: *(a) Result of the fit on the invariant $K^-\pi^+\pi^+$ mass plot when we don't cut on γ; (b) γ before (black markers) and after (red markers) the TFractionFitter. Fit residuals are also shown.*

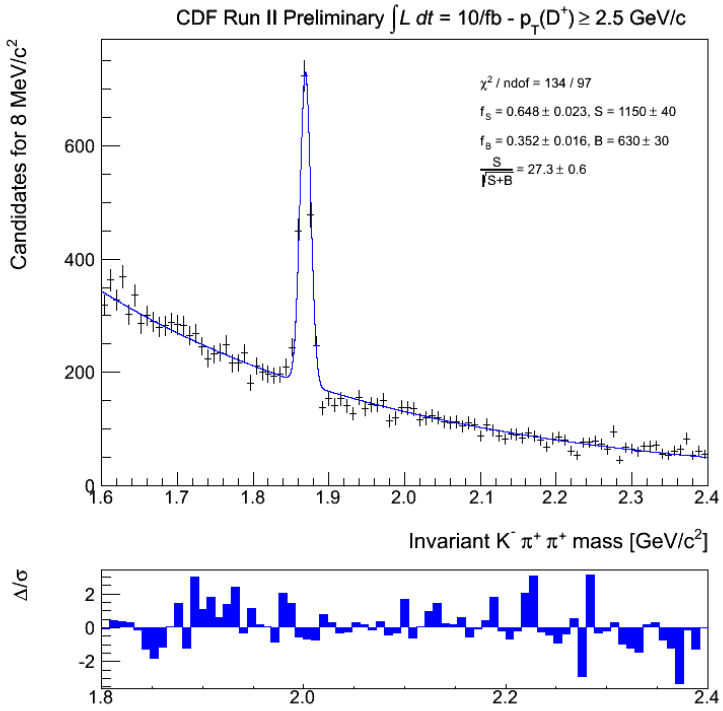

(a) Fit on the invariant $K^-\pi^+\pi^+$ mass.

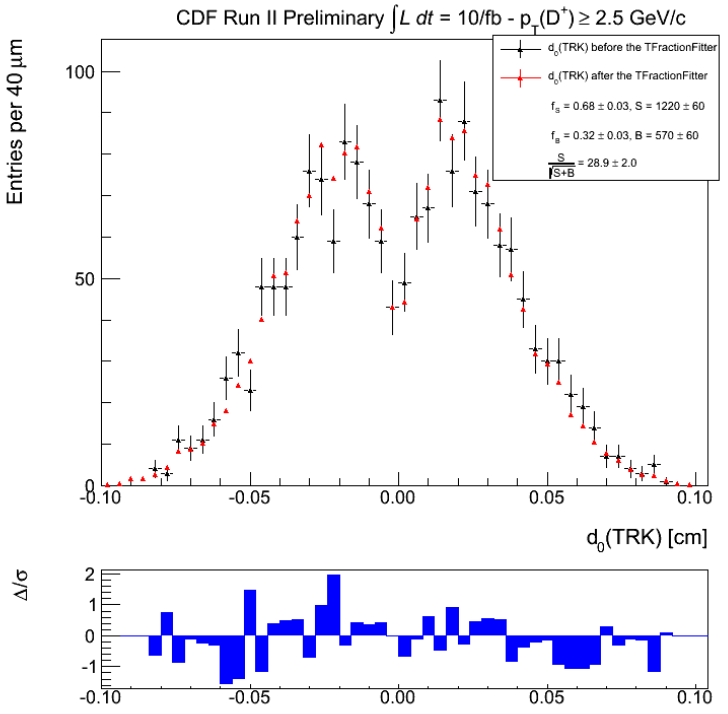

(b) TFractionFitter.

Figure 6.8: *(a) Result of the fit on the invariant $K^-\pi^+\pi^+$ mass plot when we don't cut on $d_0(TRK)$; (b) $d_0(TRK)$ before (black markers) and after (red markers) the TFractionFitter. Fit residuals are also shown.*

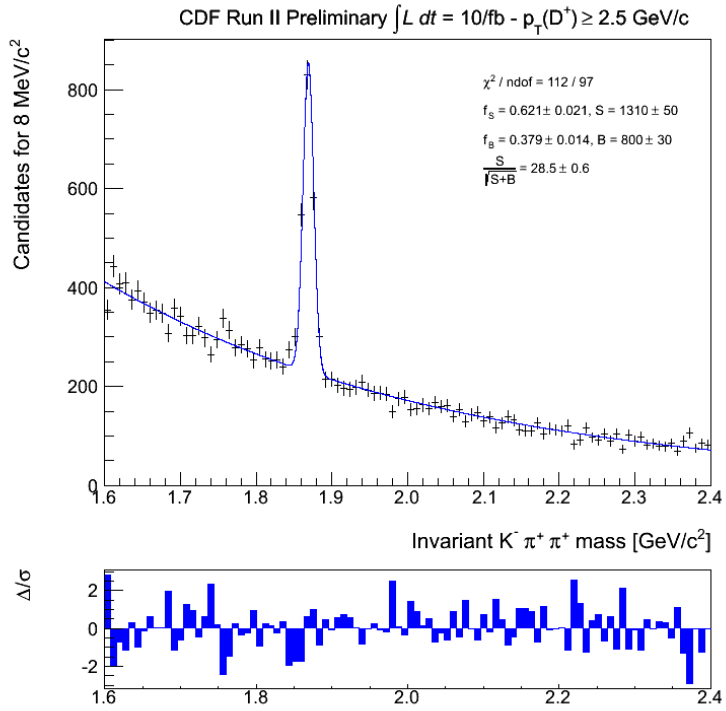

(a) Fit on the invariant $K^-\pi^+\pi^+$ mass.

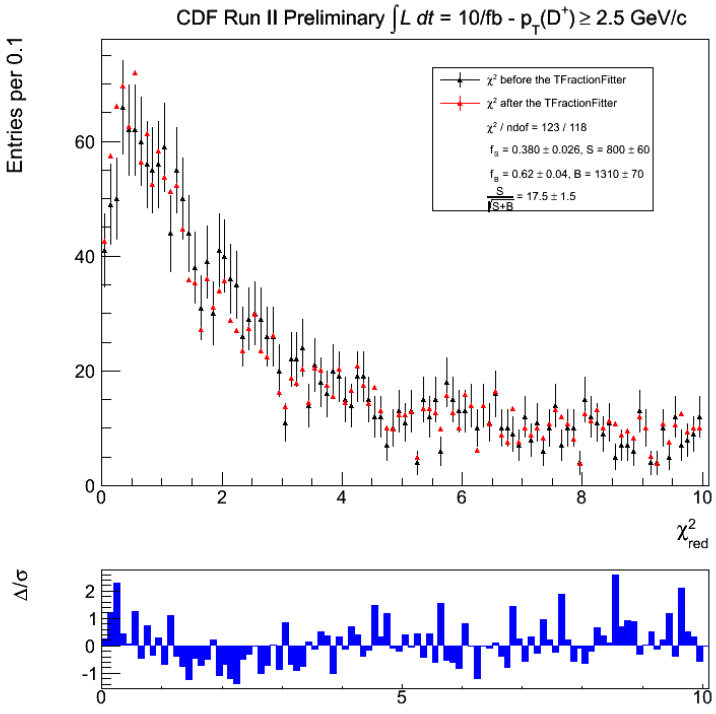

(b) TFractionFitter.

Figure 6.9: *(a) Result of the fit on the invariant $K^-\pi^+\pi^+$ mass plot when we don't cut on χ^2_{red}; (b) χ^2_{red} before (black markers) and after (red markers) the TFractionFitter. Fit residuals are also shown.*

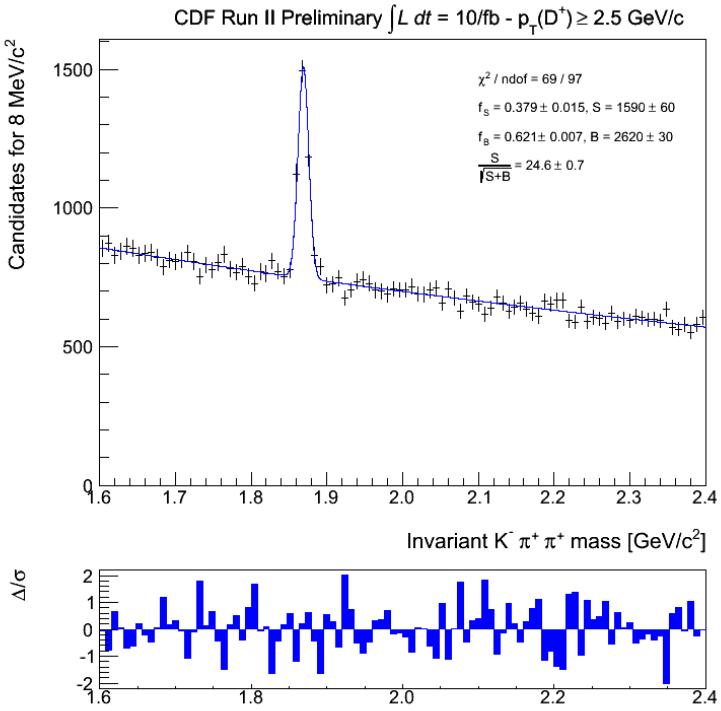

(a) Fit on the invariant $K^-\pi^+\pi^+$ mass.

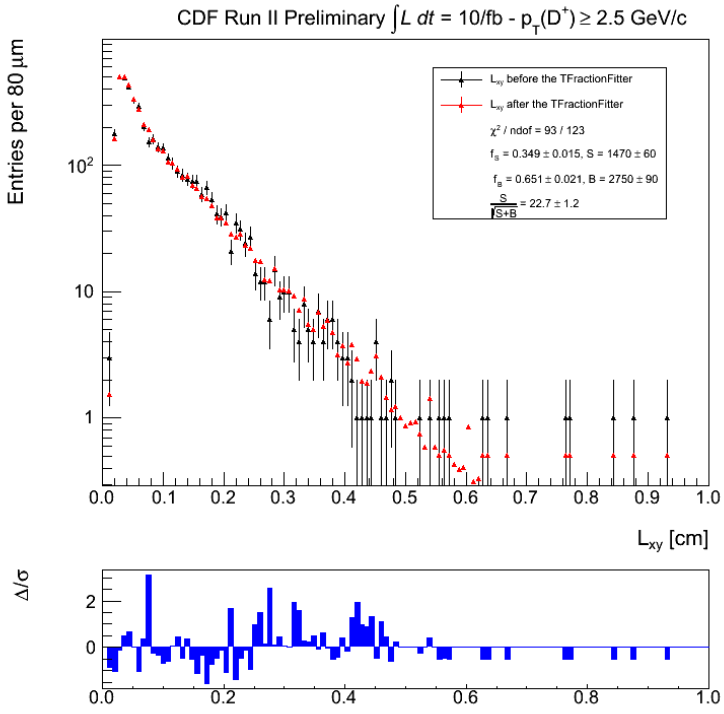

(b) TFractionFitter.

Figure 6.10: *(a) Result of the fit on the invariant $K^-\pi^+\pi^+$ mass plot when we don't cut on L_{xy}; (b) L_{xy} before (black markers) and after (red markers) the TFractionFitter. Fit residuals are also shown.*

Chapter 7

Cross section

Using the results of the previous chapters, we present in this chapter the measurement of the D^+ meson production cross section.

The final goal of this analysis is the measurement of the low p_T D^+ meson inclusive differential production cross section at CDF II, defined as in the following formula:

$$\frac{d\sigma_{D^+\to K^-\pi^+\pi^+}}{dp_T}(p_T;|y|\leq 1) = \left.\frac{\frac{N_{D^+}+N_{D^-}}{2}(p_T)}{\Delta p_T \cdot L \cdot \varepsilon_{trig} \cdot \varepsilon_{rec}(p_T) \cdot Br(D^+ \to K^-\pi^+\pi^+)}\right|_{|y|\leq 1} \quad (7.1)$$

where:

- N_{D^+} and N_{D^-} are the yields of the D^+ and D^- signals in each bin of p_T. We report the cross section only for D^+ mesons while we measure the yields for both, D^+ and D^- mesons. So we include a factor 1/2; clearly what is actually measured is the average cross section for D^+ and D^- mesons. This is true only if we postulate a charge invariant production process through strong interaction.
- Δp_T is the bin width.
- L is the integrated luminosity of the data sample.
- ε_{trig} is the trigger efficiency.
- ε_{rec} is the global reconstruction efficiency of our candidates. This parameter takes into account geometrical and kinematical acceptances as well as the detector reconstruction efficiency of the signal.
- $Br(D^+ \to K^-\pi^+\pi^+)$ is the decay branching ratio of the channel used in this analysis.

- $|y| \leq 1$ is the rapidity range considered: the central region of the detector.

We report the differential cross section $d\sigma/dp_T$ integrated over the width of each bin because the average value of the cross section in the bin i, $\sigma_i/\Delta p_{T,i}$ differs from the value corresponding to the p_T value of the center of the bin.

The differential cross section integrated within each bin is shown in Figure 7.1 and we summarize the results in Table 7.1. We show only statistical uncertainties.

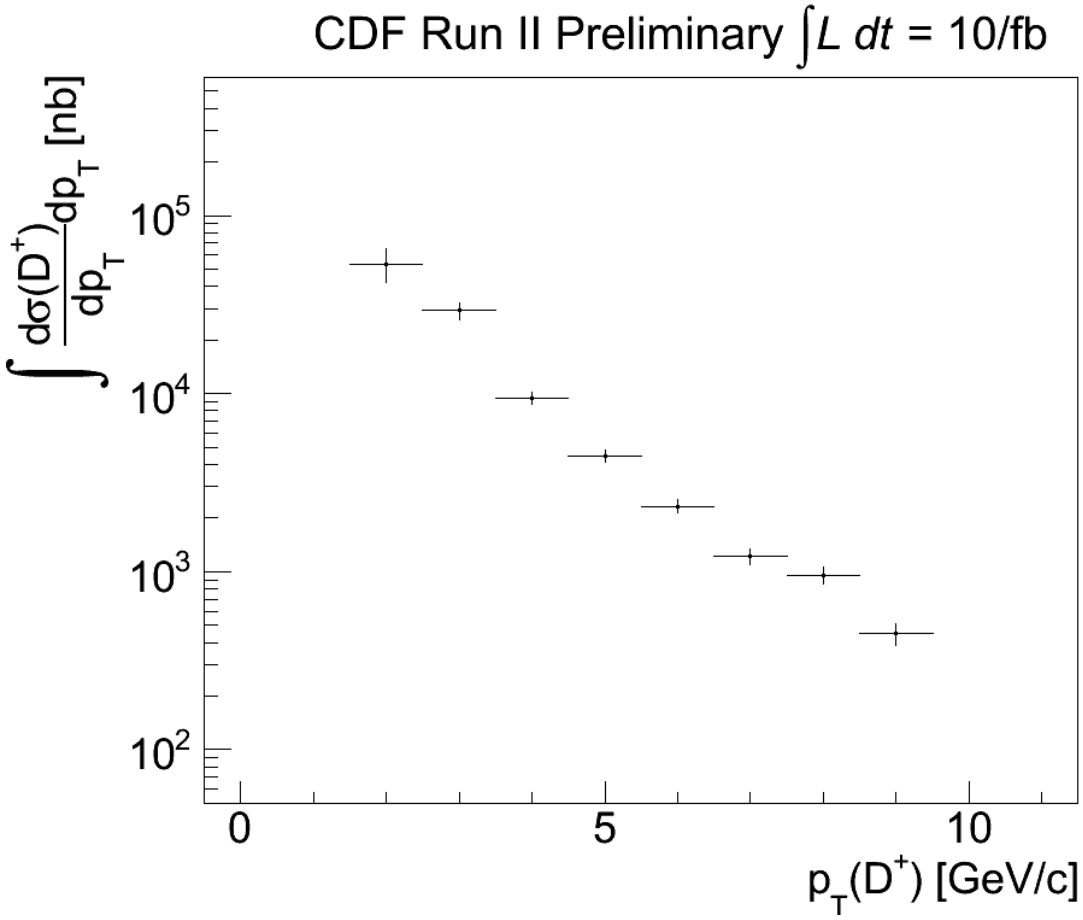

Figure 7.1: *D^+ meson inclusive differential production cross section as a function of the transverse momentum.*

At the beginning of Run II a similar measurement was perfomed. Our inclusive measurement covers the transverse momentum range [1.5, 9.5] GeV/c, while the published CDF II measurement probed the $p_T(D^+)$ range from 6.0 to 20.0 GeV/c and only for the direct component [20]. The published work has measured the differential cross section defined as in the following formula:

$$\frac{d\sigma_{D^+\to K^-\pi^+\pi^+}}{dp_T}(p_T;|y|\leq 1) = \frac{\frac{N_{D^+}+N_{D^-}}{2}(p_T)\cdot f_D}{\Delta p_T \cdot L \cdot \varepsilon_{trig}\cdot \varepsilon_{rec}(p_T)\cdot Br(D^+\to K^-\pi^+\pi^+)}\Bigg|_{|y|\leq 1} \quad (7.2)$$

which differs from our definition, given in equation (7.1), only for the direct fraction contribution, f_D (they don't consider the fraction of the D^+ coming from B^+ decays, but only the candidates produced in the primary vertex, see Sec. 1.4). If we want to compare them, we have to remove that contribution. In Table 7.2 are summarized the old results and the direct fraction corrections applied to each bin, while in Figure 7.2 we superimpose the two results after removing the correction factor from the published measurement.

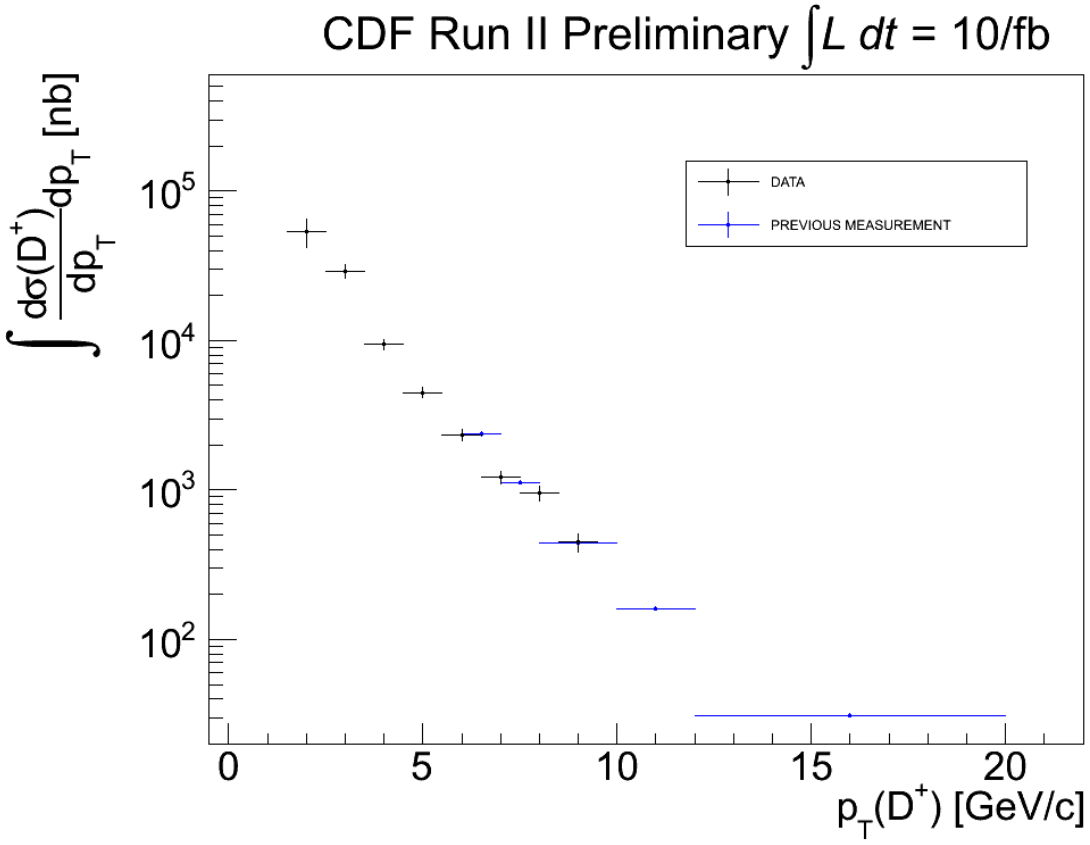

Figure 7.2: *Comparison between our result (black) and CDF previous measurement (blue) in the bins of overlapping.*

p_T [GeV/c]	[1.5; 2.5]	[2.5; 3.5]	[3.5; 4.5]	[4.5; 5.5]	[5.5; 6.5]	[6.5; 7.5]	[7.5; 8.5]	[8.5; 9.5]
$N_{D^+} + N_{D^-}$	320	540	1,040	820	540	400	320	238
stat (%)	40(25)	30(11)	40(8)	30(7)	20(7)	20(10)	20(12)	16(13)
syst (%)	-	-	-	-	-	-	-	-
L $[(\text{nb})^{-1}]$	16.0	16.0	16.0	16.0	16.0	16.0	16.0	16.0
stat (%)	-	-	-	-	-	-	-	-
syst (%)	0.9(6)	0.9(6)	0.9(6)	0.9(6)	0.9(6)	0.9(6)	0.9(6)	0.9(6)
$\varepsilon_{\text{trig}}$	1	1	1	1	1	1	1	1
stat (%)	-	-	-	-	-	-	-	-
syst (%)	0.004(0.4)	0.004(0.4)	0.004(0.4)	0.004(0.4)	0.004(0.4)	0.004(0.4)	0.004(0.4)	0.004(0.4)
ε_{rec} [%]	0.1044	0.3149	1.872	3.133	4.018	5.56	5.79	9.09
stat (%)	0.0010(1.0)	0.0021(0.7)	0.007(0.4)	0.012(0.4)	0.019(0.5)	0.03(0.5)	0.04(0.7)	0.06(0.7)
syst (%)	-	-	-	-	-	-	-	-
$\text{Br}(D^+ \to K^-\pi^+\pi^+)$ [%]	9.4	9.4	9.4	9.4	9.4	9.4	9.4	9.4
stat (%)	0.4(4)	0.4(4)	0.4(4)	0.4(4)	0.4(4)	0.4(4)	0.4(4)	0.4(4)
syst (%)	-	-	-	-	-	-	-	-
$\int \frac{d\sigma}{dp_T} \text{d}p_T [nb]$	54,000	29,000	9,500	4,500	2,330	1,220	960	450
stat (%)	12,000(21)	3,000(11)	700(8)	400(8)	200(9)	120(10)	100(10)	60(13)
syst (%)	3,000(6)	1,700(6)	500(6)	260(6)	130(6)	70(6)	600(6)	26(6)

Table 7.1: *Differential cross section measurement result.*

p_T [GeV/c]	[6; 7]	[7; 8]	[8; 10]	[10; 12]	[12; 20]
$\frac{d\sigma}{dp_T}\left[\frac{nb \cdot c}{GeV}\right]$	1961	986	375	136	19.0
stat [%]	3.6	2.9	2.3	3.0	3.0
syst [%]	17.0	15.9	16.5	17.4	17.2
f_D [%]	84.7	89.8	89.6	89.2	89.7
stat [%]	1.4	0.9	0.8	1.1	1.0
syst [%]	3.2	3.2	3.2	3.2	3.2

Table 7.2: *CDF published D^+ meson differential cross section.*

Chapter 8

Conclusions

In this thesis we present a study of the D^+ meson production in Minimum Bias and Zero Bias samples collected by the CDF II experiment at the Tevatron $p\bar{p}$ collider at Fermilab. We have measured the differential production cross section as a function of the transverse momentum down to p_T = 1.5 GeV/c.

Our study belongs to a series of experimental QCD studies. In fact, since the difficulty to apply perturbative expansion at scales below $\mu \sim \Lambda_{QCD}$, the production of charmed mesons at low p_T is a non pQCD process. This work represents the first measurement of the inclusive differential production cross section, for this charmed meson, extended to low p_T at a $p\bar{p}$ collider at the TeV scale. Recently, other measurements of charm production cross-section at low-p_T became available from the ALICE and LHCb experiments at the CERN LHC proton-proton collider. However, the present measurement maintains its uniqueness in terms of initial state ($p\bar{p}$) and center-of-mass energy ($\sqrt{s}$ = 1.97 TeV). Different processes within the regions we probed can occur at different energy scales: the comprehension of the energy dependence in non-pQCD is one of the most important open questions to solve..

Our result extends the published CDF II measurement [20] in the low p_T region. This gives the complete p_T spectum of the D^+ production from p_T = 1.5 GeV/c to p_T = 20 GeV/c.

Results will begin soon the internal CDF review process and they will be submitted to international journals for their prediction.

Appendices

Appendix A

Future improvements

In this appendix we describe the future improvements we can implement into the measurement discussed in this thesis.

A.1 Systematic uncertainties

In this work we consider as systematic uncertainty on the final cross section measurement only the luminosity. Nevertheless, there are other possible sources of systematic uncertainty due to the assumptions made in our work. The yields fitting procedure has been performed using a sum of two gaussians and a function to model the radiative tail. A different model could led to a variation in the signal yields. A mismodeling of the background shape may also introduce a systematic effect on the yield measured. Also the dependence on the MC for the absolute correction due to the reconstruction efficiency and the reweighting of the input cross section distribution can be a sources of systematic uncertainties. We are working on these aspects.

A.2 Direct fraction

We measured the inclusive cross section of D^+ mesons at the Tevatron's energy; this means that we are integrating two contributions:

Direct fraction : the prompt fraction of D^+ represents the mesons that are directly generated in the $p\bar{p}$ interaction.

Secondary fraction : several D^+ are produced by B mesons decays; unlike prompt D^+ these secondary D^+ have an origin vertex displaced w.r.t. the primary $p\bar{p}$ interaction because of the relatively long lifetime of the B mesons.

We are interested in measuring the direct component alone because it is the only one related to the $c\bar{c}$ production due to the QCD interactions. We can assess the

direct component using data. In fact the secondary component has a wider impact parameter distribution because of the displacement of the origin of the D^+ with rispect to the $p\bar{p}$ interaction point. A fit of the impact parameter can tell us the fraction of direct D^+.

Appendix B

Selection studies

Before to optimize our data-sample, we performed some selection studies. This appendix is devoted to their description.

Before performing the final selection optimization procedure, we used the following arbitrary to select the D^+ candidates:

- two $p_T(TRK) \geq 0.5$ GeV/c.
- $|d_{0,max}| \geq 50\mu m$ or $|d_{0,min}| \geq 50\mu m$;
- $\chi^2_{red} \leq 10$;
- $L_{xy} \geq 750$ μm.

Using this selection we studied some features of the sample.

B.1 Secondary peaks in the $d_0(TRK)$ distribution

Looking at the distribution of $d_0(TRK)$, two structures around ± 750 μm were evident, as shown in Figure B.1 (blue markers). These bumps were not reproduced by the Monte Carlo simulation (red markers). We noticed that the average values of these gaussian-like peaks is highly dependent on the threshold on the L_{xy} cut.

Figure B.2 shows the $d_0(TRK)$ distribution when we apply the same selection on the sample, but varying L_{xy}: $L_{xy} \geq 250$ μm (red markers), $L_{xy} \geq 500$ μm (purple markers), $L_{xy} \geq 750$ μm (blue markers), $L_{xy} \geq 1000$ μm (green markers) and no cuts on L_{xy} (black markers). The peaks are centered at about ± 250 μm, ± 500 μm, ± 750 μm and they disappear when we don't cut on L_{xy} or at 1000 μm because the n-tpules are selected for $0 \leq |d_0(TRK)| \leq 1$ mm.
We know that $d_0(TRK)$ and L_{xy} are strongly correlated, as shown in Figures 3.11.

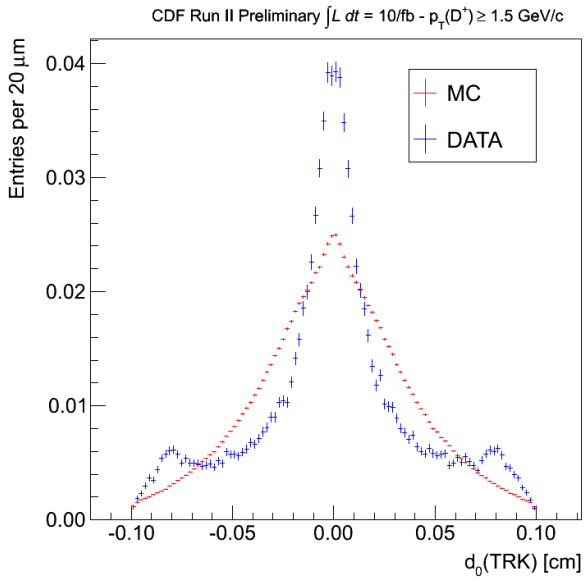

Figure B.1: *Distribution for the impact parameter of the tracks, $d_0(TRK)$. Red markers are for the Monte Carlo (MC) sample and blue markers for the data sample.*

We have pointed out that cutting on one variable, we modify the shape the distribution of the other, generating the anomalous peaks observed in the $d_0(TRK)$ distribution. In addition to that, this effect is not simulated by the MC because it is only due to the random fake candidates of the combinatorial background and in our MC sample we are simulating only real candidates.

B.2 D^{*+} contamination

In the previous analysis on the D^+ at CDF II [20], the $K\pi\pi$ invariant mass distribution showed a secondary peak, around 2 GeV/c^2, identified as accidentally selected D^{*+} ($m_{D^{*+}} = 2010$ MeV/c^2), as evident in Figure B.3(a). In order to remove this contamination, it has been used a cut on the the invariant mass: only candidates which satisfy the criterion $\Delta m = |m(K\pi\pi) - m(K\pi)| > 0.18\, GeV/c^2$ were selected ($m(K\pi)$ is the invariant mass of a specific pair, called the trigger pair[1]). In Figure B.3(b) is show the $K\pi\pi$ invariant mass distribution selected with this criterion on Δm. As evident, the D^{*+} signal disappeared.

In our case, the $p_T(D^+)$ integrated selection doesn't exhibit this contamination, as evident in Figure B.4(a). As a double-check, in Figure B.4(b) we select only candidates which satisfy the same Δm criterion and, in Figure B.4(c), only candidates

[1] two trigger tracks were called trigger pair if they had opposite charge, $p_{T1} + p_{T2} \geq 5.5\, GeV/c$ and $2^\circ \leq |\Delta\phi_0| \leq 90^\circ$.

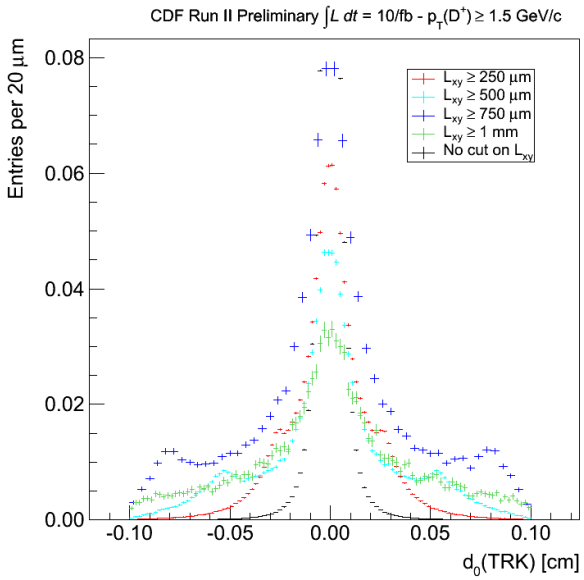

Figure B.2: *Distribution for the impact parameter of the tracks,* $d_0(TRK)$*, applying the same selection described in the text, but for different cuts on* L_{xy}*.*

for $\Delta m < 0.18\, GeV/c^2$; we have no evidence of contamination in our sample.

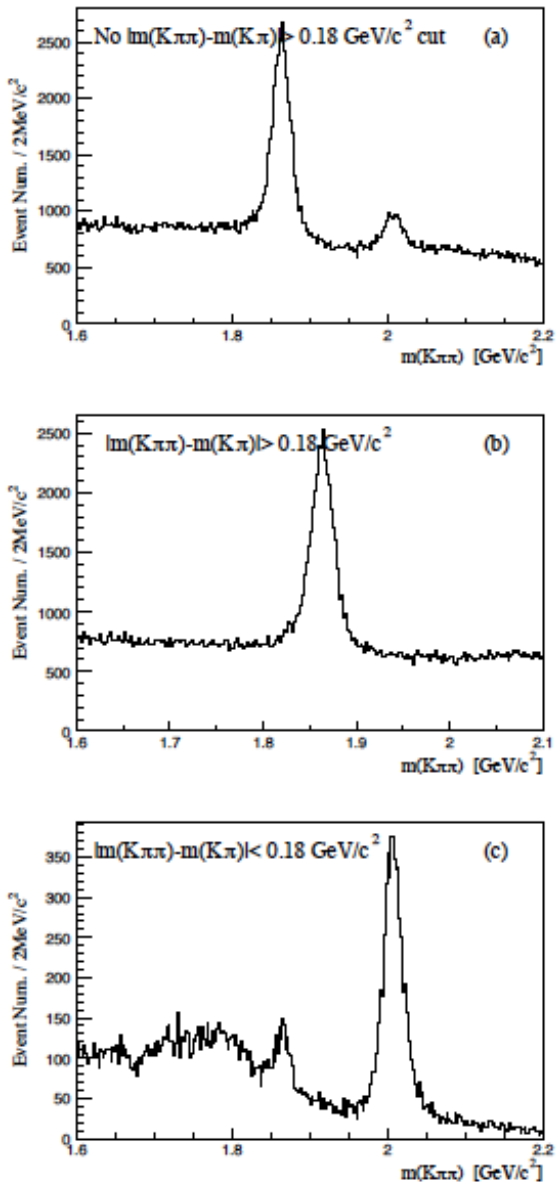

Figure B.3: *Previous analysis on the D^+ at CDF II: $K\pi\pi$ invariant mass distribution for $D^+ \to K^-\pi^+\pi^+$ candidates with different criteria on $\Delta m = |m(K\pi\pi) - m(K\pi)|$.*

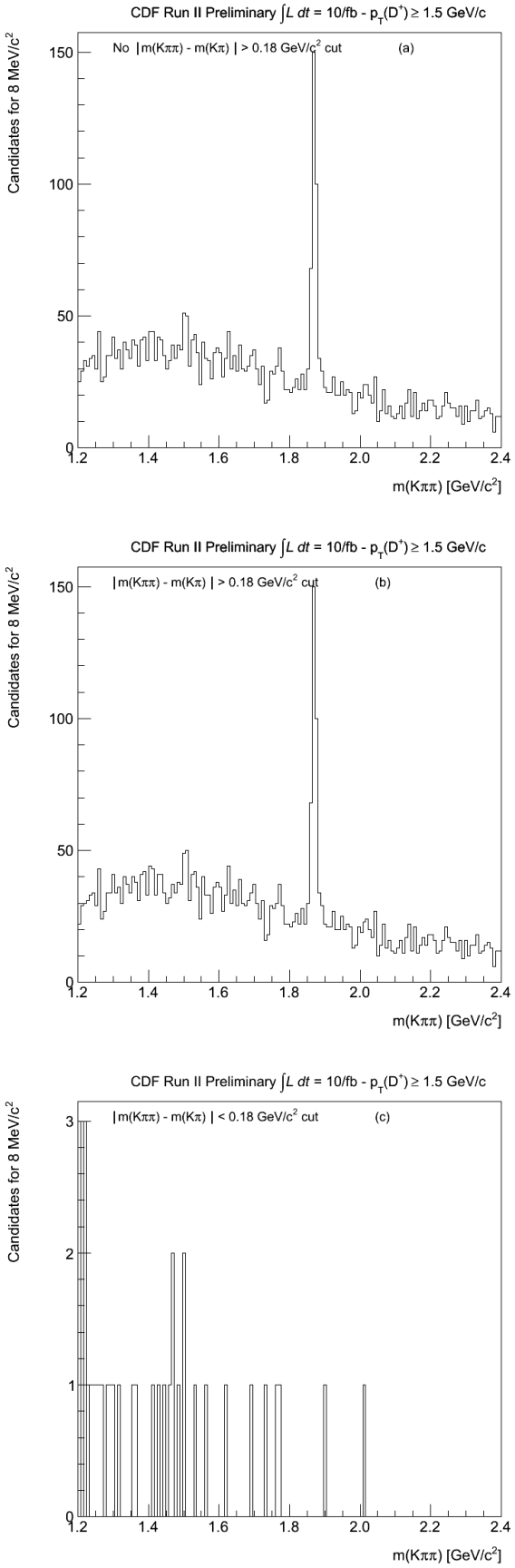

Figure B.4: *The $K\pi\pi$ invariant mass distribution for $D^+ \to K^-\pi^+\pi^+$ candidates with different criteria on $\Delta m = |m(K\pi\pi) - m(K\pi)|$.*

Bibliography

[1] P. W. Higgs, *Broken Symmetries, Massless Particles And Gauge Fields*, Phys. Lett. **12** (1964) 132.

[2] P. W. Higgs, *Broken Symmetries And The Masses Of Gauge Bosons*, Phys. Rev. Lett. **13** (1964) 508.

[3] The ATLAS Collaboration, *Observation of a new particle in the search for the Standard Model Higgs boson with the ATLAS detector at the LHC*, Phys. Rev. Lett. **B 716** (2012) 1-29.

[4] The CMS Collaboration, *Observation of a new boson at a mass of 125 GeV with the CMS experiment at the LHC*, Phys. Rev. Lett. **B 716** (2012) 30.

[5] Cian O'Luanaigh, *New results indicate that new particle is a Higgs boson*, Home.web.cern.ch.

[6] K. Nakamura *et al.* [Particle Data Group], J. Phys. G **10**, (2010).

[7] A.V. Manohar and M. B. Wise, Camb. Monogr. Part. Phys. Nucl. Phys. Cosmol. **10**, 1 (2000).

[8] Cabibbo, N. Phys. Rev. Lett **10**: 531 (1963).

[9] Ikaros I. Y. Bigi, *Charm physics - like Botticelli in the Sistine chapel*, hep-ph/0107102 (2001).

[10] The BELLE Collaboration, Phys. Rev. Lett. **98** 211803 (2007).

[11] The BaBaR Collaboration, Phys. Rev. Lett. **98** 211802 (2007).

[12] The CDF Collaboration, Phys. Rev. Lett. **100** 121802 (2008).

[13] The LHCb Collaboration, Phys. Rev. Lett. **108** 111602 (2012).

[14] The CDF Collaboration, Phys. Rev. Lett. **D 85** 012009 (2012).

[15] The PHENIX Collaboration, Phys. Rev. Lett. **97**, 252002 (2006).

[16] The STAR Collaboration, Phys. Rev. Lett. **98**, 192301 (2007).

[17] The STAR Collaboration, Phys. Rev. Lett. **94**, 062301 (2005).

[18] The ALICE Collaboration, arXiv:1201.0729v1 [nucl-ex], (2012).

[19] C.Chen, R. Oldeman and J. Kroll, CDF note 5859, (2002).

[20] D. Acosta *et al.* [CDF Collaboration], Phys. Rev. Lett. **91**, 241804 (2003).

[21] B. A. Kniehl, G. Kramer, I. Schienbein and H. Spiesberger, AIP Conf. Proc. 792, 867 (2005).

[22] B. A. Kniehl, G. Kramer, I. Schienbein and H. Spiesberger, Phys. Rev. Lett. **96**, 012001 (2006).

[23] J.Appel, M.Mussini and D.Tonelli, CDF note 11044, (2013).

[24] Fermilab Beam Division, *Run II Handbook* and *Operations Rookie Books*.

[25] R. Blair *et al.* [CDF Collaboration], *The CDFII Detector: Technical Design Report*, FERMILAB-Pub-96/390-E (1996).

[26] D. Acosta *et al.*, CDF note 6052, (2002).

[27] S. Klimenko, J. Konigsberg and T. Liss, CDF note 6314, (2003).

[28] R. Brun *et al.*, *ROOT object oriented data analysis framework.*, http://root.cern.ch.

[29] D. Acosta *et al.* [CDF Collaboration], Phys. Rev. Lett. **D 50**, 5518 (1994).

[30] S. Klimenko, J. Konigsberg and T. Liss, *Averaging of the inelastic cross sections measured by the CDF and the E811 experiments*, CDF note 0741.

[31] K. Anikeev, P. Christoph and P. Murat, *Description of Bgenerato II*, CDF note 5092, (1999).

[32] J. Lewis and P. Avery, CDF note 2724, (1994).

[33] R. Brun *et al.*, *GEANT: Simulation Program For Particle Physics Experiments. User Guide and Reference Manual*, (1978).

[34] P. A. Movilla Fernandez, *Performance of the CDF calorimeter simulation in Tevatron Run II*, AIP Conf. Proc., vol. 867, pp. 487-494, (2006).

[35] R. Veenhof, *Garfield, a drift chamber simulation program*, International Conference on Programming and Mathematical Methods for Solving Physical Problems, Dubna, Russia, 14-19 Jun (1993).

[36] D. Acosta *et al.*, CDF note 5861, (2002).

[37] D. Acosta *et al.*, CDF note 6054, (2002).

[38] N. Moggi and F. Rimondi, CDF note 8594, (2006).

[39] ROOT, class guide, http://root.cern.ch/root/htmldoc/TFractionFitter.html

[40] R. Barlow, C. Beeston, *Fitting using Monte Carlo samples*, Computer Physics Communication 77 219-228 (1993) .

Riflessioni alla deriva / Free thoughts

Caro paziente lettore, giusto una premessa. Quello a cui stai per assistere è un vero flusso di coscienza. Troverai un po' di tutto: riflessioni alla deriva, ringraziamenti in italiano e in inglese, ironia, pathos, formalità, cazzimma e nostalgia, perchè dopotutto è il modo in cui ho vissuto questi anni magistrali. Se ti è piaciuto l'Ulisse di Joyce apprezzerai, altrimenti salta al punto che ti interessa. I ringraziati sono in grassetto, proprio per aiutarti a selezionare facilmente.

Finalmente, dopo questa lunga tesi, mi ritrovo un attimo a pensare alla conclusione di tutto questo percorso e di cosa abbia significato. E' indubbio che questa laurea, più che la triennale, chiuda un'epoca della mia vita: il periodo da studente universitario. E' singolare, ma se mi soffermo a ricordare il liceo, tutti i miei ricordi più o meno coscienti volgevano in tutt'altra direzione. Ricordo esattamente una conversazione con il mio compagno di banco: "Farò lettere classiche o altro, ma sicuramente non fisica". Complici troppi film di Indiana Jones e troppi fumetti di Indiana Pipps, da piccolo mi vedevo come un moderno archeologo, infossato da qualche parte nel mondo a cercare chissà quale civiltà perduta. Grazie al superamento del test scritto d'ammissione alla Scuola Normale di Pisa per la classe di lettere, sembrava ormai quasi fatta e invece... si è profilato un nuovo percorso. Quello è stato un boccone amaro da mandar giù, ma oggi, vedendo quanto sono riuscito a colmare quella voragine di conoscenza che mi assilla sempre e soprattutto le persone che ho incontrato, sono molto soddisfatto di come siano andate le cose.

RINGRAZIAMENTI

Proprio lì, in Piazza dei Cavalieri, secondo un percorso tutt'altro che lineare, mi sono riavvicinato alla **Fisica**, questa misconosciuta. E' curioso, ma nel mio immaginario è sempre stata donna, alta, bionda e con uno sguardo nordico, misterioso. Il primo grazie di questa tesi è per lei: si è brutalmente imbattuta sulla mia strada, inizialmente ripudiata, con il tempo ammirata e infine osannata. Inutile dirlo: è la mia relazione femminile più duratura, ci frequentiamo da circa dieci anni e ancora riesce ad appassionarmi ogni volta che lascia intravedere qualcosa.

Potrei porre innumerevoli grazie sul piatto della stadera, ma il romano dovrebbe sempre essere sopra portata massima per i grazie rivolti alla mia **famiglia**, cinque "bimbi" inclusi (lo so, non si può sentire, ma bisognerebbe chiedere a mia sorella in merito).

- **Mio padre**, che ormai conosce la strada Cervinara-Capodichino a memoria; quest'anno poi, ha sperimentato diverse volte anche Cervinara-Piazza Garibaldi. Per fare economia i voli sono sempre nelle ore notturne più improponibili e gli tocca sempre la levataccia alle tre di notte. Quando si parte, la curiosità del nuovo e l'avventura compensano abbondantemente tutte le levatacce notturne, ma se poi accompagni solo? Come compensi? Questo pensiero accompagna tutti i miei voli europei, quando riesco a non dormire.

- **Mia madre**, e che lo diciamo a fare? Ha praticamente preso due lauree con me. Cosa singolare, solo adesso è riuscita a ricordare in cosa ci laureiamo, ma scommetto che per il giorno della seduta già avrà rimosso il tutto.

- **Vale** (il nomignolo affettuoso lo risparmiamo pubblicamente) con cui condivido la passione per il nuovo e ormai anche per il mal d'Africa. Quella che in casa più ha capito l'idea dello sforzo, sempre pronta a spronare per le corse agli esami (seriamente, Angi', ma è ancora lei quella della foto casa-barbie?)

- **Angina**. Ancora mi diverto a vedere la faccia della gente quando mi chiedono: "Ma qual è il cane Angini?" e quando poi spiego la storia Angino-Angina e il cane che si chiama Gennaro, è d'obbligo la riflessione: "Ma tu hai il nome di un cane e il cane il nome di una persona?!Gesù". Posso solo dire che non ti sopporto più: posso stare a stretto contatto con te per non più di cinque mesi. Superata questa soglia, quando parli sento solo un bla bla bla e ancora bla bla bla. Parli proprio tanto.

- **Gennaro**, in arte zampetta palmata (per i soprannomi, chiedere ad Angina). Ormai ogni mattina mi sveglio sentendo un'alitata calda e aprendo gli occhi vedo una lingua in faccia. Ci siamo rassegnati, ha la sindrome del figlio unico. Non bastava il disturbo del comportamento felino? No ma', non entrano in casa la mattina, è solo una metafora.

- **Lady**, in arte dumbina. La sola bionda del mio cuore. Ha studiato con me fino a Fisica 2, poi si è arresa. L'approccio con la quantistica è stato traumatico; e dire che prometteva così bene. L'unica dei cinque ad avere un profilo facebook e ad essere immortalata nella storia con un'ode. Seriamente, devo trovare un modo per portarti con me, wherever I will go.

- **Pisellina**, in arte? Non lo so, già è stato sconvolgente per lei scoprire che il nome anagrafico è Pisella (come detto, per i nomi vedi la voce Angina, eccetto

Gennaro per il quale ho scelto io). E' rimasta così scioccata dalla scoperta che è arrivata a pesare quasi 60 kg, ma ora ha deciso di mettersi a dieta per la mia laurea.

- **Pongo**, per tutti il pagliaccio di casa. Sì, non ti sopporto, mi fai sempre innervosire, ma è pure vero che sei il più simile a me per carattere. E poi, deh, oggi sono positivo, per la laurea più crocchette anche per te.

- **Bobo** (stavolta chiedi a Vale). Devi capire una cosa, più ti butti a pancia all'aria cercando coccole, meno ne ricevi. Prendi esempio da Lady, ci snobba sempre e noi puntualmente la cerchiamo. La sai la storia della selva di Ariosto? E' uguale. Provvedi in merito.

- **Gigione**, mio nonno, che onoro ogni giorno portando il suo nome. Siamo ormai giunti almeno alla centesima volta in cui mi chiede cosa studio. Dopo risposte entusiaste sulle particelle e il senso della vita con esiti ampiamente deludenti, un po' di tempo fa provai a rispondergli: "No', vedi il fulmine fuori? E vedi la presa della corrente? Qualcuno che faceva il mio mestiere, ma più bravo di me, un po' di anni fa capì che sono parenti e come portarti la corrente in casa. Sì, hai ragione, il fulmine però non lo paghi. " e la replica: "Ah, ma allora si nu' scienziat, quindi faticherai a' televisione!". Diciamo che ero abbastanza soddisfatto e inorgogliosito, fino a ieri, quando ha esordito nuovamente: "Ma allor piglierai o'post o'sportell nu riman?". A quel punto, sconfitto, mi sono rassegnato a rispondere: " Sì no', lavorerò allo sportello in banca". Un grazie di cuore anche a mia **nonna**, che per poco non è riuscita a vedere anche questa conclusione. Penso che tu adesso avrai capito cosa faccio e soprattutto saprai quando mi sposerò, visto che era il problema che ti assillava più di tutti.

Posso solo dire che non siamo la famiglia del Mulino Bianco (per fortuna, aggiungo!), ma davvero rivedo "questa bella d'erbe famiglia e d'animali".

Un grazie sentito va al **gruppo CDF di Bologna** che mi ha seguito in quest'avventura. Ognuno di loro mi ha arricchito in qualche modo e mi ha fatto sentire come parte di una grande famiglia, soprattutto durante i due mesi che ho trascorso a Bologna.

Un doveroso grazie è per il prof. **Franco Rimondi**, che con il suo sì ha permesso l'inizio di questo percorso. Non ho avuto la fortuna di lavorarci a lungo a causa della sua prematura scomparsa, ma conservo un gran bel ricordo del mese trascorso insieme nel trailer 137 A di CDF. La garbatezza e l'originalità sono la naturale cornice di questo ricordo. Grazie alla gentilezza di qualcuna, conservo con grande affetto il papillon che indossava il primo giorno che l'ho incontrato.

Un caloroso e sentito grazie è per il prof. **Stefano Zucchelli**, primo relatore di questa tesi, che ringrazio per i vari suggerimenti sull'analisi e non solo. Fra tutte le sue qualità, quelle che mi hanno sempre colpito di più sono l' eleganza e soprattutto la professionalità con la quale guida il gruppo, riuscendo a farti sentire come in una

grande famiglia, più che in un semplice gruppo di ricerca. Se mi dovessi vedere un giorno a capo di un gruppo, mi piacerebbe possedere queste varie qualità nella stessa armonica proporzione.

Ancora, un affettuoso grazie a **Milena Deninno**, cuore e burocrate del gruppo. Se tutti i gruppi avessero una Milena, probabilmente ci sarebbe la consapevolezza che le cose filano senza ingiustizie, ad eccezione di qualche furto di pollame di cioccolata dal suo ufficio, unico sollievo a qualche giornata di analisi andata male.

Grazie a **Niccolo' Moggi**, che nonostante i suoi numerosi impegni, mi ha aiutato molto nella scrittura della tesi e mi ha fornito vari suggerimenti durante i BO-meetings, nonché il più acuto osservatore a notare il Paperino che ha deciso di farci compagnia nell'analisi.

Un simpatico grazie a **Elena**, che si è prestata a darmi una mano con l'analisi e per di più mi ha fatto scoprire una piccola passione per il trash fra i vari sogni americani. Lavorare con lei e Manuel ha ricreato proprio l'idea di gruppo che avevo in mente quando immaginavo il mio lavoro di tesi. La giornata dei cataclismi transoceanici è stata la vera chicca di questa tesi.

Lascio per ultimo **Manuel Mussini**, perché voglio spendere qualche parola in più per la persona più significativa di questa tesi. Tutte le parole che posso usare non compenserebbero nemmeno minimamente quanto ti devo.

Se mi ritroveró autore di un articolo cosí giovane, è solo merito tuo.

Se ho potuto risolvere tutte le obiezioni che mi venivano mosse dall'esterno della collaborazione, è solo merito tuo.

Se ho potuto risolvere i vari problemi dell'analisi entro tempi contratti, è solo merito tuo, soprattutto perchè so quanto posso essere fastidioso con proposte nuove di cose da fare. E che dire della tua grande diposponibilità praticamente a tutti gli orari? Non dimentico la lunga "emailata" fino alle due di notte per sistemare il problema della MC (ancora oggi immagino le "bestemmie" di Federica!).

Se ancora oggi quando scrivo le macro le organizzo in un certo ordine, è solo merito tuo.

Se ... ..., è solo merito tuo.

E dire che quando ho spulciato il tuo profilo facebook prima di conscerti, ho pensato: "Cominciamo male, è un amante dei gatti. Io non li sopporto proprio". Invece poi, ho trovato anche un amico, oltre che un grande ricercatore. In principio mi avevi scambiato per la volpe del Piccolo Principe, ma poi, grazie a qualche vivace presentazione, si è creata una sinergica intesa. In più, grazie ad Otto, mi sono più simpatici i gatti. Grazie anche a Federica e a tutta la tua famiglia per il pranzo e il buon nocino (mi piaceva di più quello freddo!).

Un doveroso grazie anche al prof. **Luciano Ristori** per i suoi suggerimenti e spunti critici all'analisi, nonché per le semplici speculazioni sui limiti di alcuni concetti cardini dell'analisi statistica (confidence level etc...) che mi hanno consentito di rendere un po' più applicative delle conoscenze didattiche relative ad un ambito che mi appassiona molto, l'analisi statistica per la fisica delle alte energie. Spero

che queste chiacchierate possano continuare almeno in un futuro prossimo.

Ero piccolo, leggevo il Topolino e il mio ideale di scienziato aveva un nome, Archimede. Oggi posso dire di averlo incontrato "in carne e piume", il prof. **Fabio Ambrosino**, mio relatore napoletano. Grazie perchè, avendo visto quanto ci tenevo, si è cimentato in questa tesi molto sui generis e complessa per via delle varie difficoltà burocratiche. Se le molle possono essere appese al soffitto e se non sudo più freddo quando sento nominare il χ^2, è solo merito suo. Il corso di Analisi Dati in Fisica Subnucleare è stato per me uno dei più colorati, formativi e belli che abbia mai seguito. Fra le tante massime del corso, posso solo dirle che non vedo l'ora di divorziare dalla mia analisi.

Ringrazio molto anche il mio correlatore, il prof. **Guglielmo De Nardo**, per una riflessione critica sulle analisi multivariate e la loro concreta applicazione nella fisica delle particelle. La ringrazio anche per i suggerimenti sul futuro e su quale possa essere una scelta più consona alle mie aspirazioni.

Marco Trovato (in arte Franco), il ringraziamento nei tuoi confronti è duplice per questo ti metto a parte. Penso che dopo Manuel sei stato la persona che ho assillato di più con i mie fastidiosi: "Aspe' hai ragione, ma se...". Quante serate a parlare in casa Frascati del segno meno nelle pulls oppure le infinite conversazioni sul TFractionFitter. Anche se stanchissimo per la tua "laurea", ti sei sempre fermato a parlare (un paio di volte però sonnecchiavi mentre parlavo, ma sei giustificato perchè era mezzanotte e io non accennavo a smettere). E poi, Franco, che devo di'?! Sei stato il wingman perfetto! La compagnia del baccaglio trova in te il suo fondatore. E i guai che mi hai creato con messaggi inopportuni? Meno male per te che è finita bene, perchè altrimenti avresti passato un brutto guaio.

Chicago, la città di cui mi sono perdutamente innamorato. Non si può non ringraziarti. Erano le due di notte, mi ero perso sulla 290. Di sfuggita ho visto la tua skyline nello specchietto retrovisore e una profonda fitta mi ha tramortito: mi sono sentito subito a casa, anche se parecchi km più in là. Per diversi momenti mi hai fatto vivere come in un libro di Fitzgerald e io, come un moderno Gatsby. Grazie anche per avere una così folta comunità dell'Est Europa.

Poi c'è tutta la famiglia Fermilab, che ha reso piacevoli autunni ed estati in quel di Chicago, Batavia e dintorni. Un profondo grazie per:

- **Anna Mazzacane**, per avermi fatto ritrovare un po' di Federico II in quelle lande sperse americane. Sempre gentile e disponibile. Quando era tardi e nei trailer non c'era più molta gente, sapevo che poco dopo le fotocopiatrici, in uno studio un pò lontano, c'eri sempre per una chiacchierata pre-cena.

- **Anna Driutti**, per le numerose dritte sui GRE, l'organizzazione americana e anche per un po' di terrore per il sistema sanitario americano. In più, tante grazie anche per esserci stata quel Sabato pomeriggio nei trailer, quando davvero non c'era nessuno.

- **Matteo Cremonesi**, pur partendo da punti di vista diversi, sei la persona più simile a me che conosca in termini di ambizione e aspettative di vita. Ti devo di' grazie almeno per un tris di belle serate e informazioni varie, ma ti dico solo che abbiamo arretrato un road trip saltato una volta per i miei, una volta per i tuoi impegni. Speriamo che in un prossimo futuro si concretizzi.

- **Gianfranchino**, sempre disponibile per parlare di analisi e per uscire. Quando nessuno vuole uscire, tu ci sei sempre. Sei il mio uomo, colui che mi ha fatto vivere in un bell'appartamento da scapolo per parte dell'estate 2013. L'uomo delle torte gelato, che ho mangiato in modo ortodosso e non.

- **Ivano**, per tutti la bestia roscia (ha sollevato ben 90 kg di panca, occhio!) che mi ha fatto divertire per parecchie serate autunnali e che parla parla parla... e ancora parla parla parla... Un ricordo su tutti? La festa di Halloween nel granaio del Fermilab.

- **Giani**, il buon vecchio Giani, che mi ha snobbato per i russi ultimamente. Aspe', la rifaccio: Giananto', il buon vecchio Giananto', che mi ha snobbato per i russi ultimamente. Lo guardi e ti chiedi come possa essere possibile contenere così tanta energia frenetica in tale volume. Ormai ti associo ad una parola, quando la sento pronunciare mi viene in mente sempre la tua vocina e una tua foto in quella via. Aspetto sempre un invito per delle nozze...

- **Ludovico**, Mr banana-man. L'uomo dall'accento perfettamente British, un po' snob insomma. E' scolpito nella mia memoria un momento colmo di pathos. Io e te che parliamo di come alle ragazze piaccia bearsi se si vedono riflesse negli occhi degli uomini e Giani che irrompe con il nome di una famosa via (vedi sopra).

- **AndreaTau**, così elegante e garbato nei modi di fare, ma anche un così arguto fotografo. Ho scoperto una nuova passione per la fotografia. Confesso che certe prospettive che mi hai fatto notare, mi erano completamente estranee. Se fossi un numero, saresti il n.57.

- **Sandrina**, per la dolcezza e semplicità con la quale mi ha fatto osservare alcuni aspetti umani che non avevo notato. Anche se appena di ritorno da una pausa caffè, ti sei sempre lasciata tentare da un mio cioccolatino, caffè bis-tranello oppure da una lunga passeggiata verso la TD. Per non parlare delle mie irruzioni improvvise nel tuo ufficio o dei biglietti alla Grande Fratello; però, la cena di compleanno la sera della mia partenza...imperdonabile!

- **Er Vix**, così burbero, ma così di cuore. Non si può non pensarti mentre borbotti qualcosa, però sei anche stato il compagno di palestra più fedele di FNAL. Rimane storica la toccata del magnete, neanche la Madonna dell'Arco può arrivare a tanta devozione.

- **Camilla**, per avermi fatto sforzare enormemente a ricordare il frullatore di Gianfranchino e poi, nemmeno una torta in ricompensa. A parte gli scherzi, grazie per le chiacchierate sulle correlazioni e sui TFractionFitter.

- **La Marghe**. Non si può chiudere la rassegna FNAL senza la Marghe. Grazie per i numerevoli passaggi all'aeroporto, per i caffè in TD, per la compagnia alla partita NBA. Sei a tuo modo parecchio sorprendente: uno ti conosce e di primo acchito si fa un'idea di te e poi ecco, quando pensa di averti inquadrata, dici qualcosa che rompe tutto lo schema. E' rimasto in sospeso l'esperienza gospel, ma tranquilla... dopotutto hai in ostaggio almeno un paio di miei jeans e di scarpe da running.

- **Guendalina**, l'anatra che mi posteggiava sotto l'ufficio nel trailer 137 A nel Novembre 2012. No, i tuoi canti d'amore non mi hanno mai persuaso. Spero vivamente che sia finita sul piatto di qualche americano per il Thanksgiving.

Grazie a tutti ragazzi, dopotutto molti di noi sono stati l'ultima generazione CDF.

Un affettuoso ringraziamento è poi per tutti i **summer students italiani del 2011**, con i quali ho scoperto la meravigliosa realtà targata FNAL. Primi fra tutti i miei due coinquilini, **Marino** e **Stefano**, per la passione e la determinazione con la quale abbiamo condiviso l'esperienza. Inoltre per le uscite serali, i passaggi, le donuts all'una di notte, i confronti etc... **Paolino**, perchè è Paolino. Che si può dire? E' il solo capace di mettersi la giacca per un'udienza in un tribunale americano, il solo capace di pronunciare e ricordare un paese nelle vicinanze di Naperville (Chris, l'impiegato della Chase, ancora ride di te!) ed il solo responsabile, se sono ritornato a casa senza qualcosa che non era la dignità. Quando poi aggiungi **Schicchi**, la coppia è completa. Basta provare a chiedere la strada per Hooters e la miccia è accesa. Se poi incuriosisci Schicchi con la cazzimma, il divertimento è assicurato. **Mattew**, per avermi fatto appassionare ai suoi racconti in cui alla fine c'era sempre qualcuno che faceva qualche sortilegio e tutti che facevano sesso con tutti. Ah, un'altra cosa, la flebotomista! **Gabriele**, per la serata targata Paris e per la tranquillità con la quale raccontava anche le cose più improponibili.

Poi ci sono gli **amici storici**, quelli di vecchia data. Prime fra tutte le Assunte. Per una strana sorte del destino, la mia vita è piena di Assunte. Per un periodo sono state addirittura tre. Felix, il giorno della laurea potrai finalmente associare dei volti a dei miei racconti e fare meno confusione.

Susy, una delle poche persone che vanta il primato di comparire in entrambe le tesi. Posso solo autocitarmi, ricordando che se non ci fossi stata, sarebbe stato molto difficile prendere queste due lauree. Grazie per essere stata una coinquilina speciale, per esserti inzuppata di acqua putrida di seppioline alle 6 di mattina, per esserti sorbita i miei sfoghi sui 30 che non sentivo rappresentativi della mia conoscenza, per i supporti alle corse esami etc... Quando le cose non quadrano e sembra che non ci

sia soluzione, bisognerebbe guardare un po' il mondo con quei tuoi buffi occhialoni neri.

Assunta-Milano, per fare la differenza ti ho sempre chiamato così con tutti. In realtà poi, mentre io facevo Gigino o'mmericano, tu sei diventata Assunta a'straliana. Sicuramente mi dovrò sorbire una ramanzina perchè non sei la prima. Siamo amici da 13 anni, quasi metà vita. Che devo dire? Ogni qualvolta ho un problema ci sei sempre per consigli, suggerimenti o anche solo per parlare. Eppure non sei sempre stata proprio a portata di mano. Mi fai morire: parti sparata con la tua obiettività pungente, poi torni sui tuoi passi perchè la tua grande emotività prende il sopravvento. Basta smancerie, la chiudo solo dicendo che tutti avrebbero bisogno di una Assunta nella propria vita, anche solo per un giorno, in modo da notare la differenza.

Carmina che ha sopportato una convivenza molto divertente: allenamenti in corridoio, stramba gente in casa, scherzi all'improvviso, euforia da abbuffata di cioccolata... insomma quella che abbiamo allegramente definito la vita nell'appartamento "napulegno". Ora hai scelto Torino, ma Napoli resta nel cuore, soprattutto casa Monfregola.

Nico, il mio compagno di banco di una vita, anche quando non divideva esattamente a metà lo spazio. Grazie per avermi fatto vivere un gran bell'anno, quando sono tornato stabile a Cervinara. E soprattutto grazie per avermi fatto conoscere **Jhonny**, che mi ha fatto divertire assai. Mi avete fatto scoprire il piacere di stare davanti alla "Gola" a fare due chiacchiere, pensando che la Domenica pomeriggio potesse essere infinita... mi avete fatto riscoprire il bello del paesello, un po' offuscato da tanta americanità e napoletanità. Il viaggio a Praga poi, è stato un vero bijoux! Si può solo bissare, magari qualche km più in a nord.

Teresa, che mi ha fatto fare una bella pausa nel pieno della corsa esami, quando il divertimento può solo essere concentrato in cinque giorni, perchè non hai tempo. Nonostante mi lamentassi praticamente ogni sera, quella mini vacanza ad Alicante mi ha rigenerato al meglio. Grazie per l'ultima sera, quando ho perso il volo e mi sono precipitato a casa tua cercando di arrivare in aeroporto quanto prima. Difficilmente dimenticherò quella lunga notte.

Finalmente c'è tutta la bella **gente dell'università**, palluccellari e non. I fisici, insomma quelli strani e senza un euro.

Felix, ogni qualvolta ti vedo all'università finisco a ridere, anche se non sempre mi ricordo il principio della conversazione. I nostri primi incontri la dicono lunga: la prima volta che ci siamo conosciuti eri inzozzata come una bambina di tre anni. Quando poi ci siamo rivisti alla magistrale, io avevo i jeans tutti stracciati. Ricette speciali, risate, regali speciali, risate, risotti di non compleanno quando non c'è nient' altro, risate, partite a pallavolo, risate, rebus con il "sangue" sullo specchio, risate, movimenti molesti alle feste di laurea altrui, risate, coefficienti di Clebsh-Gordon sul praticello, risate ... la lista è lunga, ma finisce sempre con risate. Se poi c'è anche **Gnocco Gustoso**, le risate sono sempre le stesse, ma con una simpatica

interiezione qua e là: "Amore, quanto sei bono!". Meno male che Carmine ha quella pazienza invidiabile, mista alla quasi equivalente tranquillità. Ca', tanto poi vengo a Berlino all'insaputa di Felix e organizziamo un paio di quelle serate di cui abbiamo parlato. Scherzo Felix, o forse no? Tanto lo sai non ti libererai facilmente, anche se farò il phd un po' lontano!

I Tuthankamionisti:

- **Fabrizia**. Ormai siamo amici collaudati, sono sicuro che anche fra dieci anni ci sentiremo ancora. Sei stretto con i tempi e non sai se riuscirai a dare l'esame? Chiama la Bizia per un semplice incoraggiamento oppure per sapere gli argomenti più papabili. Ci sono tante imitazioni, ma lei è la più attendibile. Provare per credere! Il mio esame di Complementi testimonia in merito. Grazie anche a te e a **Enrico** per il viaggio a New Orleans: è stata una bell'avventura al sapore di coccodrillo. Fra qualche foto improba di Enrico attorniato di signorine al Mardi Gras (concentra la tua attenzione su di loro e non sui grilli parlanti, che è meglio!) e qualche sassofono per strada, quel weekend mi ha riportato un pò di sangue e ca(/o)lore del Sud, dopo tanto Nord-America. Non ti ringrazio invece per la croce che non mi hai fatto mettere sulla tomba della strega di NO, avrebbe permesso l'inizio di una secolare maledizione wicca su tutti noi quattro.

- **Ciccio**: recupero logbook, filmati trash in laboratorio, interessanti rubriche sulla natura e i suoi mostri, estenuanti countdown per il Natale... Devo aggiungere altro? Sì, quando hai spinto Bizia nell'uscita antincendio facendo risuonare tutto un corridoio. Ho riso veramente tanto quel giorno! Grazie anche per le varie dritte per gli esami, soprattutto per quello finale. France', un'altra cosa: a quanto viaggiano le particelle durante uno starnuto? E a quanto fonde il cioccolato nei buoni muffins che **Carla** gentilmente ci ha preparato per passare i pomeriggi di laboratorio? Carla, dovresti davvero interrogarlo in merito.

- **Nello J/Ψ**, Il mio compagno di gruppo più duraturo della magistrale. Ho dovuto trascorrere ben un anno in sua compagnia, anche se per ragioni diverse. Un punto di vista molto diverso dal mio nell'affrontare le varie problematiche di laboratorio e analisi, che qualche volta mi innervosiva parecchio, ma che al tempo stesso mi ha arricchito abbastanza perchè, come sempre accade, si apprende più dal diverso che dal simile. A causa della tua apatia congenita, sono ben consapevole che non ci vedremo più se non fra dieci anni, quando magari ti beccherò in un ascensore del CERN (un caffè sarebbe chiedere troppo visto la tua accidia sociale).

Giovani, un'ultima cosa, che lo spirito di Tuth sia sempre con voi e cercate sempre di "sbrodolarvi", che è meglio!

Super Cir8, che mi ha fatto "pariare" veramente tanto l'anno che sono stato di più in dipartimento, per conversazioni narrabili e non (soprattutto quelle non!). Come me, un po' lo sguardo del ragazzo di paese e la meraviglia per quella donna fantastica che è la Fisica. Quel dialetto un po' buffo che però diventa un incredibilmente sofisticato accento inglese: difficilmente potrò sentire ancora nominare un Confidence Level con sobrietà . Un po' con tristezza, ormai i percorsi si sono separati, ma chissà, magari un giorno ceneremo in quel di Ginevra e ovviamente pagherai tu, perchè stai chin e sold. Giovine, la scommessa su chi prima solleva il proprio peso in panca resta sempre valida!

Marco, l'ingegnere. Potrai esserti anche laureato in fisica, ma ti chiamerò sempre Marco l'ingegnere. Sei la persona alla quale devo di più per appunti vari. Ho dovuto apprendere l'ingegnerese per capirli, ma sono stati più utili a me che a te. Il tuo problema è stato salutarmi il primo giorno dei corsi, dovevi fidarti del tuo istinto e ignorarmi. Non so ancora come abbia fatto **Peppe** a non menarti durante i mesi di laboratorio. Peppe, grazie per le dritte su dove beccare l'orsetto lavatore a FNAL e soprattutto i buoni biscotti allo User Office. **Mirko**, grazie per avermi fatto divertire abbastanza con i tuoi "delicati" borbottamenti al corso di Astroparticelle e Meccanica Quantistica 2.

La **Sannina** che, avendo visto quanta bella gioventù c'è in Valle Caudina, ha ben deciso di trasferirsi fra queste belle genti. Il paese però... ahi ahi ahi, non è decisamente quello giusto. Confidiamo che al prossimo giro migrerai verso una scelta più opportuna. Ci sono montanari e montanari, ricordalo sempre! Sono ancora in debito di un paio di borracce made in USA per un'epocale scommessa, ma tu, hai ancora un cena bucolica da recuperare. Vedremo chi si sdebiterà per primo.

Il **Pastena** per essere l'amico teorico fastidioso, ma tanto buono di cuore. Quello sempre pronto a vedere il lato buono delle persone, ma anche quello che non crede nel modello Standard e con il quale puntualmente devo "litigare" durante ogni importante occasione. Miche', rassegnati: il premio a Higgs è più che meritato; Newton e Galileo oggi camminerebbero nei corridoi del CERN discutendo di 5σ e C.L.

Fiammetta, grazie per avermi fatto amare così tanto il napoletano in questi anni. Con lei non sai mai cosa aspettarti, un commento sferzante e ironico o uno d'infinita dolcezza. Proprio ora che non ho più un appoggio a Milano dovevi diventare polentona? Aspettati una sorpresa, prima o poi. Poi c'è **Imma** con la quale ho studiato l'ESAME e che mi ha fatto letteralmente andare di matto per Marte. Un giorno mi offrirai un caffè su Marte. Hai già pensato a cosa portare con te nel 2033? MarsOne è alle porte: portati un po' di cose che è un one-way trip, occhio! E ancora **Francesca**, la storica compagna dei laboratori, con la quale ho fatto le necessarie figure con i vari tecnici. Basti ricordare la pulsazione, eh France' ? Strana ironia della sorte, quella persona ha avuto un ruolo non trascurabile in questa tesi. Meno male che ha la memoria corta.

Infine ci sono tutti i palluccelari napoletani e un po' di fisici di diverso orientamento: Bri, Claudio, Simona, Valerio, Riccardone, Enrica, Sebastiano, Bellotta,

Lollo, Melania e Riccardino. Grazie perchè, anche se ho condiviso un po' meno tempo con voi, avete comunque reso piacevole il mio ricordo del dipartimento.

Doveroso è il grazie per tre studenti della magistrale di fisica a Napoli, insieme al loro relatore. Vi chiamerò ζ, ξ, ϑ e Υ perchè mi sono sempre state poche simpatiche come lettere greche. Grazie, siete riusciti a rovinare la mia convinzione che il mondo dei fisici rappresentasse un'isola felice, scevra da personalizzazioni e favoritismi. Tutto questo nell'ultimo mese della mia carriera da studente e per di più nel giorno dell'antivigilia di Natale, che mi avete fatto trascorrere inutilmente in dipartimento e nel traffico.

Grazie anche a tutti quelli che ho dimenticato, volutamente e non.

INTERNATIONAL ACKNOWLEDGEMENTS

I wanna deeply thank **Jeffrey A. Appel** for his support and knowledge. The meetings that we had, proved to be beneficial for this analysis and very instructive for me. I still remember the quote you told me: "Better is the enemy of good". It is very appropriate for me. I'm also grateful to **Marjorie** for the dinner and the book.

Thanks to **Aline Simoes**, **Taisa Maia** and **Grace Caldas** for the time spent together during the strong winter storms in Toronto. We had a lot of fun. I'll never forget the day spent in Niagara-on-the-Lake.

Finally I want to thank **Leonel Villanueva, Emily** and **Flor** for the long talks in the dorm 3, while waiting for dinner. I hope to see you again.

Grazie a tutti. Altro che la particella, il vero valore aggiunto di questa tesi, il vero

siete stati voi.

THANK YOU, GUYS!